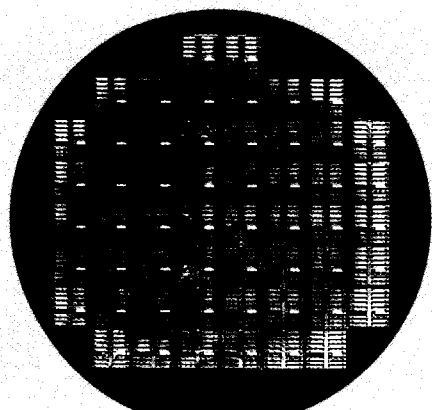


THE TRANSVERSE JUNCTION SOLAR CELL



MARTIN KROON



STELLINGEN

BEHORENDE BIJ HET PROEFSCHRIFT

THE TRANSVERSE JUNCTION SOLAR CELL

DOOR

MARTIN KROON

1. Zonnecellen gebaseerd op een verticale junctie, hebben een fundamenteel lager omzettingsrendement vanwege het feit dat de optische absorptie afhangt van de diepte.
2. In geïmplanteerd gehydrogeneerd amorf silicium wordt de effectieve doteringsconcentratie bepaald door de defectdichtheid.

HOOFDSTUK 3 VAN DIT PROEFSCHRIFT

3. De minimale grootte van het intrinsieke gebied in de transversale junctie zonnecel wordt bepaald door de laterale verstrooiing van de doteringsatomen.

HOOFDSTUK 4 VAN DIT PROEFSCHRIFT

4. De ruimtelijke verdeling van defecten in een amorf silicium diode heeft een veel grotere invloed op de donkerstroom-spanningskarakteristiek dan de energetische verdeling.

HOOFDSTUK 7 VAN DIT PROEFSCHRIFT

5. In een amorf silicium zonnecel heeft een hoge defectdichtheid in de gedoteerde gebieden als gunstig gevolg dat het elektrisch veld in het intrinsieke gebied hoger is.

6. De openklemspanning van een amorf silicium *pin* zonnecel wordt bepaald door de eigenschappen van *p/i* overgang.
M. A. Kroon en R. A. C. M. M van Swaaij, Spatial effects on ideality factor of α -Si:H *pin* diodes, J. Appl. Phys., **90**(2), Blz. 994–1000 (2001).
7. Alhoewel duurzame-energieopwekking de grootste drijfveer is voor de meeste activiteiten op fotovoltaïsch gebied, blijft het vooralsnog een niche in de markt.
8. Besluitvaardigheid impliceert niet dat een beslissing snel genomen dient te worden.
9. Nu presentatie- en schrijfcursussen vast onderdeel uitmaken van het curriculum van veel β -studierichtingen, is het de beurt aan juristen en beleidsmedewerkers om hun communicatie te verbeteren.
10. Gratis software werkt doorgaans beter dan commercieel verkrijgbare.
11. De beperkte omvang van het oeuvre van Jan Vermeer is voornamelijk te wijten aan het gebrek aan vrouwelijke modellen in Delft.



3746

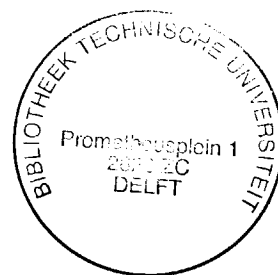
762345

2001-2002

TR 3746

THE TRANSVERSE JUNCTION SOLAR CELL

PROEFSCHRIFT



TER VERKRIJGING VAN DE GRAAD VAN DOCTOR
AAN DE TECHNISCHE UNIVERSITEIT DELFT,
OP GEZAG VAN DE RECTOR MAGNIFICUS PROF. IR. K.F. WAKKER,
VOORZITTER VAN HET COLLEGE VAN PROMOTIES,
IN HET OPENBAAR TE VERDEDIGEN OP
DINSDAG 2 OKTOBER 2001 OM 16 UUR

DOOR

MARTIN ALBERT KROON

NATUURKUNDIG INGENIEUR

GEBOREN TE DEDEMSVAART.

Dit proefschrift is goedgekeurd door de promotor:
Prof. dr. C.I.M. Beenakker

Samenstelling promotiecommissie:

Rector Magnificus (voorzitter)	Technische Universiteit Delft
Prof. dr. C.I.M. Beenakker (promotor)	Technische Universiteit Delft
Prof. dr. H. Wallinga	Universiteit Twente
Prof. dr. ir. M.C.M. van de Sanden	Technische Universiteit Eindhoven
Prof. dr. R.E.I. Schropp	Universiteit Utrecht
Prof. dr. J. Schoonman	Technische Universiteit Delft
Dr. J.W. Metselaar	Technische Universiteit Delft
Dr. R.A.C.M.M. van Swaaij	Technische Universiteit Delft

Dit werk is mede tot stand gekomen door financiële ondersteuning door de Nederlandse Onderneming voor Energie en Milieu B.V. (Novem).

Kroon, M.A.

The Transverse Junction Solar Cell/M.A. Kroon, Ph.D. thesis Delft University of Technology. – With ref. – With summary in Dutch

Keywords: Amorphous silicon, ion implantation, solar cell, diode.

ISBN: 90-9014958-9

Copyright © by M.A. Kroon.

All rights reserved.

No part of this publication may be reproduced, stored in a retrieval system, or transmitted in any form or by any means – optical, electronic, magnetic, mechanical, photocopying, or any other recording system – without the prior written permission of the copyright owner.

Printed in the Netherlands

Contents

1	Introduction	7
1.1	Motivation and outline	7
1.2	Hydrogenated amorphous silicon	8
1.3	α -Si:H Solar cells	10
1.4	The transverse junction solar cell	12
1.5	Potential applications	15
2	Device Fabrication and Characterisation	19
2.1	Introduction	19
2.2	Fabrication process	19
2.3	Plasma deposition and etching	22
2.3.1	Deposition of α -Si:H	22
2.3.2	Reactive ion etching	23
2.4	Optical lithography	24
2.5	Ion implantation	25
2.6	Material characterisation	26
2.6.1	Absorption measurements	26
2.6.2	Conductivity measurements	27
2.6.3	Activation energy measurements	27
2.6.4	Effect of nonuniform doping	28
2.7	Device characterisation	29
2.7.1	Current-voltage measurements under illumination	29
2.7.2	Dark current-voltage measurements	30
2.7.3	Spectral response measurements	30
3	Ion Implantation of Amorphous Silicon	33
3.1	Introduction	33
3.2	Implantation profile	34
3.3	Doping mechanism in α -Si:H	36
3.4	Properties of ion implanted α -Si:H	38
3.4.1	Introduction	38
3.4.2	Optical absorption	38

3.4.3	Electrical properties	41
3.4.4	Discussion	42
4	Experimental analysis	45
4.1	Introduction	45
4.2	Width of the active region	45
4.3	Efficiency considerations	49
4.3.1	Initial efficiency	49
4.3.2	Light-induced degradation	51
4.4	Bottom side illumination	52
4.5	Spectral response	56
4.6	Contact properties	59
4.7	Discussion and conclusions	61
5	Device simulations	63
5.1	Introduction	63
5.2	Vertical effects	64
5.3	Lateral straggle	68
5.4	Conclusions	70
6	Series Connections	73
6.1	Introduction	73
6.2	Interconnecting <i>np</i> junctions	75
6.3	Metal interconnects	78
6.4	Conclusions	81
7	Defect Distribution in <i>a</i>-Si:H <i>pin</i> diodes	83
7.1	Introduction	83
7.2	Theory	84
7.2.1	The defect-pool model	84
7.2.2	Defect distribution in <i>pin</i> diodes	85
7.2.3	Charge transport in <i>a</i> -Si:H <i>pin</i> diodes	86
7.3	Results	88
7.3.1	Procedure	88
7.3.2	Experimental results	88
7.3.3	Comparison to conventional solar cells	90
7.4	Numerical analysis	91
7.5	The ideality factor	94
7.6	Summary and conclusions	98
8	Conclusions	101
A	Flow Charts	103
A.1	General remarks	103

A.2 Crystalline wafer substrates	103
A.3 Glass substrates	106
B Two-Dimensional Device Simulations	109
B.1 Introduction	109
B.2 Comparison of ASA and Medici	109
B.3 The accuracy of Medici	111
B.3.1 Discretisation error	111
B.3.2 Comparison of band diagrams	112
B.3.3 Nonequilibrium conditions	113
B.4 Example input of Medici	114
C Analysis of Thin-Film Transistors	117
List of Symbols and Abbreviations	119
Bibliography	123
Summary	131
Samenvatting in het Nederlands	137
Nawoord	141
Curriculum Vitae	143



Introduction

1.1 Motivation and outline

This Ph. D. thesis is the result of four years research on the Transverse Junction Solar Cell (TJSC). This is a solar cell with a fundamentally different design than conventional solar cells. The TJSC is made by using technologies for the fabrication of micro-electronic devices. There seems to be a contradiction here, because one of the main items in solar cell industry is the up-scaling of fabrication processes to large areas, whereas in micro-electronics much effort is taken to decrease the size of the devices. However, solar cells are not applied only for large-scale conversion of solar energy, but also in small-scale applications, like pocket calculators, watches, *etc.* This kind of applications will gain importance in the future, *e.g.*, in smart cards and disposable electronics. The power consumption of these applications is usually very low; hence, the solar cell requires only a small area.

This research project started as a feasibility study of the TJSC. Soon it was realised that the miniature size of the TJSC should be explored, *i.e.*, the TJSC should be used for small-scale low-power applications or as a photodetector. Note that solar cells and photodetectors are based on the same operation mechanism; only the design and the geometry are slightly different.

The performance and the properties of a solar cell are for a considerable part determined by the choice of material in which the light is converted into electrical power. (Poly)crystalline silicon is the most widely used material for solar cells. However, solar cells of novel materials, like cadmium-telluride (CdTe), copper-indium-diselenide (CIS), and amorphous and micro-crystalline silicon, are evolving fast and (will) have an increasing market share. These materials require novel fabrication technologies, based on the *thin-film* concept, *i.e.*, the active layer is deposited on a cheap carrier substrate, like glass, stainless steel, or flexible polymer foils. The TJSC is a thin-film cell concept and can be made of several materials. However, we have restricted ourselves to amorphous silicon, because at the Delft Institute of Micro-Electronics and Submicron technology (DIMES) the infrastruc-

ture is present for the deposition and processing of this material only.

This research project consisted of several stages. First, a fabrication process was developed, in which TJSC's could be fabricated with an acceptable performance and reproducibility (Ch. 2, App. A). Second, the fabricated cells were characterised and the output parameters were investigated as a function of the design parameters (Ch. 4). The analysis of the material is indissmissible in the understanding of the device behaviour. Therefore, the relevant material parameters were also measured (Ch. 3). Many features were simulated in order to acquire understanding of the physical processes that occur inside the device (Ch. 5). The specific design of the TJSC requires two-dimensional simulations, whereas solar cells are usually simulated in one dimension. Therefore, a lot of work comprised the development of a proper simulation structure to simulate the TJSC with the commercially available device simulator MEDICI (App. B). Third, the suitability for specific applications was studied, *e.g.*, a fabrication process for monolithic series connections (Ch. 6) and the characteristics of the TJSC on glass substrates (Sec. 4.4). The last stage of this research concentrated on the TJSC as a test device to study the physical properties of amorphous silicon diodes (Ch. 7).

The remainder of this chapter is devoted to the fundamentals of amorphous silicon (Sec. 1.2) and amorphous silicon solar cells (Sec. 1.3), the specific features of the TJSC (Sec. 1.4) and a discussion of potential applications (Sec. 1.5).

1.2 Hydrogenated amorphous silicon

The main difference between amorphous and crystalline semiconductors is the absence of long-range order in amorphous semiconductors. However, amorphous semiconductors possess some degree of short-range order (*i.e.*, in the order of an interatomic distance), which gives rise to the electronic band structure. Amorphous silicon (*a*-Si) has a tetrahedral atomic structure, similar to crystalline silicon (*c*-Si). Small deviations from this configuration give rise to the characteristic shape of the band structure of *a*-Si (Fig. 1.1). Variations in the bond angle and bond length lead to a dispersion of the band structure; hence, instead of abrupt band edges, the density of states (DOS) in *a*-Si decays exponentially into the band gap (the *band tails*).

The valence-band tail consists of energy states which are correlated to stressed (or *weak*) Si-Si bonds, having a higher energy than relaxed Si-Si bonds (the valence-band states). Due to thermodynamic fluctuations, weak bonds can acquire a sufficient amount of energy to break and form two dangling bonds. Dangling bond states have an energy close to the centre of the band gap, being higher than the energy of weak bonds; however, when this conversion of bonding states occurs, the total free energy of the system decreases due to relaxation of the amorphous network. There exists an equilibrium between the number of weak bonds and the number of broken bonds [84]. By introducing hydrogen in the *a*-Si network, weak bonds can also be relaxed by forming Si-H bonds, which are not electrically ac-

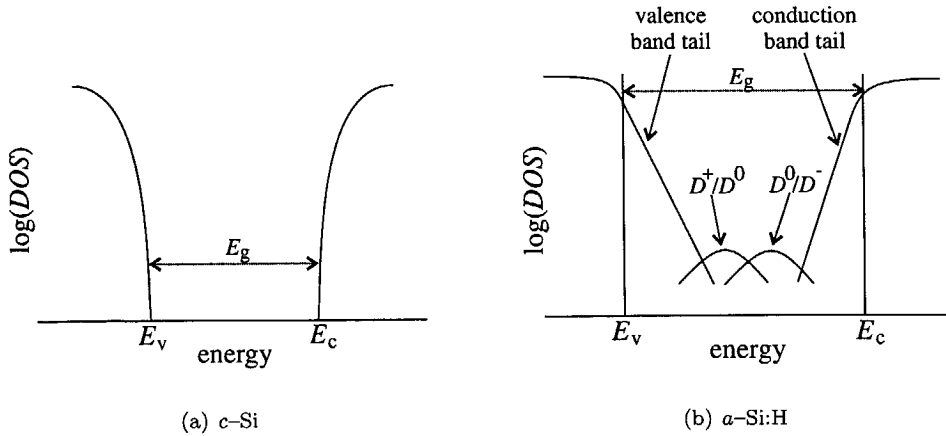


Figure 1.1: Band structures of crystalline Si (a) and hydrogenated amorphous Si (b).

tive (*i.e.*, they are not correlated to a defect state). Hydrogen passivation reduces the density of electrically active dangling bonds from $\sim 10^{19} \text{ cm}^{-3}$ in pure a -Si to $\sim 10^{15} \text{ cm}^{-3}$ in hydrogenated amorphous silicon (a -Si:H) with up to 10 *at.* % hydrogen. This reduction of the defect density makes a -Si:H suitable for electronic applications. State-of-the-art a -Si:H is deposited by plasma enhanced chemical vapour deposition at radio frequency (Sec. 2.3.1), using silane (SiH_4) as the source gas. Under usual deposition conditions, the silane plasma contains a sufficient amount of hydrogen to passivate the dangling bonds during deposition of the material.

The dangling bond is an amphoteric state, which means that it can act both as an electron trap and as a hole trap. In other words, the state has three occupation levels: it can be empty, or occupied by one or two electrons. The empty state is positively charged, the singly occupied state is neutral, and the doubly occupied state is negatively charged. The transition from one to two trapped electrons (denoted D^0/D^-) corresponds to an acceptor state (electron trap) and occurs at a higher energy than the transition from an empty to a singly occupied state (D^+/D^0), corresponding to a donor state (hole trap). The energy difference is caused by electron–electron interactions and is typically 0.2 eV (the *correlation energy*). The dangling bond states are dispersed as a result of the disorder, giving rise to an *energy pool* of defects, which is assumed to have a gaussian distribution. Section 7.2.1 discusses the dangling bond DOS in more detail.

Strictly speaking, amorphous semiconductors do not have a forbidden band gap, since the deviations in the atomic structure yield a high DOS in the band gap. Therefore, the *mobility gap* is used to express the difference between extended

states outside the gap (in which charge carriers are mobile) and localised states inside the gap (in which charge carriers are trapped). The mobility gap is ~ 1.6 eV in pure a -Si and increases with the hydrogen content to $1.8\sim 1.9$ eV in device quality a -Si:H.

In 1977, Staebler and Wronski reported that after long exposure to light (*light soaking*), both the photoconductivity and the dark conductivity decrease, the latter by nearly four orders of magnitude [75]. After an anneal above 150°C , the initial properties of the material could be recovered. This degradation of the material quality was ascribed to an increase in the number of dangling bond states under light soaking. Since then, many models have been reported that might explain this so-called Staebler–Wronski effect. Stutzmann *et al.* derived the kinetics of the widely observed $G^{2/3}t^{1/3}$ dependence of the dangling bond concentration [87]. Electron–hole recombination was shown to be the driving force of defect creation, since it provides the energy to create a dangling bond. Branz presented a ‘hydrogen collision model’, which provides a clarifying mechanism for defect creation [7]. The model explains a process in which two separate Si–H bonds are broken, thereby creating two dangling bond states. The released hydrogen is mobile and diffuses through the network. Energetically the most favourable reaction of hydrogen is the passivation of two dangling bonds, *i.e.*, the reverse process of the dangling-bond creation mechanism. When this process occurs, the hydrogen simply hops to another defect site, without changing the number of defect states. However, two hydrogen atoms can ‘collide’ (*i.e.*, they associate into a paired configuration) and break a Si–Si bond into a metastable $(\text{Si-H})_2$ complex. Two dangling bonds remain at the original hydrogen sites, so the total number of defect states has increased after the hydrogen collision process has occurred.

The degradation processes are reversed under thermal or light-induced annealing. Thermal annealing means the recovery as described by Staebler and Wronski. Light-induced annealing occurs during light soaking and results in stabilisation of the number of defect states after prolonged exposure.

Although the electronic properties of amorphous silicon may be inferior to crystalline silicon, a -Si:H is a very suitable material for opto-electronic devices. Above photon energies of 1.8 eV, the absorption of a -Si:H is about ten times higher than in c -Si. The sun emits most the energy in this part of the spectrum. Therefore, the active layer of a -Si:H solar cells can be much thinner ($< 1 \mu\text{m}$) than in c -Si and hence, the poor electronic properties (*e.g.*, low mobilities, short lifetimes) are overcome to a large extent. Besides, the band gap of a -Si:H is higher, so the open-circuit voltage of a -Si:H solar cells is higher than in c -Si.

1.3 a -Si:H Solar cells

After substitutional doping of a -Si:H was demonstrated by Spear and Le Comber in 1975 [74], the material gained considerable interest, as it set the stage for the fabrication of a -Si:H devices. One year later, this breakthrough resulted in the

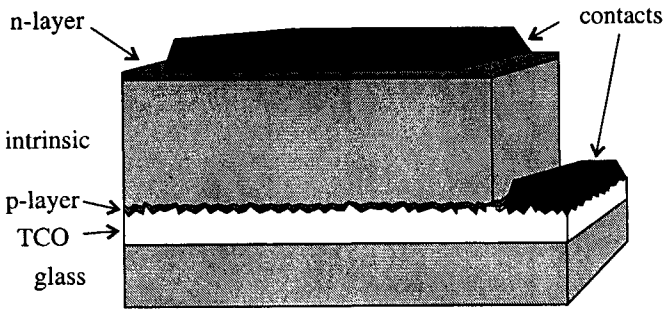


Figure 1.2: Schematic lay-out of an a -Si:H pin solar cell.

first a -Si:H solar cell by Carlson and Wronski, having an efficiency of 2.4% [9].

Figure 1.2 shows the basic structure of an a -Si:H pin solar cell. Doped a -Si:H has a much higher defect density than undoped a -Si:H and contains a lot of trapped charge; therefore, the depletion region in an a -Si:H pn diode is very small. Hence, amorphous silicon solar cells have an intrinsic layer in between the doped layers in order to obtain a depletion region with a thickness of several times the absorption length of light (~ 500 nm). The electron-hole pairs which are generated in the intrinsic layer are separated by the internal electric field; the holes are accelerated towards the p layer and the electrons towards the n layer. The carriers which are generated in the doped layers do not contribute to the photocurrent, since there is no electric field to separate those carriers and they recombine instantaneously at the position where they were created. Therefore, the doped layers are made as thin as possible (10~20 nm) in order to minimise absorption losses. Furthermore, the p layer is an a -SiC:H alloy, which has a lower absorption, due to the wider band gap [96].

The operation principle of crystalline pn solar cells is quite different from the mechanism described above for a -Si:H solar cells. In c -Si solar cells, the electron-hole pairs are generated outside the depletion region and separated by diffusion of the minority carriers. Excess electrons, generated in the p layer, diffuse towards and through the pn junction and are collected in the n layer. The diffusion length of minority carriers in a -Si:H is very small and hence, there is virtually no diffusion transport of minority carriers in doped a -Si:H. Therefore, the current in a -Si:H solar cells is driven by drift rather than diffusion.

The pin structure of an a -Si:H solar cell is sandwiched between well conductive contacts, as the conductivity of doped a -Si:H is rather low. Therefore, a transparent conductive oxide (TCO) is used as a front contact and the back contact is a metal with a high reflectivity and conductivity, like silver or aluminium. Most of the TCO's used at present have self-textured surfaces. At such a surface the incoming light is scattered, resulting in an increase of the optical path length and

the absorption in the cell. In this way, the front and back contacts are employed to enhance the incoupling of light in the active part of the solar cell.

At present, *a*-Si:H *pin* solar cells have initial efficiencies of over 12% under AM1.5 illumination [17]. The efficiency decreases by a factor of 10~30% under light-soaking and then stabilises. In order to reduce the recombination, tandem and triple-junction solar cells have been developed [26]. They consist of a stack of two or three solar cells with tunnel-recombination junctions in between [30]. Since the individual cells in a stack can be made thinner than in a single-junction solar cell, the generated carriers are collected earlier, thus reducing the recombination. An additional advantage of tandem and triple junctions is that by using *a*-SiGe:H or μc -Si:H in the bottom cell, a larger part of the AM1.5 spectrum can be absorbed, since *a*-SiGe:H and μc -Si:H have a smaller optical band gap and the cell design can be optimised such that each junction absorbs a different part of the spectrum. This technique has resulted in a world record initial efficiency of 15.2% and a stabilised efficiency of 13.0% on an *a*-Si:H/*a*-SiGe:H/*a*-SiGe:H triple-junction structure [108].

One of the main advantages of *a*-Si:H solar cells is that it is deposited at a relatively low temperature of, say, less than 250°C. This allows the use of cheap substrates, like glass or polymer foils, and enables fabrication technologies for deposition on large areas. *c*-Si Solar cells are fabricated on self-supporting wafers of 200~300 μm thick, although 50 μm is sufficient to absorb the light. Hence, besides the production price, the energy-pay-back time and the economic use of raw material are also in favour of thin-film solar cells.

1.4 The transverse junction solar cell

The operation principle of a solar cell is relatively simple: first electron-hole pairs are generated by photon absorption, then they are separated by the internal electric field, and finally, the generated charge carriers are collected in the doped regions. Despite its apparent simplicity, the design of *a*-Si:H solar cells have evolved considerably during the last three decades. Much effort has been taken by research institutes and the industry to improve the material properties, to optimise the design of the solar cell, and to develop new technologies for light scattering, contact grids, *etc.* More recently, the trend has moved slowly towards the development of cheaper materials and technologies, rather than improving the cell performance. This transition is mainly a consequence of the maturity of solar energy and market developments.

Nonetheless, the search for novel cell designs and concepts to convert solar energy is still going on. Especially new applications of solar cells are the driving force for new cell designs, particularly for integration in electronic systems, *e.g.*, very cheap cells for disposable electronics, flexible solar cells in large-area electronics, and small solar cells in stand-alone circuits.

This thesis describes the research on the amorphous silicon transverse junction

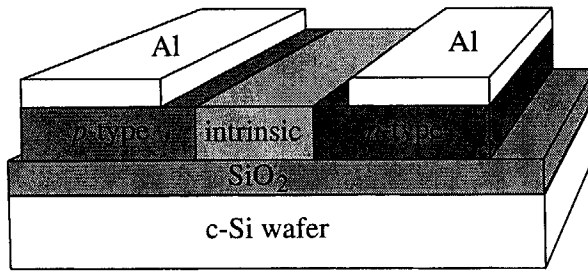


Figure 1.3: Schematic drawing of the TJSC.

solar cell, a new cell design for thin-film solar cells [44]. A schematic drawing of this cell is shown in Fig. 1.3. The novelty of this device is that the semiconductor junction is formed perpendicularly to the surface of illumination. The initial motivation to start this research project was to solve or to avoid some problems which are encountered in 'conventional' thin film solar cells. The advantages of the TJSC with respect to conventional solar cells are

- a. The internal electric field is perpendicular to the direction of incoming light, which gives more freedom to optimise the electrical properties and the optical properties of the solar cell independently;
- b. The TJSC does not require a TCO and a p type window layer. Hence, the absorption losses can be reduced;
- c. The contacts have a planar configuration instead of a 'sandwich' structure. This feature has advantages for series connections, since the interconnects between adjacent cells can be fabricated without additional process steps. This topic is discussed in Sec. 1.5 and is investigated in detail in Ch. 6.

ad. a. a -Si:H Solar cells are complicated devices and in order to obtain maximum conversion efficiency, both the electrical and the optical systems have to be optimised. For example, the optical absorption can be increased by increasing the thickness of the absorbing layer; however, this is at the expense of the internal electric field. Hence, the recombination and the series resistance are increased at the same time. This problem can be relieved by introducing an extra degree of freedom for the optimisation of the device. Roughly spoken, the TJSC is designed such that the internal electrical field is perpendicular to the direction of incoming light. This approach is rather simplistic; the physical consequences of the transverse electric field are discussed in Sec. 5.2.

The concept of a two-dimensional cell design has already been applied before in crystalline solar cells. In 1955, a patent for a photovoltaic cell was submitted to the United States Patent Office by IBM and in 1961 this patent was approved [92].

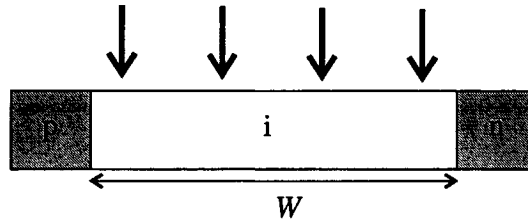


Figure 1.4: Schematic drawing of the photovoltaic cell as described in a patent by IBM [92].

The patent claims a bar of an intrinsic semiconductor with a p -type and a n -type region at each end (Fig. 1.4), which is illuminated perpendicularly to its length axis. The patent does not mention possible fabrication technologies. The aim of this device was to absorb all photons in the depletion region, since the inventors erroneously thought that only those photons contribute to the photocurrent in a crystalline solar cell. They did report neither the advantages of this lateral device with respect to a layered pin structure, nor any experimental results.

The patent claims a structure with a width between 0.1 and 0.5 cm, or smaller than the *transport length*, $l_t = \sqrt{\mu E_g \tau}$. In this definition, μ is the average carrier mobility and τ is the mean carrier lifetime, including surface recombination. A rough estimation of l_t in a -Si:H gives $\sim 4 \mu\text{m}$ (taking $\mu = 1 \text{ cm}^2/\text{Vs}$, $E_g = 1.8 \text{ eV}$, and $\tau = 10^{-7} \text{ s}$). Hence, the TJSC is claimed by this patent, since the junction in a TJSC has a width of typically $1 \mu\text{m}$. However, to our knowledge, it is the first time that a lateral concept is applied to thin-film solar cells.

ad. b. The shorter wavelengths of the solar spectrum have the highest absorption coefficient, hence, the absence of the TCO and the a -SiC:H p layer should result in a better response of the cell in the blue part of the spectrum. A conventional solar cell has an effective optical system, with an anti-reflective optical system on top (*i.e.*, glass, TCO, and a -Si:H have increasing refractive indices), a textured surface (the TCO surface), and a back reflector. In order to compete with conventional solar cells, the TJSC should also have these features; only then the absence of the TCO and the p -type layer can be explored. The requirements of anti-reflection layers and back reflectors for the TJSC is that it is electrically insulating, that it passivates the surface states, and that it does not contain any electrical charge.

It has been tried before to avoid the absorbing layers on top of the active layer in a thin-film solar cell. With this aim, the field-effect a -Si:H solar cell was developed at the Tokyo Institute of Technology [38]. The lay-out of this cell is shown in Fig. 1.5. The cell is an nip junction of which the p layer is removed locally over a distance of $1 \mu\text{m}$. On top of the intrinsic layer a charged dielectric layer is deposited, which induces an inversion layer near the surface of the intrinsic

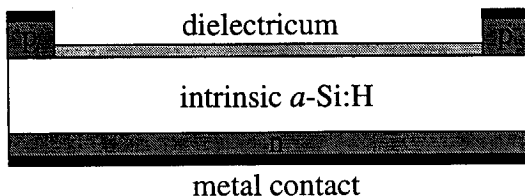


Figure 1.5: Schematic drawing of the a -Si:H field effect solar cell (after Koinuma *et al.* [38]).

material. This inversion layer is contacted by the remaining p -type islands. The most important result is an increase of the simulated short-circuit current of 35% as compared to a conventional a -Si:H solar cell. So far, the research on this type of solar cell has not exceeded the stage of device simulations.

1.5 Potential applications

A novel application for solar cells is integration with micro-electronic devices [46, 47]. Micro Electro-Mechanical Systems (MEMS) are chips with an integrated sensor or actuator, *e.g.*, tuneable mirrors [29, 60] and micro-machined cantilevers [31, 93]. They often require a high voltage in the range of 10~100 V, but the power consumption is very low. Such high voltages are usually not supplied by the circuitry around the device and especially in these devices it is interesting to use an integrated solar cell for the generation of a high voltage. Integration of a solar cell in the MEMS is a cheap and compact solution for stand-alone devices, especially in portable electronics. The TJSC has potential for this type of applications, since it can be integrated relatively easily in micro-electronic systems and an array of cells connected in series can be fabricated without additional process steps. Moreover, the fabrication process is fully compatible to standard micro-electronics technology.

When a solar cell is integrated in a microchip, it can be positioned either next to the device [46, 47] or on top. In the latter case, the semiconductor devices are fabricated in the silicon wafer and they are interconnected using several metallisation layers. When the back-end processing has finished (*i.e.*, all metallisations are made), the top surface is planarised and substrate layer is deposited for the TJSC (Fig. 1.6). This layer must be absorbing (and preferably reflecting) in order to prevent photogeneration in the silicon wafer. Contact holes have to be etched in the substrate layer and the solar cell can be contacted to the microchip. Such a process has been developed at the University of Siegen and is known as the TFA process (Thin Film on ASIC, where ASIC stands for 'Application-Specific Integrated Circuit') [6]. The purpose of this process is to integrate a matrix of a -Si:H photodetectors with the read-out electronics.

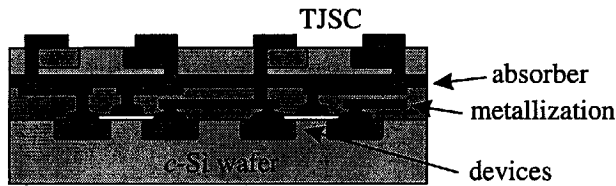


Figure 1.6: Possible lay-out of a TJSC integrated with a micro-electronic circuit.

It is also possible to integrate TJSC's as photodetectors with a -Si:H thin-film transistors (TFT's) [13]. Amorphous silicon photodetectors can be used in a wide range of applications. One of the main advantages of a -Si:H photodetectors is the possibility to fabricate two-dimensional matrices of detector pixels on a large area. For example, a matrix is used for scanning of documents and for x -ray imaging in medical applications. Moreover, a -Si:H photodetectors are a cheap alternative for CCD cameras, *e.g.*, in TFA technology [6]. Three-colour detectors can be fabricated in multiple (hetero)junction configurations, without additional colour filters [100, 102]. In 1995, a study has been started for applying a -Si:H photodetector matrices for replacing the receptors in the retina of the human eye, using a flexible substrate [66].

The design of an a -Si:H photodetector is similar to a solar cell. A small reverse-bias voltage is applied continuously to the photodetector, because the photosensitivity is highest under reverse bias. The reverse current is more or less proportional to the illumination intensity over a large range.

One-dimensional arrays and two-dimensional matrices of a -Si:H photodetectors can be fabricated in several ways. A complicating factor is the integration of the photodetector with a switching device for addressing the pixel. When each pixel is connected individually, the number of wires connecting the display would be very high; therefore, the pixels are scanned in a matrix configuration, where each photodetector is connected to a switching element (Fig. 1.7). Important design issues of a -Si:H photodetector matrices are [83]

- The size of a pixel, *i.e.*, the size of the sensor and the accompanying read-out electronics. The pixel size determines the resolution of the imager. The larger the area consumption of the read-out electronics and the interconnects, the smaller the detector and thus, the sensitivity of the imager.
- The switching speed of the sensor and the read-out electronics. The image is read by addressing each pixel and each line subsequently. The scan rate depends on the capacitance. Too fast reading of the display results in cross-talk between the pixels.
- The off-current of the sensor. This is the dark current at reverse-bias voltage.

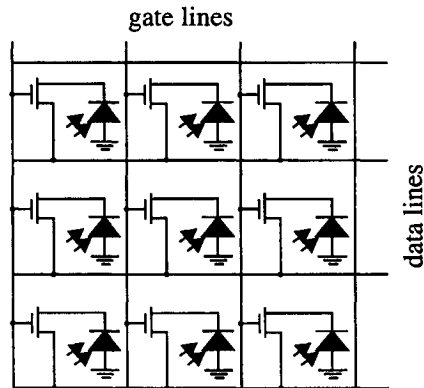


Figure 1.7: Example of a two-dimensional matrix for addressing photodetectors with TFT's.

When an a -Si:H pin diode is used as the switching element, both the detector and the switch can be fabricated in the same stack of a -Si:H layers [3] or in two stacks on top of each other [10]. However, the switching speed of a -Si:H diodes is low and therefore, a TFT is preferred as the switching element. The drawback of TFT circuits is that the photodetector and the TFT are fabricated separately, using different depositions of a -Si:H. The stack of a -Si:H for fabricating the detector is deposited on the entire substrate and subsequently, the periphery of the detector is removed by reactive-ion etching. This is done to insulate the detectors and to create space for the TFT's and the interconnects. The area consumption of the read-out electronics can be reduced by stacking the detector on top of the electronic circuit, such that only the n layer of the pin structure needs to be etched [48]. The lateral leakage in the p layer and the i layer is very small. However, the technology for stacking the detectors on the read-out electronics is complicated. Therefore, the TJSC has potential for this type of applications, since it is a small device and it can easily be integrated with the addressing and read-out electronics. The functionality of the TJSC as a photodetector is discussed in this thesis. The characteristics of a -Si:H TFT's were also studied in a pilot experiment, in which the TFT's were made in the same fabrication process as a TJSC, without additional process steps. The results of this experiment are presented in Appendix C.



Device Fabrication and Characterisation

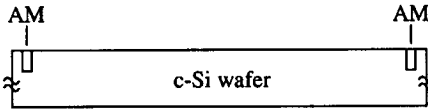
2.1 Introduction

This chapter gives an overview of the fabrication process of the TJSC in Sec. 2.2 and discusses in separate sections the most important technologies, *i.e.*, *a*-Si:H deposition, reactive ion etching, optical lithography, and ion implantation. Sections 2.6 and 2.7 describe the analytical techniques used to characterise the material and the devices.

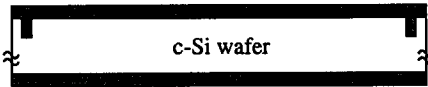
2.2 Fabrication process

This section follows the schematical flow chart in Fig. 2.1. The fabrication was carried out in the class 100 cleanroom facility at DIMES, except steps *c* and *h*. This overview follows the flow chart for samples on crystalline wafer substrates. Details and relevant process parameters can be found in App. A.2. For glass substrates, a few modifications are required (see App. A.3).

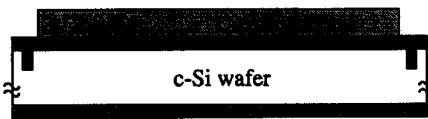
- a. **Alignment marks.** Two marks are etched into the wafer, which are used by the wafer stepper to align the lithographic patterns of consecutive process steps (*cf.* Sec. 2.4). These marks are etched in the periphery of the active area.
- b. **Thermal oxidation.** The silicon wafer is oxidised in a furnace at 1100°C [37], in order to obtain an insulating substrate. Incidentally, the oxide layer was deposited by Plasma Enhanced Chemical Vapour Deposition (PECVD) at 400°C, however, a thermally grown oxide has better electrical properties, *i.e.*, less incorporation of interface and oxide charge [52].
- c. **Deposition of *a*-Si:H.** An intrinsic layer of *a*-Si:H is grown by PECVD. The



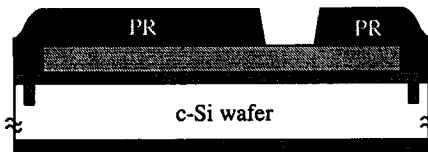
a. Two alignment marks (AM) etched in wafer edge.



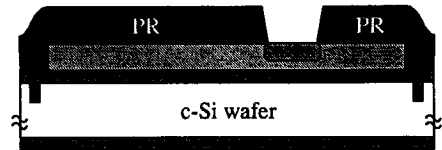
b. Thermal oxidation of wafer 550 nm).



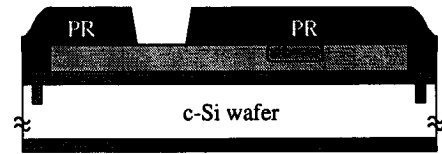
c. Deposition of intrinsic a -Si:H (500 nm).



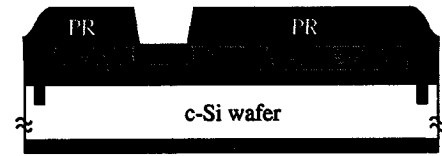
d. Lithography (mask IN).



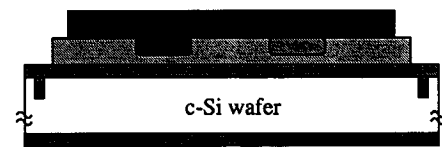
e. Ion implantation of phosphorus.



f. Lithography (mask IP).

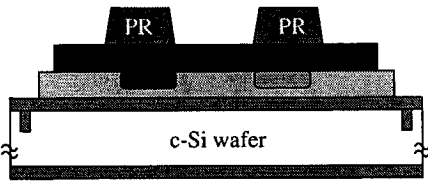


g. Ion implantation of boron.

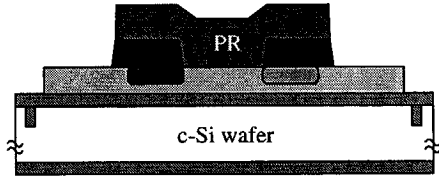


h. Aluminium evaporation (300 nm).

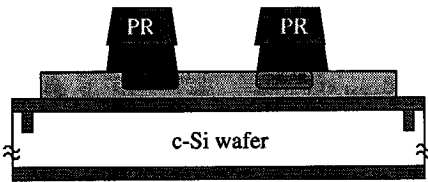
Figure 2.1: Schematic overview of the fabrication process of TJSC's. The enumeration corresponds to the items in the text.



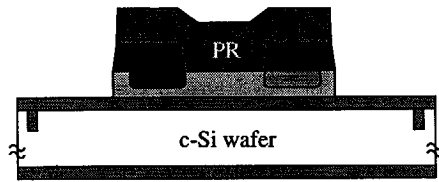
i. Lithography (mask IC).



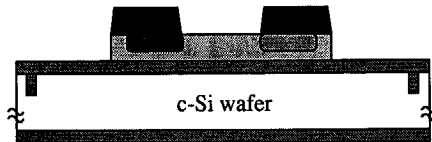
k. Lithography (mask MESA).



j. Reactive ion etching of aluminium.



l. Reactive ion etching of *a*-Si:H.



m. Final device.

Figure 2.1: continued.

a -Si:H is deposited through a shadow mask, using deposition conditions which are optimised for application in conventional *pin* solar cells. The most widely used layer thickness is 500 nm. The set-up and the deposition process are described in Sec. 2.3.1.

- d. **Patterning of n region.** A layer of photoresist (PR) is spun on the wafer, illuminated through a mask and developed. Sec. 2.4 summarises the physics and technology of optical lithography.
- e. **P^+ implantation.** Ion implantations of phosphorus were carried out at two different energies through the same mask. The ion energies and the corresponding doses have been optimised to obtain a more or less uniform doping concentration as a function of depth. The obtained concentration profile is shown in Fig. 3.3. The physics and technology of ion implantation are discussed in Sec. 2.5.
- f. **Patterning of p region.** See step *d*.
- g. **B^+ implantation.** See step *e*.
- h. **Aluminium evaporation.** A 300 nm thick layer of pure aluminium is deposited by electron beam evaporation. The contacts are formed in this layer.
- i. **Patterning of contacts.** See step *d*.
- j. **Aluminium Etching.** The aluminium is etched by reactive-ion etching (RIE), using BCl_3 and Cl_2 as the etching gases. The RIE process is described in Sec. 2.3.2.
- k. **Patterning of a -Si:H layer.** See step *d*.
- l. **Mesa etching.** The a -Si:H layer is etched by RIE, leaving each device on a separate island of a -Si:H. This is called a mesa etch and is used for the electrical insulation between devices (Sec. 2.3.2).

The device formed by this process is shown schematically in Fig. 2.1.m.

2.3 Plasma deposition and etching

2.3.1 Deposition of a -Si:H

Plasma Enhanced Chemical Vapour Deposition (PECVD) is the most widely used technique to deposit a -Si:H for solar cell applications. At DIMES, a PECVD set-up is used with separate chambers for the p , i , and n layers, in order to prevent cross-contamination by residual gases. For the fabrication of TJSC's, intrinsic layers are grown using the deposition parameters for the fabrication of the i layer in standard solar cells (App. A). The layer thickness is typically 500 nm.

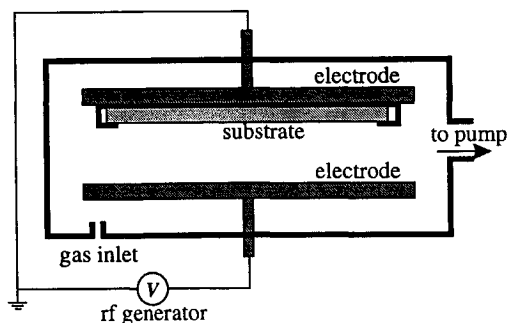


Figure 2.2: Schematical lay-out of a reactor chamber for PECVD and RIE.

Figure 2.2 shows a schematical lay-out of the deposition chamber. The substrate is mounted upside-down and heated. Silane (SiH_4) is introduced into the chamber. Silane decomposes spontaneously at temperatures higher than $\sim 450^\circ\text{C}$ [79], however, at such a high temperature the quality of the deposited α -Si is very poor, due to the low concentration of hydrogen in the layer. Hence, the gas molecules are decomposed at low temperatures using a radio frequency (rf) plasma (13.56 MHz). The plasma is obtained by an alternating electric field between two electrodes, in which free electrons oscillate and collide with SiH_4 molecules. Due to these collisions, the bonds in the SiH_4 molecules are broken and ions and radicals are formed. The radicals (SiH_3 , SiH_2 etc.), which are the main precursors of the growth of the layer, diffuse towards the substrate and react with surface bonds. The deposition rate is typically 2 \AA/s .

2.3.2 Reactive ion etching

Reactive Ion Etching (RIE) is a form of dry etching to etch thin films anisotropically in a plasma. The operation principle of dry etching is that chemical and/or physical reactions occur at the surface, such that the surface atoms get into a gaseous form. The RIE set-up is similar to the PECVD set-up (Fig. 2.2). Etching can be induced by sputtering of ionised particles (physical etching) or by chemical reactions between the sample surface and the radicals (chemical etching) [69]. In case of physical etching, the ions are accelerated towards the electrode that supports the wafer. This is caused by the self-bias of the plasma, *i.e.*, a DC bias persists when the areas of the two electrodes are different [69]. The electrode configuration and the plasma can be regarded as a plate capacitor. The charge per unit area is higher at the smallest plate. Due to the acceleration of ions, physical etching is anisotropic, *i.e.*, the etch rate is higher in the longitudinal than in the lateral direction. Etching in the lateral direction is often undesired, since it often leads to smaller and uncontrollable dimensions of the etch structures.

Chemical etching allows selective etching, *i.e.*, a high ratio between the etch rates of different materials. The selectivity is an important issue, especially in case of the aluminium etch. When the aluminium layer is removed, the etch process should stop at the underlying amorphous silicon. However, the chlorine radicals also react with silicon. A comparison with wet chemical etching of aluminium, did not give any indication of damage to the active region of the TJSC for short exposure of α -Si:H to the chlorine plasma (*i.e.*, less than 10 seconds after the aluminium was completely etched). The selectivity of the fluorine plasma is very low: α -Si:H is etched about three times as fast as the underlying silicon oxide layer. However, this is not harmful since the oxide layer is very thick and not an active part of the device.

RIE is used twice in the fabrication of TJSC's: the aluminium etch (Fig. 2.1.j) and the α -Si:H etch (Fig. 2.1.l). Amorphous silicon is etched by SF_6 diluted in He. Helium is an inert diluent, which controls the etch rate and improves the uniformity. Aluminium is etched by BCl_3 and Cl_2 diluted in N_2 . Molecular Cl_2 etches Al isotropically, but it does not react with native oxide (Al_2O_3) [64]. BCl_3 is added in order to etch Al_2O_3 . Nitrogen increases the bombardment energy, which is beneficial for the anisotropy.

2.4 Optical lithography

Lithography is a technique to transfer an image from a mask onto a photoresist (PR) layer. The process consists of the following steps.

1. **Priming.** A primer (hexa-methyl-disilazane, HMDS) is vapourised onto the wafer to enhance the adhesion of PR to hydrophylic surfaces (*e.g.*, SiO_2).
2. **Coating.** Dissolved PR is deposited on the wafer by spin coating. The layer thickness is typically $1.4 \mu\text{m}$.
3. **Prebake.** The solvent is evaporated by baking on a hotplate.
4. **Alignment.** Two alignment marks have been etched in the wafer (Fig. 2.1.a) and in the mask. The wafer stepper aligns the wafer with respect to the mask in the x - and y -direction and in the rotation angle.
5. **Exposure.** The wafer stepper projects the mask 54 times on the wafer by a step-and-repeat method. The pattern on the mask is reduced by a factor of 5, resulting in an image of $1 \times 1 \text{ cm}^2$. The light source is a mercury arc lamp, from which the i -line ($\lambda=365 \text{ nm}$) is used. The resolution (*i.e.*, smallest feature size that can be projected) is $0.5 \mu\text{m}$ [1].
6. **Postbake.** After exposure the wafer is baked on a hotplate to enhance the contrast between exposed and unexposed PR. Due to interference fringes, the plane between exposed and unexposed PR is not completely flat. During the postbake, exposed molecules diffuse out of the unexposed region.

7. **Development.** The exposed PR is dissolved in a liquid developer by a spray puddle. After developing, the wafer is rinsed with water and dried.
8. **Hardbake.** The remaining PR is made more resistive to etchants *etc.* by baking on a hotplate.

This lithographic process is optimised such that the exposure energy (*i.e.*, the shutter time) is the only variable which has to be set before each exposure. When the exposure energy is too low, residues of PR will remain in the exposed areas after development. When the exposure energy is too high, scattered light exposes molecules outside the area defined by the mask and the developed areas become larger than defined. The fixed parameters are listed in Table A.1.

Typical sources of inaccuracies are the alignment procedure, under-exposure (resulting in smaller linewidths), over-exposure (larger linewidths), and inaccuracies in the fabrication of the masks. In the integrated-circuit industry, an inaccuracy of 20~25% of the resolution is tolerable [51]. The resolution of the wafer stepper used in this process is 0.5 μm , which implies an inaccuracy of more than 0.1 μm . This results in a large spread of the cell performance, since the characteristics of the TJSC are very sensitive to the width of the intrinsic region. In several experiments, inaccurate or irreproducible results were caused by the lithographic process (*e.g.*, Secs. 4.4 and 6.3).

2.5 Ion implantation

This section describes the technique of doping a semiconductor by ion implantation. Chapter 3 discusses the typical impurity profiles obtained from ion implantations, the doping mechanism in *a*-Si:H, and experimental results.

The main components of an ion implanter are shown in Fig. 2.3. All components are situated in a high vacuum chamber. For the implantation of boron and phosphorus, the source gases BH_3 and PH_3 are used, respectively. The source gas is dissociated by heated filaments and the positive ions are accelerated by a high voltage applied between the ion source and the mass spectrometer (10 or 35 kV). The mass spectrometer is used to select ions with the desired mass (B^+ or P^+). Heavier particles (such as PH , PH_2 *etc.*) and doubly charged particles (*e.g.*, B^{2+}) are undesired since they will penetrate the wafer with different momenta. The selected ions are accelerated again to the final energy. The ion beam scans the entire wafer surface using electrostatic scan plates in the *x*- and *y*-directions. The wafer is electrically insulated and the surrounding Faraday cup is connected to earth via a Coulomb meter, which measures the charge required to compensate the charge built up in the wafer. The implantation process is finished when the measured charge equals the desired ion dose times the wafer area.

The ion implanter is designed for implantation in crystalline wafers. Therefore, the wafer is tilted by 7° to prevent channeling. This has only a small effect on the

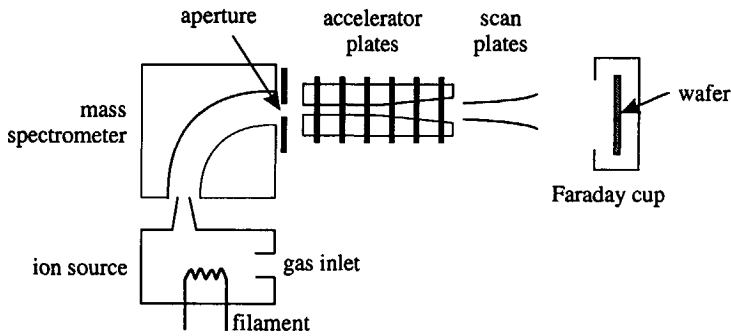


Figure 2.3: Schematic representation of the main components of an ion implanter.

implantation depth, however, the tilt should be kept in mind when analyzing the lateral straggle of dopants (Sec. 3.2).

2.6 Material characterisation

2.6.1 Absorption measurements

Reflection-Transmission (RT) measurements are used to determine the spectral absorption of *a*-Si:H layers deposited on glass substrates. In this work, the main purpose of RT measurements is to determine the thickness of the deposited *a*-Si:H layers and the optical band gap. The thickness is calculated from the interference fringes in the reflection and transmission spectrum. The Tauc energy, E_{Tauc} , is a widely used parameter to express the optical band gap. For photon energies $h\nu > E_{\text{Tauc}}$, the absorption obeys the relation

$$\sqrt{\alpha h\nu} \propto (h\nu - E_{\text{Tauc}}), \quad (2.1)$$

where the absorption coefficient, α , is calculated from the measured reflection and transmission.

In the sub-band gap energy range, the absorption is too low to do RT measurements accurately. In this part of the spectrum, the absorption is measured by Dual Beam Photoconductivity (DBP) [101]. This technique measures the photoconductivity of a sample as a function of wavelength. The photoconductivity is proportional to the number of electrons excited from trap levels at a specific depth into the extended states. The absorption spectrum contains an exponential part (the Urbach tail), which is assumed to represent the valence band tail. DBP measurements are used to determine the Urbach energy and give an estimate of the defect density.

2.6.2 Conductivity measurements

When the dark conductivity is measured, the semiconductor film is in thermal equilibrium, provided the film is homogeneous. The dark conductivity is given by

$$\sigma_d = q [\mu_e n_0 + \mu_h p_0], \quad (2.2)$$

where the subscript '0' denotes the equilibrium value. Under illumination, excess free charge carriers are generated, giving

$$\sigma_{ph} = q [\mu_e (n_0 + \delta n) + \mu_h (p_0 + \delta p)], \quad (2.3)$$

where $\delta n = \delta p$ are the excess carrier concentrations. The ratio σ_{ph}/σ_d is called the *photoresponse* and is a measure of the quality of intrinsic *a*-Si:H. Device-quality intrinsic *a*-Si:H has a low σ_d (since n_0 and p_0 are small) and a high σ_{ph} (long carrier lifetimes). The photoresponse is $10^6 \sim 10^7$ in device-quality intrinsic *a*-Si:H. Doped *a*-Si:H has a high σ_d (indicating a high effective doping concentration) and a relatively low photoresponse, caused by the high concentration of majority carriers.

The conductivities are measured on planar test structures. They are measured by sweeping the voltage and fitting the linear part of the *I-V* curve. In that way, any nonlinearities, like nonideal contact properties, are ruled out.

2.6.3 Activation energy measurements

The activation energy, E_{act} , is the distance between the Fermi level and the nearest mobility band edge. It is determined by measuring σ_d as a function of temperature, according to the Maxwell-Boltzmann equation. For example, in case of n-type *a*-Si:H,

$$\sigma_d(T) = \sigma_0 \exp\left(\frac{E_f - E_c}{kT}\right), \quad (2.4)$$

where $E_{act} \equiv -(E_f - E_c)$. Hence, E_{act} is equal to the slope of the $\ln \sigma$ vs. $-1/kT$ curve. The activation energy itself can also vary with temperature, due to changes in the occupation of the DOS in the band gap (which has an asymmetrical distribution around E_f) and the temperature dependence of the mobility gap. In order to prevent these effects, the activation energy is always determined at the same temperature (50°C).

Measurements of the activation energy are important for doped *a*-Si:H, since it is used to express the effectiveness of the doping. The impurity concentration can be simulated (Sec. 3.2) or be determined experimentally (*e.g.*, by secondary-ion mass spectroscopy), however, only a small fraction ($10^{-3} \sim 10^{-4}$) is electrically active. The doping efficiency depends on the structural properties of the material and the doping concentration; therefore, the doping concentration itself is not a good measure of the doping level.

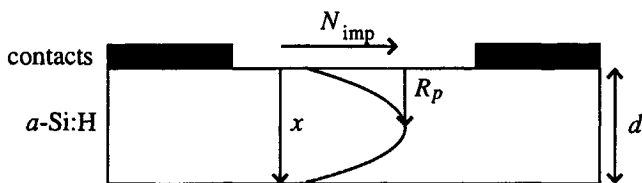


Figure 2.4: Schematic representation of the model used to determine the measured activation energy of a planar sample with a gaussian impurity profile.

2.6.4 Effect of nonuniform doping

In the analysis of the aforementioned characterisation techniques, it is assumed that the measured sample is homogeneous. However, an ion implanted sample has a nonuniform impurity profile in the longitudinal direction and hence, E_{act} and σ_d are not homogeneous. We will now derive an analytical expression which can be used to calculate the error in the activation energy and the conductivity of an $a\text{-Si:H}$ sample doped by ion implantation.

Figure 2.4 shows a schematical representation of a sample with planar contacts and a gaussian impurity profile. The origin of this profile is explained in Sec. 3.2. The gaussian profile is described by the depth of the peak concentration, R_p (the *projected range*), and the width of the profile, σ_p (the *straggle*, see Eq. 3.1). It has been demonstrated that E_{act} has a more or less logarithmic dependence on the impurity concentration, N_{imp} , both for B^+ and for P^+ implanted samples (Fig. 3.7, [16, 19, 39]),

$$E_{\text{act}} \propto E_{\alpha} \ln N_D, \quad (2.5)$$

for moderate doping concentrations. In the calculations, we use $E_{\alpha}=60$ meV (corresponding to the slope of the conduction band edge, see Sec. 3.4.4). Assuming a gaussian impurity profile (Eq. 3.1) gives

$$E_{\text{act}} \approx E_0 + E_{\alpha} \frac{(x - R_p)^2}{2\sigma_p^2}. \quad (2.6)$$

The minimum in E_{act} is located at the top of the peak, which is located at a depth, R_p , of 150 nm from the surface and $\sigma_p = 50$ nm. These data correspond to a phosphorus implantation at 110 keV (see Fig. 3.2). The conductivity of the sample as a function of temperature yields

$$\ln \sigma_d(T) \propto -\frac{E_0}{kT} + \frac{E_{\alpha}}{kT} \frac{1}{d} \int_0^d \frac{(x - R_p)^2}{2\sigma_p^2} dx. \quad (2.7)$$

This equation is evaluated numerically in order to calculate the measured E_{act} from E_{act} at the gaussian peak, E_0 . For a sample with a thickness, d , of 300 nm and with

$E_0 = 0.28$ eV, Eq. 2.7 gives an E_{act} varying from 0.293 eV at room temperature to 0.296 eV at 130°C. Hence, according to this calculation, the measured E_{act} will be ~ 15 meV higher than the 'peak' value. The real variation in E_{act} will be less than the assumed parabolic function, since depletion occurs in a nonuniformly doped semiconductor (*cf.* Fig. 5.2). Moreover, the samples used in the experiments are implanted at two different energies (Table 3.1), making the impurity profile flatter. From this analysis it can be concluded that the inaccuracy caused by the inhomogeneous impurity profile is negligible.

The dark conductivity at room temperature is also affected by the doping profile. Using the model described above, the measured dark conductivity will be 38% lower than the conductivity at the peak value. Note that this is a systematic error, *i.e.*, independent of the doping concentration.

2.7 Device characterisation

2.7.1 Current–voltage measurements under illumination

The current–voltage (I – V) characteristics of an illuminated solar cell are measured using a solar simulator. This is a He–Xe arc lamp with a system of filters, lenses, and mirrors, such that the produced spectrum resembles the AM1.5 spectrum. This is a standardised spectrum, corresponding to the average of the solar spectrum at the surface of the earth [15]. The intensity of the AM1.5 spectrum is 100 mW/cm². The voltage is swept by a Hewlett Packard 4145B parameter analyser and the current is measured. The performance of a solar cell is expressed by the so-called *external parameters*. These are the open-circuit voltage, V_{oc} , the short-circuit current, I_{sc} , the maximum power point, P_{max} , and the fill factor, which is defined as $FF = P_{\text{max}}/(V_{\text{oc}}I_{\text{sc}})$ (see Fig. 2.5). The efficiency, η , is calculated by dividing P_{max} by the illumination intensity.

The inaccuracy of I – V measurements under AM1.5 illumination is estimated to be $\sim 8\%$. Possible origins the inaccuracy are

- Variations in the intensity and the spectrum of the solar simulator, caused by the lifetime of the lamp and changes in the alignment of the mirrors and lenses;
- Temperature of the sample under study. The temperature of the substrate holder is not controlled and the sample is heated by the light;
- Noise in the electrical circuit. The power supply of the solar simulator produces a strong electromagnetic field which induces noise in the order of 1 nA, which affects the measurement near V_{oc} .

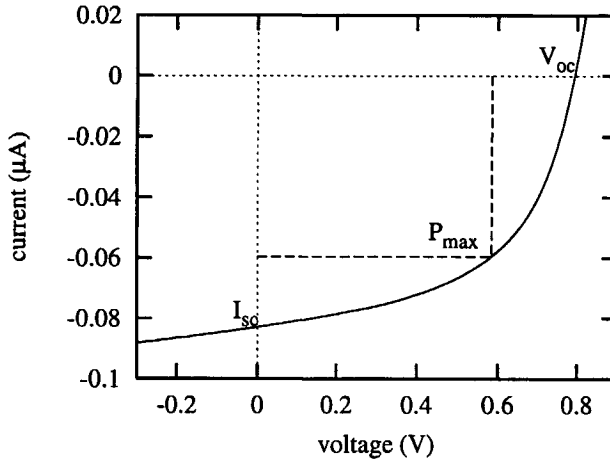


Figure 2.5: I - V curve of a TJSC measured under AM1.5 illumination. The width of the intrinsic region is $1.0 \mu\text{m}$, the α -Si:H layer thickness is 500 nm , and the length of the junction is 3 mm . The substrate is an oxidised silicon wafer. The external parameters yield: $V_{oc} = 0.79 \text{ V}$, $I_{sc} = 0.083 \mu\text{A}$, $FF = 0.53$.

2.7.2 Dark current–voltage measurements

Dark I - V curves contain information on the generation–recombination processes in the intrinsic region (ideality factor, m , saturation current, J_0), on leakage currents, and the series resistance. Dark measurements on α -Si:H solar cells can be very time consuming, since the current density is very low under reverse bias and low-forward bias conditions. Hence, the charging and discharging of trap states occurs slowly. A computer routine has been developed that sets the bias voltage of a Keithley 617 electrometer and measures the current through the sample every few seconds. When the variance during the last 20 s is less than 3%, the current is measured again and stored. It was found experimentally that a sweep from high bias to low bias is measured faster than a sweep from low bias to high bias. Apparently, the discharging of trap states occurs faster than the charging.

2.7.3 Spectral response measurements

Spectral response measurements are used to determine the performance of the solar cell as a function of the wavelength of the incoming light. These measurements provide the external quantum efficiency (QE) of the solar cell and give an estimate of the internal QE. The latter represents the fraction of the incoming photons which create an electron–hole pair. The external QE is defined as the number of incoming photons that result in a current, *i.e.*, the internal QE multiplied by the fraction of charge carriers which are collected. Hence, the external QE is smaller

than the internal QE. The external QE is given by

$$QE_{\text{ext.}}(\lambda) = \frac{I(\lambda, V)}{q\phi(\lambda)}, \quad (2.8)$$

where $\phi(\lambda)$ is the photon flux. The external QE depends on the strength of the internal electric field. Hence, it is a function of the applied voltage. By applying a reverse-bias voltage, the external QE increases, due to the stronger internal field. In the ideal case, the external QE saturates towards the internal QE.

Shorter wavelengths are absorbed better than larger wavelengths. Hence, the quantum efficiency of blue light is a measure of the collection efficiency in the top of the cell and the QE of red light is a measure of the efficiency in the entire cell.

In the experimental set-up, the sample is illuminated with a chopped monochromatic light beam. The system is calibrated by a photodetector with a known quantum efficiency. The beam is focussed on the sample such that the light spot is ~ 0.5 mm in diameter. The width of the TJSC is much smaller than the spot size, so only a fraction of the incoming photons is absorbed. Therefore, spectral response measurements do not give quantitative data of the QE of a TJSC. Nevertheless, the shape of the QE curve can be determined and compared to other types of solar cells.



Ion Implantation of Amorphous Silicon

3.1 Introduction

Doping of amorphous silicon was first demonstrated by Spear and Le Comber in 1975 [74]. They showed results on a -Si:H which was doped by adding diborane (B_2H_6) or phosphine (PH_3) to silane in a PECVD set-up (so-called *gas-phase doping*). The demonstration of substitutional doping was quite revolutionary, since it had long been thought that amorphous semiconductors cannot be doped due to the disordered nature of the material.

In 1980, Kalbitzer *et al.* showed that a -Si:H can also be doped by ion implantation of substitutional impurities (like boron and phosphorus) and interstitial impurities (*i.e.*, the alkali elements) [36]. It was found that the electrical properties of ion implanted a -Si:H can be varied in almost the same range as in a material that is doped from the gas phase, although in the latter case, the doping efficiency (*i.e.*, the fraction of doping atoms at electrically active sites) is 50~100 times higher.

The main advantage of ion implantation is that doping can be introduced locally into an a -Si:H layer by using a mask layer. Gas-phase doping is only possible when the doped regions of the device are deposited layer by layer. For the fabrication of the TJSC, ion implantation is necessary to form the doped regions.

This chapter discusses the distribution of doping atoms in ion implanted a -Si:H by using Monte-Carlo simulations (Sec. 3.2). Section 3.3 discusses the doping mechanism in a -Si:H. The material properties of ion implanted a -Si:H are investigated in Sec. 3.4 and a model is derived that describes the relation between the activation energy and the defect DOS in ion implanted a -Si:H (Sec. 3.4.4) [39].

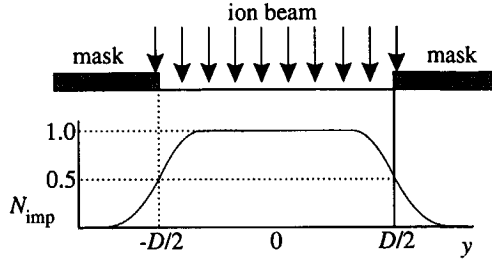


Figure 3.1: Fraction of the total implanted dose through a narrow mask opening (after Giles [21]).

3.2 Implantation profile

The ion implanter accelerates the ions to an energy in the range of 10 keV to 180 keV. The accelerated particles collide with Si atoms in the a -Si:H film. Since the ion energy is much larger than the energy of a Si-Si bond (~ 2.5 eV [79]), the ions collide inelastically. At each collision, the network is distorted and the implanted atom is scattered and loses energy. Finally, the atom is stopped at a certain position, which is determined by the statistics of the scattering processes and the depth distribution of final positions is roughly gaussian,

$$N_{\text{imp}}(x) = \frac{\Phi}{\sqrt{2\pi}\sigma_p} \exp\left[\frac{-(x - R_p)^2}{2\sigma_p^2}\right], \quad (3.1)$$

where Φ is the implanted dose, which is a process parameter. The mean value, R_p , is called the longitudinal projected range and the deviation, σ_p , is the longitudinal straggle. The atoms are scattered in the lateral direction as well. It is difficult to determine the lateral profile accurately, so generally, a gaussian profile is assumed in the lateral (y -)direction [21]. The two-dimensional impurity distribution is written as

$$N_{\text{imp}}(x, y) \approx N_{\text{imp}}(x) \exp\left[\frac{-y^2}{2\sigma_l^2}\right]. \quad (3.2)$$

Strictly spoken, the lateral range depends on the depth. However, for simplicity we define the *mean* lateral straggle, σ_l , as the average of the straggle of all implanted atoms [111]. The lateral straggle is of importance only at the edge of a mask opening (Fig. 3.1).

Biersack and Haggmark developed a computer code that calculates the implantation profile using Monte-Carlo simulations [5]. This computer code, named TRIM, calculates the trajectories of a number of ions with statistically determined collision events.

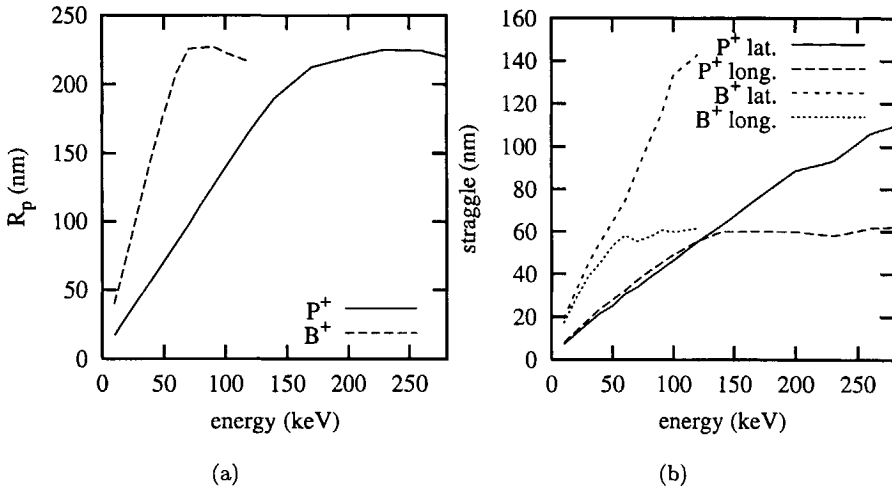


Figure 3.2: (a) Longitudinal projected range and (b) longitudinal and lateral straggle of boron and phosphorus implanted a -Si:H. The data were obtained from Monte-Carlo simulations in TRIM [5] with a tilt angle of 7° and a mass density of 2.27 g/cm^3 .

The longitudinal range and straggle and the lateral straggle were calculated in TRIM for boron and phosphorus implanted in a -Si:H (see Fig. 3.2). From these plots, we determined suitable implantation energies for the TJSC. At these energies, the dose was determined from the longitudinal profile, such that the impurity concentration is more or less uniform. The obtained parameters are listed in Table 3.1, giving the profiles as shown in Fig. 3.3.

Unfortunately, Monte-Carlo simulations have a limited resolution. The statistical error is equal to the square root of the number of ion trajectories. Therefore, it requires the calculation of more than 100,000 trajectories in order to obtain an acceptable profile over two decades (*i.e.*, the resulting error is 0.3%). This requires a lot of computer time and covers only a small part of the range in which the doping concentration influences the electrical properties of a -Si:H.

Realistic implantation profiles are asymmetric in the longitudinal direction. Several analytical models have been developed to express the profile more accurately than as a gaussian function [90]. The most widely used model is a Pearson IV distribution [21, 111], which is an adapted gaussian profile. Besides the range and the straggle, the profile is described by two additional parameters: the *skewness*, which accounts for the asymmetry in the distribution, and the *kurtosis*, which accounts for the flattening of the peak. Figure 3.4 shows a contour plot of the implantation profiles in a TJSC from Pearson IV calculations. The data were obtained from the commercially available process simulator TSUPREM-4 [97].

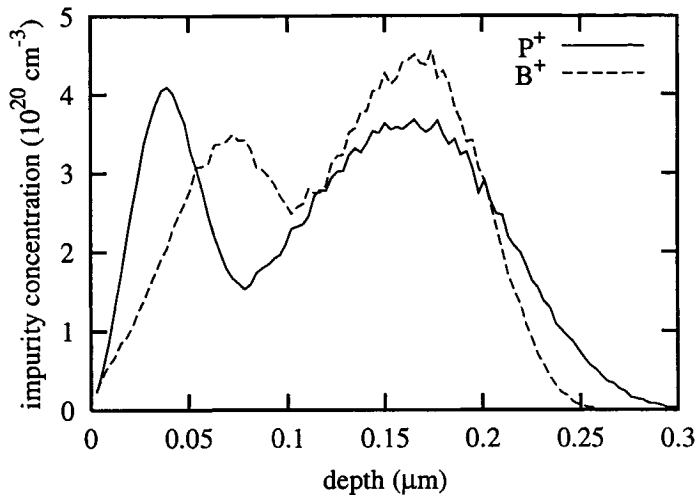


Figure 3.3: Monte-Carlo simulations in TRIM of the longitudinal impurity profiles of implanted phosphorus and boron using the parameters in Table 3.1. The plot covers the calculation of 100,000 ion trajectories for each dopant at each energy.

With Pearson IV distributions the impurity concentration can be studied over more decades than with Monte-Carlo simulations. The drawback of calculating the implantation profile from Pearson distributions is that the projected ranges are based on empirical data. Therefore, the method is less flexible than Monte-Carlo calculations, *e.g.*, the tilt angle (Sect. 2.5) and the mass density of *a*-Si:H have not been taken into account.¹

3.3 Doping mechanism in *a*-Si:H

The doping mechanism in *a*-Si:H is quite different from that in crystalline semiconductors. In *c*-Si a substitutional dopant, like phosphorus, is fourfold coordinated in the crystal lattice. One of the valence electrons of phosphorus is not involved in bonding and is released to the conduction band. Amorphous semiconductors do not have such a rigid network and impurity atoms can also be bonded in a threefold or fivefold coordination as a neutral atom. According to Mott's $8 - N$ rule, which predicts the lowest energy configuration of molecular bonds, both boron and phosphorus are preferentially threefold coordinated as a neutral atom [79]. However, due to thermodynamic fluctuations, a neutral doping atom can exchange a valence electron with a neutral Si atom, thereby creating a negatively charged dangling

¹The mass density is ~ 2.27 g/cm³ for *a*-Si:H with 10 at. % H and 2.33 g/cm³ for *c*-Si. The Pearson distributions in TSUPREM-4 are based on parameters of *c*-Si.

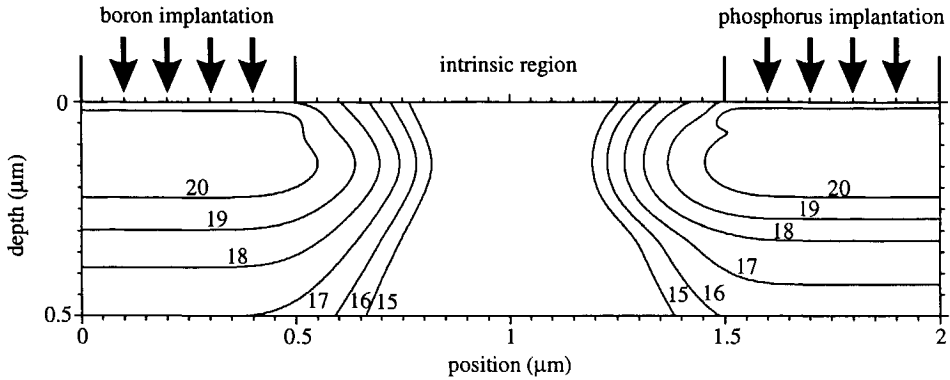


Figure 3.4: Contour plot of the implantation profiles of the TJSC in $\log(N_{\text{imp}}) \text{ cm}^{-3}$. The plot was calculated by TSUPREM-4 using Pearson IV distributions and the data in Table 3.1.

bond [77]. For example, in case of phosphorus doping, this reaction yields



It has been confirmed experimentally that the density of dangling bonds increases with the doping concentration [78]. Another important consequence of this doping mechanism is that the *active* impurity concentration is proportional to the square-root of the total doping concentration in the gas phase [86],

$$N_D \propto C_g^{\frac{1}{2}} . \quad (3.4)$$

This result can be derived from the law of mass action for Eq. 3.3 [77].

When *a*-Si:H is doped by ion implantation, additional defects are introduced by the bombardment of the material with highly energetic particles. These defects can be removed by annealing, although the required annealing temperature can be up to 300~400°C for 'complete' recovery [57]. In this sense, complete recovery means that the defect density and the Urbach energy are equal to those for *a*-Si:H doped in the gas phase. Annealing has two effects on implanted *a*-Si:H: removal of defects and activation of the dopants. For phosphorus implanted at an energy of 30 keV, it was found that below a *critical dose* of $\sim 10^{15} \text{ cm}^{-2}$, the dark conductivity decreases upon annealing for one hour at 250°C and above this dose, the dark conductivity increases [105]. We have also observed that annealing has a minor effect on the dark and photoconductivity and the activation energy. The TJSC is implanted near the critical dose as described by Ref. [105] (Table 3.1).

B ⁺		P ⁺	
energy (keV)	dose (cm ⁻²)	energy (keV)	dose (cm ⁻²)
40	5×10 ¹⁵	110	5×10 ¹⁵
15	1.5×10 ¹⁵	25	1.5×10 ¹⁵

Table 3.1: Parameters of the ion implantations for the fabrication of TJSC's.

3.4 Properties of ion implanted *a*-Si:H

3.4.1 Introduction

This section studies the influence of the implantation dose on the electrical and optical properties of boron and phosphorus implanted *a*-Si:H. Characterisation of the separate regions of the TJSC is important in order to understand the characteristics of the device and is essential when the device is modelled.

The key parameters of ion implantation are the type of dopant, the implantation energy, and the dose. Boron and phosphorus were chosen, since boron was the only *p* type dopant available and phosphorus is the lightest *n* type dopant of silicon. Heavier dopants, such as arsenic and antimony, require a higher energy to penetrate to the same depth and induce more damage in the *a*-Si:H network. The implantation energy can be varied to change the depth and shape (*i.e.*, straggle) of the implantation profile. The dose determines the doping concentration.

The experiments were carried out with 320 nm thick *a*-Si:H layers on Corning 7740 glass substrates. The implantation energy was fixed and the dose was varied (see Table 3.2). After implantation, the samples were annealed for 1 h at the deposition temperature of the layer (193°C). Planar aluminium contacts were evaporated with a length of 20 mm and 0.5 mm spacing. The data are presented as a function of the doping concentration, which was derived from the dose, using TRIM simulations (see Table 3.2).

3.4.2 Optical absorption

The absorption was measured as a function of the photon energy, using RT and DBP measurements (Sect. 2.6.1). Figure 3.5 shows the absorption curves calculated from these measurements.

The optical band gap (E_{Tauc}) and the Urbach energy were derived from the absorption data. The undoped reference sample has an E_{Tauc} of 1.77 eV. The boron doped samples have an E_{Tauc} decreasing from 1.73 eV to 1.64 eV with increasing doping concentration. Although the inaccuracy in the determination of E_{Tauc} is ~ 0.05 eV, the variation in the Tauc energy was clearly observed in plots of the Tauc relation (Eq. 2.1). The phosphorus doped samples have an E_{Tauc} of ~ 1.68 eV without a clear dependence on the concentration. The reduction

	E (keV)	dose (cm^{-2})	E (keV)	dose (cm^{-2})	N_{imp} (cm^{-3})
B ⁺	40	2×10^{13}	15	6×10^{12}	$\sim 10^{18}$
	40	2×10^{14}	15	6×10^{13}	$\sim 10^{19}$
	40	2×10^{15}	15	6×10^{14}	$\sim 10^{20}$
	40	2×10^{16}	15	6×10^{15}	$\sim 10^{21}$
P ⁺	110	2×10^{13}	25	6×10^{12}	$\sim 10^{18}$
	110	2×10^{14}	25	6×10^{13}	$\sim 10^{19}$
	110	2×10^{15}	25	6×10^{14}	$\sim 10^{20}$
	110	2×10^{16}	25	6×10^{15}	$\sim 10^{21}$

Table 3.2: Implantation doses and energies of the samples. The column on the right-hand side indicates the order of magnitude of the resulting profile from simulations in TRIM (cf. Fig. 3.3).

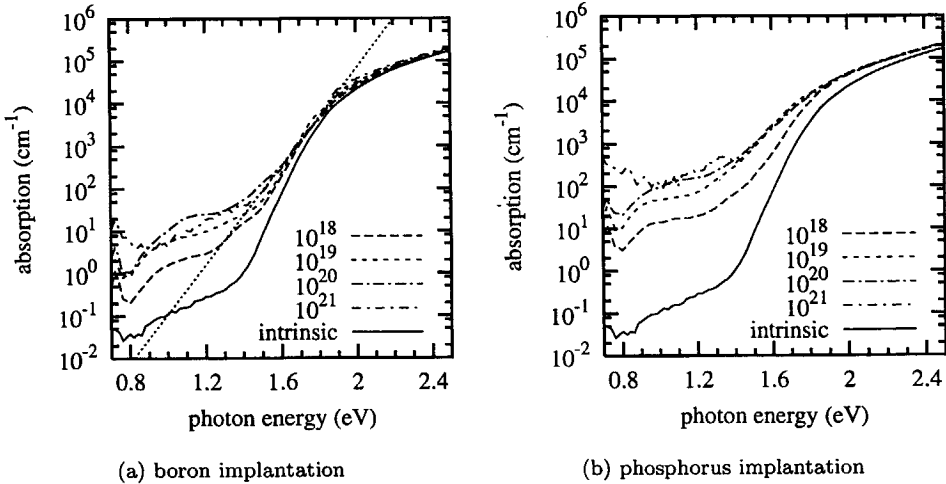


Figure 3.5: Absorption of a -Si:H implanted with different boron (a) and phosphorus (b) concentrations (in cm^{-3}). The dotted line in (a) is a guide of the eye with an exponential decay of 75 meV, corresponding to the Urbach energy at moderate doping levels.

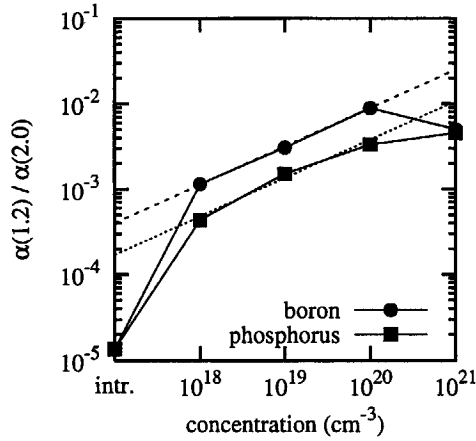


Figure 3.6: Dangling-bond density derived from the absorption data at 1.2 eV and 2.0 eV of Fig. 3.5. The dashed line is a fit of the boron doped samples; the dotted line is a fit of the phosphorus doped sample in the range $10^{18} < N_{\text{imp}} < 10^{20} \text{ cm}^{-3}$.

of the band gap is an indication of structural changes in ion implanted $a\text{-Si:H}$. Boron is known to reduce the optical band gap [35, 49], which is ascribed to enhanced strain in the $a\text{-Si:H}$ network [35]. Samples which were phosphorus doped from the gas phase (with PH_3) did not give rise to a noticeable change in the optical band gap with respect to undoped $a\text{-Si:H}$. The reduction of the band gap in phosphorus implanted $a\text{-Si:H}$ has also been reported in literature and is ascribed to a reduction of the hydrogen concentration [18]. Damage introduced by implantation of Si can be removed by annealing for concentrations up to 10^{20} cm^{-3} . However, at higher doses, the initial material properties can only be restored by post-hydrogenation [20]. This means that after implantation with a high dose of phosphorus, the hydrogen concentration has decreased.

The Urbach energy was determined from the absorption curves in Fig. 3.5. This energy increases with increasing doping concentration from 60 meV to 80 meV for the boron implanted samples and from 70 meV to 110 meV for the phosphorus-implanted samples. The Urbach energy of the undoped reference sample is 47 meV.

The absorption at 1.2 eV is a measure of the dangling bond density. Figure 3.6 shows the absorption at 1.2 eV with respect to the absorption of the extended states (at 2 eV). Evidently, the dangling-bond density increases with increasing doping concentration. At moderate concentrations, the dangling-bond concentration is related to the impurity concentration, N_{imp} , as

$$N_{db} \propto (N_{\text{imp}})^{\beta_{db}}. \quad (3.5)$$

The curves in Fig. 3.6 are fitted with an β_{db} of 0.45. The auto-compensation model for doping predicts a β_{db} of 0.5 (see Eq. 3.4) [77, 86]. This model is also applicable

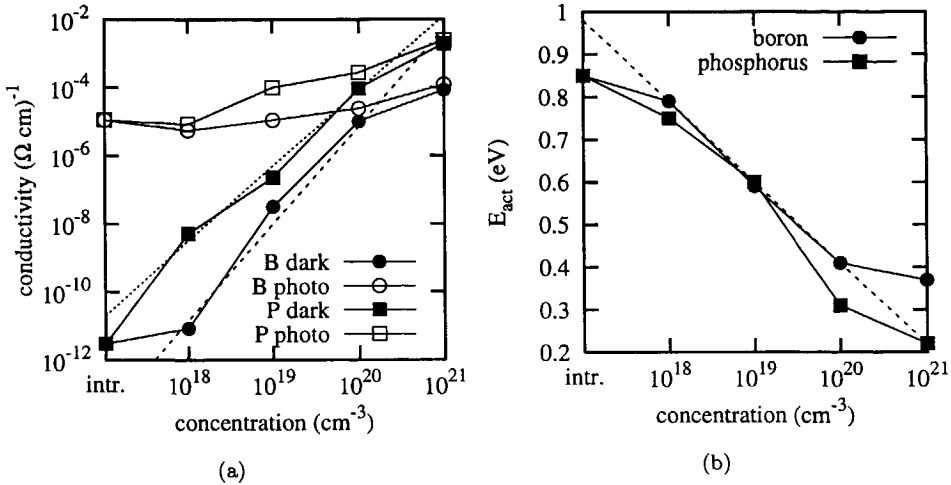


Figure 3.7: (a) Activation energy and (b) dark and photoconductivity of boron and phosphorus ion implanted a -Si:H at different doping concentrations. The dashed lines are fits of the boron doped samples; the dotted line is a fit of the phosphorus doped sample in the range $10^{18} < N_{\text{imp}} < 10^{20} \text{ cm}^{-3}$.

to ion implanted a -Si:H [53].

3.4.3 Electrical properties

Figure 3.7 shows the dark and photoconductivity data and the activation energy of a -Si:H doped by boron and phosphorus implantation. At the lowest doping concentration, the photoconductivities are lower than in intrinsic a -Si:H. This is due to the enhanced defect density in ion implanted a -Si:H, giving an increase in the recombination. The doping efficiency of phosphorus is higher than of boron, because, the conduction band tail is steeper than the valence band tail.

For a comparison to gas-phase doped a -Si:H, the slope of the dark conductivity curves in Fig. 3.7.a is examined. The data were fitted to the relation

$$\sigma_d \propto (N_{\text{imp}})^\beta. \quad (3.6)$$

Rough estimates of β yield ~ 2.2 for the phosphorus doped samples and ~ 2.9 for boron doped samples. Spear and Le Comber [74] plotted the conductivity of boron and phosphorus doped a -Si:H as a function of the doping concentration in the gas phase, giving a slope of ~ 1.6 for boron and ~ 1.1 for phosphorus doping at moderate doping levels. For a comparison to ion implanted material, the gas-phase concentration has to be related to the solid-phase concentration. Therefore, we

have to multiply the slope in the data of Spear *et al.* by two, according to Eq. 3.4. Then we obtain comparable values of β for gas-phase doped and ion implanted a -Si:H, both for boron and for phosphorus doping.

The activation energy is plotted as a function of the doping concentration in Fig. 3.7.b. The activation energy of intrinsic a -Si:H is about 0.85 eV. This means that the Fermi level lies 0.05~0.10 eV above the centre of the band gap. The fact that the intrinsic Fermi level is not at mid-gap results from the asymmetric distribution of defect states. The curve of the boron doped samples in Fig. 3.7.b has a more or less exponential dependence on N_{imp} for moderate concentrations ($10^{18} < N_{\text{imp}} < 10^{20} \text{ cm}^{-3}$). The curve of the phosphorus implanted samples does not exhibit a well defined exponential slope. Fitting the curve of the boron doped samples to

$$E_{\text{act}} \propto \gamma_{\text{imp}} \ln N_{\text{imp}} \quad (3.7)$$

yields a γ_{imp} of -83 meV.

3.4.4 Discussion

In the analysis of the experimental results, we will only consider the data for the boron doped samples. The results for phosphorus doped samples are not suitable to analyse quantitatively. At first sight, the slope of the E_{act} vs. N_{imp} curve (Fig. 3.7.b) seems to be related to the Urbach energy: 83 meV vs. 75 meV. In the following, a relation between these two values is derived.

The activation energy of p -type a -Si:H is defined as $E_{\text{act}} \equiv E_f - E_v$. The active (*i.e.*, ionised) acceptor concentration, N_A , is balanced by positive charge in the form of free holes, empty states in the valence band, and empty dangling bond states (D^+ states). Hence, from the charge-neutrality condition we obtain

$$N_A(E_f) = p(E_f) + \int_{E_{fi}}^{E_f} f_{fd}(E) N_{vb}(E) dE + N_{db}(E_f). \quad (3.8)$$

The first term is the hole density in the valence band,

$$p = N_v \exp\left(\frac{-E_{\text{act}}}{kT}\right), \quad (3.9)$$

the second term denotes the DOS in the valence band tail between the intrinsic Fermi level and E_f , yielding

$$\int_{E_{fi}}^{E_f} f_{fd}(E) N_{vb}(E) dE \approx N_{v0} E_{v0} \exp\left(\frac{-E_{\text{act}}}{E_{v0}}\right), \quad (3.10)$$

where N_{v0} is the DOS at the valence band edge. We assume that all dangling bonds are in the positively charged D^+ state, which we will demonstrate later.

For the dangling bond density, N_{db} , we use a result of the defect-pool model of Powell and Deane (Sec. 7.2.1) [62],

$$N_{db} = \text{const.} \times \exp\left(\frac{-E_{\text{act}}}{2E_{v0}^*}\right). \quad (3.11)$$

The term E_{v0}^* denotes the characteristic energy of the valence band tail at the equilibration temperature, T^* . This energy depends on the temperature by [62, 85]

$$E_{v0}^2(T) = E_{v0}^2(T=0) + (kT)^2. \quad (3.12)$$

At $T^* = 500$ K, E_{v0}^* is 82 meV. The defect density for device-quality intrinsic *a*-Si:H is typically $10^{15} \sim 10^{16}$ cm⁻³, so the prefactor in Eq. 3.11 is $10^{20} \sim 10^{21}$ cm⁻³.

In order to study the influence of each term in Eq. 3.8, the derivative of this equation is expressed as

$$\gamma_A = \left[\frac{d(\ln N_A)}{dE_{\text{act}}} \right]^{-1}. \quad (3.13)$$

The exponential slopes are $-kT$ in Eq. 3.9, $-E_{v0}$ in Eq. 3.10, and $-2E_{v0}$ in Eq. 3.11. The prefactors in Eqs. 3.9–3.11 are comparable, so the term with the largest slope dominates. Hence,

$$\gamma_A \approx 2E_{v0}^*. \quad (3.14)$$

This result illustrates that the change in the Fermi level is essentially induced by the dangling bond density [86]. Equation 3.14 can be verified by numerical simulations with ASA. In thermal equilibrium, the Poisson equation is solved for a single layer of *p*-doped *a*-Si:H. The activation energy is varied and the corresponding N_A is calculated. The defect-pool model is used to determine N_{db} in an iterative procedure, keeping $E_{v0} = 75$ meV (the Urbach energy). Figure 3.8 shows the calculated N_A , N_{db} and the charge density in the valence band tail, the dangling bond states, and the total charge density. This figure shows that it is correct to assume that all dangling bonds are positively charged in *p*-type *a*-Si:H. At moderate doping levels ($E_{\text{act}} > 0.4$ eV, *i.e.*, $N_{\text{imp}} < 10^{20}$ cm⁻³), the active doping concentration is indeed dominated by N_{db} . The slope of the N_{db} *vs.* E_{act} curve is 163 meV. This value corresponds well to γ_A in Eq. 3.14. The charge density in the valence band tail has a slope of 74 meV, corresponding to E_{v0} . This charge influences N_A at high doping concentrations only.

For a comparison to the experimental value γ_{imp} , we apply the result of Street's auto-compensation model, *i.e.*, $N_A \propto (N_{\text{imp}})^{0.5}$, which gives $\gamma_{\text{imp}} = 0.5\gamma_A \approx E_{v0}^*$. The slope of the curve in Fig. 3.7.b. is 83 meV, which is very close to value of E_{v0}^* as calculated from Eq. 3.12, using the experimental Urbach energy of 75 meV. This result supports two important findings. First, this analysis provides a direct verification of an important result of the defect-pool model, namely the dependence of the defect density on the slope of the valence band tail [62]. Second, it shows

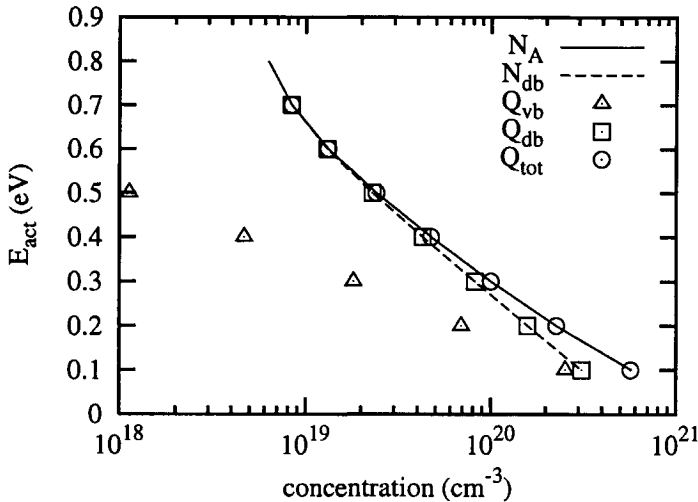


Figure 3.8: Simulated acceptor concentration, dangling bond concentration, and charge densities in the valence band tail and the dangling bond states, in thermal equilibrium, using the defect-pool model [62].

that Street's auto-compensation model [77] is also consistent for ion implanted a -Si:H [53]. A comparable analysis was carried out by Müller *et al.* [54] and Galloni *et al.* [18]. They both fitted their models to experimental results by varying some key parameters of the defect density. We have used the defect-pool model of Powell and Deane [62], which is consistent with the experimental dependence of N_{db} on E_{v0} in boron doped a -Si:H, although the validity of this model is limited to a small range of doping concentrations. Our approach gives direct evidence that in doped a -Si:H, the position of the Fermi level is determined solely by the charge density in doping-induced defect states.

Applying this analysis to the dark conductivity (Fig. 3.7.a) implies that the value of β in Eq. (3.6) is equal to E_{v0}^*/kT . With an E_{v0}^* of 83 meV the slope yields 3.1, which is close to β fitted from the data in Fig. 3.7.a. and corresponds to the data of Spear *et al.* [74]. Note that in crystalline semiconductors, all doping atoms are completely ionised and the slope of the σ_d vs. N_d curve is essentially unity.

The analysis of the phosphorus implanted samples is hampered by the nonlinearity in the E_{act} vs. N_{imp} characteristics. Plots of the conductivity data and the activation energy do not exhibit a well defined linear part for n-type a -Si:H [54, 74]. This can be ascribed to the fact that in undoped a -Si:H, the Fermi level is closer to the conduction band edge than to the valence band edge. Hence, at relatively low doping concentrations N_D already deviates from N_{db} (*cf.* Fig. 3.8). Obviously, more data points are required to analyse the dependence of E_{act} on the phosphorus concentration.

Experimental analysis

4.1 Introduction

In this chapter, the external parameters of the TJSC are investigated as a function of the geometry of the device (see Sec. 2.7.1). Figure 4.1 shows the assignment of the parameters that describe the design of the TJSC. These parameters are used extensively in the text and the figures. Section 4.2 discusses the influence of the dimensions of the active region on the device performance. An important issue in the design of the TJSC is the ratio between the *active* area (*i.e.*, the illuminated surface of the intrinsic region), where photovoltaic conversion occurs, and the total area of the device. In the doped regions, the photo-generated charge carriers are not separated, so they do not contribute to the photocurrent. In order to maximise the efficiency, the area of the doped regions has to be minimised. This topic is discussed in Sec. 4.3. Section 4.4 analyses a technique to reduce the area loss of the doped regions by illuminating the device from the bottom side through a transparent substrate. The quantum efficiency is studied in Sec. 4.5 and finally, the properties of the metal contacts are studied in Sec. 4.6.

It must be stressed that it is not the aim of this thesis to present an optimised device; this research project is a feasibility study of the TJSC. From that point of view, this section gives some helpful clues for an *eventual* device optimisation. Furthermore, the experiments are analysed in order to acquire more understanding of the physical consequences of a transverse junction in a solar cell.

4.2 Width of the active region

A characteristic feature of the TJSC is that the width of the intrinsic region, W , can be varied without changing the optical properties. This width is one of the most important parameters in the optimisation of the electrical system of the TJSC. The area of the intrinsic region (and hence W) must be maximised with respect to the area of the doped regions, since the photovoltaic conversion occurs

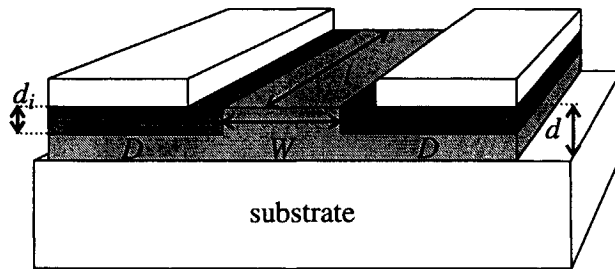


Figure 4.1: Schematical drawing of the a -Si:H TJSC with the definition of some relevant design parameters.

in the intrinsic region only (*i.e.*, the active region).

Figure 4.2 shows the external parameters of the TJSC as a function of W . These parameters were derived from I - V curves measured under AM1.5 illumination (*cf.* Fig. 2.5). The data are taken from TJSC's on c -Si wafers with layer thicknesses of 500 nm for the a -Si:H layer and 550 nm for the underlying SiO_2 . The length of the junction, l , is 3 mm. The mask set used for the lithographic patterning contains four different sizes of the width of the intrinsic region. The defined values of W are indicated on the horizontal axis of the graphs. The error bars shown in the figure represent the lowest and the highest values measured on five sets of cells at arbitrary positions on one wafer. The circles are the average results. Section 4.3 discusses possible inaccuracies in W .

The data points of the cells with a W of $0.4 \mu\text{m}$ are significantly different from the wider cells, in particular the V_{oc} . The relatively poor performance of these cells can be deduced from the dark I - V curves of a set of cells with different W 's (Fig. 4.3). The cell with a W of $0.4 \mu\text{m}$ has a very high saturation current with respect to the larger cells. Probably the intrinsic region is so narrow that the implantation profiles overlap (see Sec. 3.2). The dark I - V measurements will be discussed extensively in Sec. 7.3.

The short-circuit current is plotted in Fig. 4.2.a. A current of $0.2 \mu\text{A}$ corresponds to a *lateral* current density of $13.3 \text{ mA}/\text{cm}^2$. However, in order to compare this value to conventional solar cells, the illuminated area should be taken into account. In that way, the current yields 6.6 mA per cm^2 active area, for a $1 \mu\text{m}$ wide intrinsic region. A conventional a -Si:H solar fabricated at DIMES produces an J_{sc} of $\sim 17 \text{ mA}/\text{cm}^2$ and has a V_{oc} of $0.80\sim 0.83 \text{ V}$.

The V_{oc} of $\sim 0.80 \text{ V}$ is on average slightly lower than the V_{oc} of conventional *pin* solar cells, based on the same intrinsic layer. The exact origin of the V_{oc} is not completely understood [34], since it depends on a number of device parameters. First of all, the V_{oc} depends strongly on the quality of the doped regions. The activation energy of the n region of the TJSC ($\sim 0.28 \text{ eV}$) is higher than in gas-phase doped a -Si:H ($\sim 0.16 \text{ eV}$) and probably the mobility band gap is smaller (see

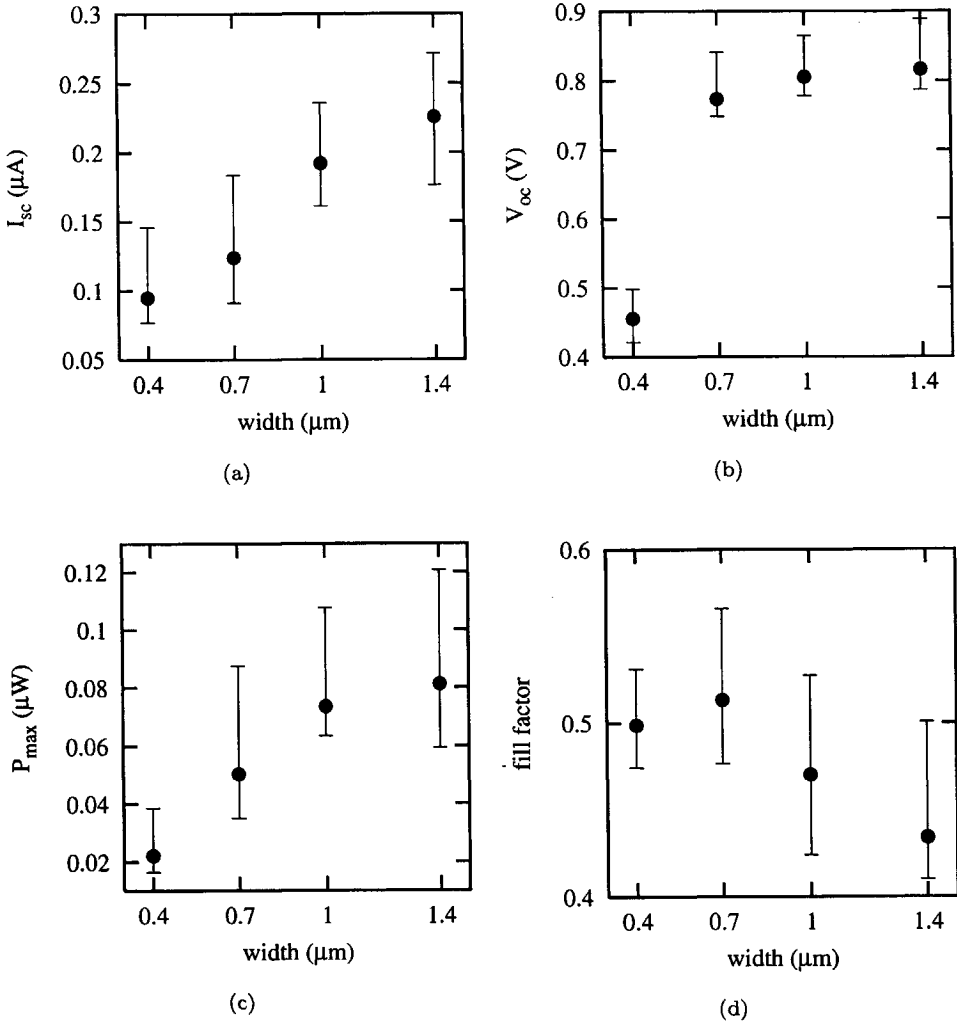


Figure 4.2: Averaged external parameters of five sets of TJSC's on one wafer, as a function of the width of the intrinsic region. The error bars indicate the lowest and the highest measured values.

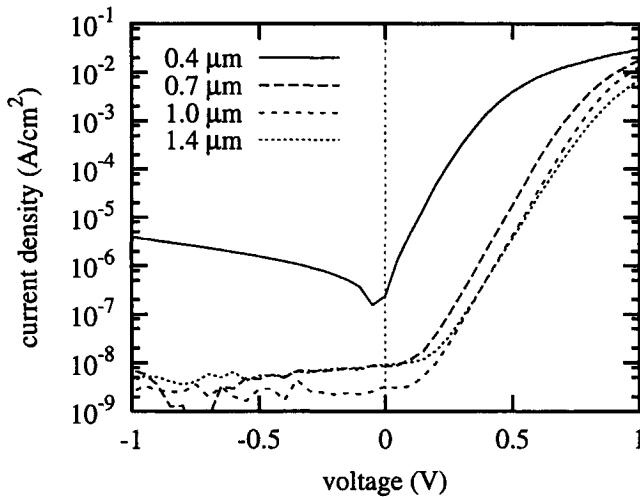


Figure 4.3: Dark I - V curves of a set of TJSC's with different widths of the intrinsic region.

Sec. 3.4.2). The p region has an activation energy of ~ 0.38 eV and also a smaller band gap as compared to conventional solar cells. In the latter, the a -SiC:H p layer has a wider band gap than a -Si:H, giving rise to a potential barrier that prevents the excess electrons in the intrinsic layer to penetrate into the p layer. Furthermore, the V_{oc} depends on the illumination intensity.

The fill factors of $0.4\sim 0.5$ are relatively low. Conventional pin solar cells have a FF of ~ 0.7 . The fill factor is a good measure of the quality of the 'electrical system' of the solar cell, as it reflects the recombination under operation conditions. The low value of the fill factor is inherent to the two-dimensional lay-out of the TJSC. In a conventional solar cell, most of the incoming light is absorbed in the region under the p/i interface. The holes have the shorter lifetime of the two types of charge carriers. Hence, the design of a conventional solar cell is chosen such that the holes travel the shortest distance before being collected in the p layer. In the TJSC, however, the average path length in the intrinsic region is $W/2$ for both holes and electrons. Moreover, most of the photo-generated holes have to pass the defect-rich p/i interface region. As a result, the collection efficiency is lower in a TJSC. This is illustrated by a modelling experiment in which the external parameters of a conventional cell are studied as a function of the shape of the generation profile. A conventional pin solar cell was simulated in ASA using the material parameters of Table B.2.¹ First, the generation profile of a conventional cell was used (Fig. 5.1). This simulation yielded a V_{oc} of 0.84 V, an

¹The defect pool model was used in these simulations [62], in order to describe the enhanced defect density near the p/i interface and i/n interface.

J_{sc} of 12.3 mA/cm², and a FF of 0.72. Then the same structure was simulated with a uniform generation rate of 1.53×10^{21} cm⁻³s⁻¹, which was chosen such that J_{sc} matches. This situation corresponds to the generation profile in a TJSC. In this simulation, the V_{oc} was almost the same (0.83 V), however, the FF had decreased to 0.66. This is the result of the longer path length of generated holes.

The general trend is that the V_{oc} and the I_{sc} increase with increasing W . Obviously, when W is increased, the number of generated electron-hole pairs increases (leading to an increase in I_{sc}) and more electron-hole pairs are separated, thereby increasing the space charge (leading to an increase in V_{oc}). A larger W yields more recombination and this is reflected by a reduction of the fill factor.

4.3 Efficiency considerations

4.3.1 Initial efficiency

The efficiency is calculated from the power output at maximum power point (Fig. 4.2.c). The measured cells have very large doped regions which could be much smaller in practical applications. Therefore, only the area of the active (*i.e.*, intrinsic) region is taken into account. Thus, the efficiency is defined as

$$\eta = \frac{P_{\max}}{(l \times W)P_{\text{ill}}}, \quad (4.1)$$

where P_{ill} is the intensity of the AM1.5 spectrum (100 mW/cm²). This equation gives efficiencies as plotted in Fig. 4.4. The data points are the mean values obtained from the measurements of five identical cells. The error bars indicate the lowest and the highest values measured. The best result was obtained with a cell with a W of 0.7 μm , having an efficiency of 4.2%. The maximum of the averaged values is in between 0.7 and 1.0 μm .

Previously, an efficiency of $5.2 \pm 1.4\%$ was reported on a TJSC with a W of 0.56 ± 0.14 μm [44]. The errors in those results (*i.e.*, the inaccuracy of W) were estimated from the inaccuracies of the lithographic process (*i.e.*, overlay and line width inaccuracies). However, those results were obtained with devices which were fabricated with another wafer stepper. For the present experiments, a more sophisticated wafer stepper was used [1], having a higher resolution and a better alignment accuracy. The errors are determined differently. In the present experiments, the inaccuracy of W has not been taken into account, because, even if W could be determined accurately, the distance between the interfaces with the doped regions cannot be defined exactly. This is due to the lateral profile of the ion implantation (Sec. 3.2).

The cell efficiency is lower when the entire area of the TJSC is taken into account, including the doped regions. At first sight, the width of the doped regions, D is determined by the resolution of the lithographic process. However, there is also a physical limit to D : the peak value of the gaussian profile in the lateral

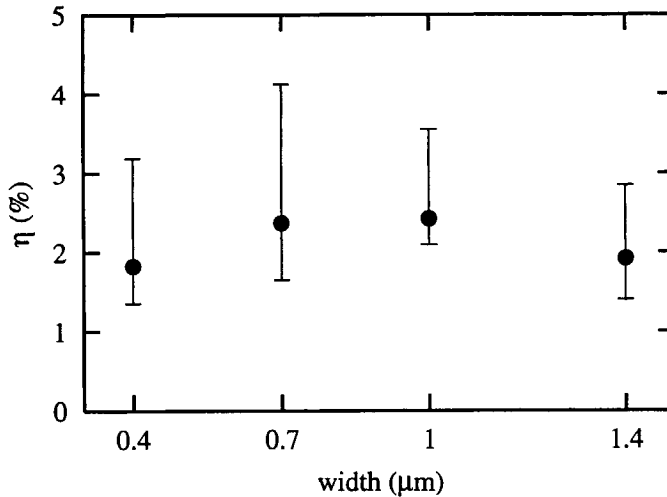


Figure 4.4: Efficiencies determined from Fig. 4.2.c using Eq. 4.1.

direction must be reached. The dopant atoms are implanted through an opening in the PR layer. As a result of scattering in the lateral direction (Sec. 3.2), the impurity concentration at the mask edge is half the 'peak' concentration (see Fig. 3.1) [21]. When the width of the mask opening, D , is too small, the lateral profiles at both sides overlap and the concentration does not reach its maximum in the center of the mask opening. Therefore, D must be at least two times the distance at which the gaussian function of Eq. 3.2 decreases to half the 'peak' value. Hence,

$$D^2 \geq 8\sigma_l^2 \ln 2. \quad (4.2)$$

With a σ_l of 50 nm (Fig. 3.2.b), Eq. 4.2 yields a minimum width of ~ 120 nm. This value is smaller than the resolution of the lithography ($0.5 \mu\text{m}$ [1]); therefore, under the present conditions, the lithography is the limiting factor in the reduction of the area of the doped regions.

In order to calculate the efficiency with respect of the total area of the device, we simply assume that the doped regions are as wide as the intrinsic region. In that case, the efficiency of the entire cell is one-third of the efficiency as calculated in Eq. 4.1. By using an interdigitated finger pattern for the doped regions with the intrinsic region meandering in between [41], the total efficiency is one-half of the efficiency calculated with Eq. 4.1.

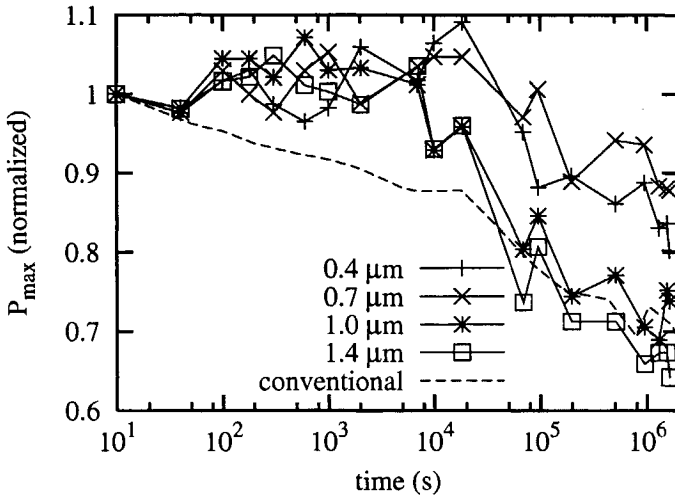


Figure 4.5: Normalised maximum power output as a function of time at continuous illumination of 1.3 suns at 50°C. For reference, the dashed line shows the degradation of a conventional α -Si:H *pin* solar cell with an intrinsic layer thickness of 450 nm.

4.3.2 Light-induced degradation

Degradation of the device performance is an important issue in the optimisation of the cell design. The metastability of defect states is basically a material property, however, the design of the solar cell is also an important factor. The light incoupling determines the generation rate in the cell and in conventional *pin* solar cells, there is a strong dependence of the degradation rate on the width of the intrinsic region [109], because the wider the intrinsic region, the higher the recombination rate.

The stability of TJSC's has been studied as a function of the width of the intrinsic region. Before degradation the cells were annealed for 1 hour at 150°C in order to assure a good starting point. The cells were degraded at 50°C with a white light intensity of $\sim 130 \text{ mW/cm}^2$ (1.3 suns). Figure 4.5 shows the power output, P_{max} , as a function of time, normalised to P_{max} in the initial state. The degradation rate increases with the width of the intrinsic region: after 10^6 s of light soaking, the power of the 0.4 μm wide cell decreases 17% and the cell with a W of 1.4 μm decreases 35%.

For comparison, a conventional *pin* solar cell was degraded under the same conditions. This intrinsic layer of this cell was deposited with the same process recipe and has a thickness of 450 nm. It is remarkable that this cell degrades faster than TJSC's with a similar size of the intrinsic region. This is due to the fact in the TJSC, the light incoupling is not as good as in conventional solar cells.

Simulations in ASA, using the optical model GENPRO1 [95], showed that the total generation in a 500 nm thick i layer, deposited on an oxidised silicon wafer is 70% of the total generation in a 450 nm thick conventional cell (*cf.* Fig. 5.1). According to the $G^{2/3}t^{1/3}$ relation for the creation of dangling bonds in a -Si:H [87, 88], the TJSC must be degraded twice as long in order to obtain the same defect density.

Another important difference is that most of the light is absorbed in the top part of the intrinsic region, so the degradation rate is higher. In conventional *pin* solar cells, all generated holes have to pass this part of the cell before collection. Spectral response measurements have shown that the initial collection efficiency is already low in the top part of the TJSC (*cf.* Sec. 4.5). Degradation mainly reduces the collection efficiency for blue light [14]; however, the *initial* blue response of the TJSC is already poor. The fill factors of the TJSC's reduced to ~ 0.35 for all cells.

4.4 Bottom side illumination

An alternative method to maximise the active area is to modify the design of the TJSC such that the illuminated surface consists entirely of intrinsic material. The doped regions can be positioned deeper in the cell, since most of the light is absorbed near the illuminated surface. Such a situation can be obtained by illuminating the cells from the bottom side through a transparent substrate, like glass [45]. Therefore, TJSC's have been fabricated on Corning 7740 glass wafers (Sec. A.3) with a design as depicted in Fig. 4.1, in which the layer thickness, d , is larger than the depth of the ion implantations, d_i . In the narrow intrinsic region between the doped regions and the substrate, the photo-generated carriers are collected as well, provided a built-in electric field exists in this part of the cell. This picture is very schematical; in practice, the doping concentration has a longitudinal profile (Fig. 3.3). It is evident that the doping profile will extend down to the substrate, however, if the doping level near the substrate is sufficiently low, the conditions for photovoltaic conversion can be met (*i.e.*, a built-in electric field and sufficiently long minority carrier lifetimes). In such a case we can speak of a 'quasi-intrinsic' region under the doped regions, in which the generated charge carriers can be collected.

Several sets of TJSC's were fabricated with different thicknesses of the a -Si:H layer and doping profiles as shown in Fig. 3.3. The width of the intrinsic region is 1 μm and the width of the doped regions, D , is also 1 μm . The length of the cells is 3 mm. The cells were first illuminated from the top side and then through the substrate. The I - V curves measured under these conditions are shown in Fig. 4.6 for cells with layer thicknesses of 200, 350, and 500 nm.

When comparing these data it should be kept in mind that at a glass/air interface the optical reflection is lower than at an a -Si:H/air interface. Therefore, the optical generation is higher when the cell is illuminated through the substrate. Simulations in GENPRO1 [95] show that the total generation (*i.e.*, the integral of the generation profile across the layer thickness) is 21% higher under substrate

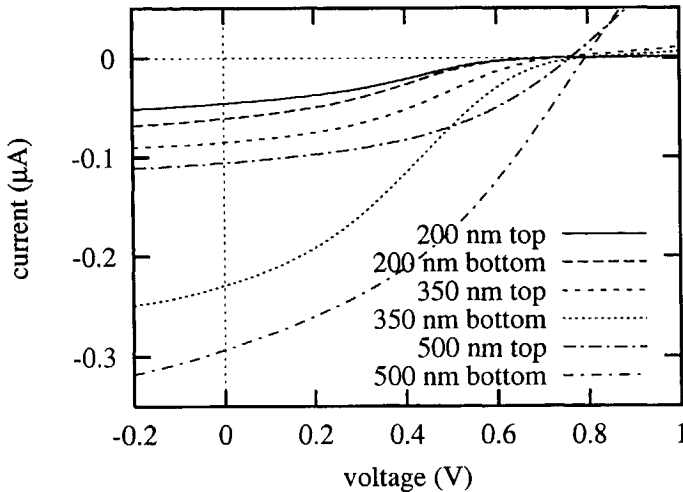


Figure 4.6: I - V Curves of TJSC's illuminated from the top side and through the glass substrate (bottom side). The cells have layer thicknesses of 200, 350, and 500 nm.

illumination as compared to top side illumination.

The 200 nm thick cell shows an increase in I_{sc} of 33% when it is illuminated through the substrate. Two-third of this increase can be ascribed to enhanced optical generation; the remaining part is caused by other effects, like the passivation of surface states. Furthermore, it should be noted that the shape of the longitudinal doping profile can probably influence the cell performance as well. The maxima in these profiles are located at a depth of ~ 170 nm, which is relatively close to the glass interface in the 200 nm thick cells. Besides, the longitudinal straggle of the deep implantation is larger than for the shallow (*i.e.*, low energy) implantation (Fig. 3.2). Figure 3.3 shows that at a depth of 200 nm, the doping concentrations are more than ten times higher, both for the phosphorus and the boron implantation. Therefore, in the 200 nm thick TJSC, the collection efficiency is probably higher near the bottom side than near the top side.

The thicker cells have a much larger difference in I_{sc} under top-side and bottom-side illumination: 169% for the 350 nm thick cell and 177% for the 500 nm thick cell. These differences are too large to be explained by the increased generation rate. Apparently, the active area of the device has increased and the difference between illumination from the top side and the bottom side is caused by extra collection of charge carriers generated under the doped regions. The 200 nm cell has a high doping level through the entire layer, without a quasi-intrinsic region underneath; hence, the area where photovoltaic conversion occurs is the same under top illumination and substrate illumination.

The other external parameters, *i.e.*, V_{oc} and FF , are not conclusive, since these

values are affected by the S -shape in the I - V curves of the cells of 200 and 350 nm thick. The S -shape is probably caused by the contact resistance, which will be discussed in Sec. 4.6.

The collection of charge carriers generated in the quasi-intrinsic regions requires a built-in electric field. When the field in these regions has a substantial lateral component, the electrons, generated under the p -type region, can drift towards the n -type region and be collected. The same applies for holes generated under the n -type region. When the lateral field component is absent, the 'minority' carriers will recombine and only the 'majority' carriers are collected. In order to study how far the internal electric field extends into the quasi-intrinsic regions, an experiment was carried out in which the width of the doped regions, D , was varied from 1 to 100 μm . In these cells, W is 1 μm and d is 350 nm. Five identical sets of TJSC's were measured under AM1.5 illumination from the top side and through the substrate. The external parameters were averaged for each size of the doped regions. Figure 4.7 shows the results of these measurements, where the error bars indicate the lowest and the highest values measured.

The effect of the direction of illumination is most pronounced in I_{sc} and P_{max} . Under substrate illumination, these parameters increase with increasing D up to 10 μm wide doped regions. Here I_{sc} is five times higher under substrate illumination than under top side illumination. At larger D , both I_{sc} and P_{max} seem to decrease slightly. Under top side illumination there is no clear dependence of the external parameters on D .

The open-circuit voltage is not directly related to D . However, the V_{oc} increases slightly with increasing photocurrent (i.e., I_{sc}). The cells with a D of 1 μm have a very low fill factor, which was ascribed previously to the contact resistance. Cells with larger doped regions have a larger contact area and a better I - V curve (without the typical S -shape), which is reflected by the higher fill factor. The fact that the fill factor is lower when the cell is illuminated through the substrate supports the assumption of carrier collection in the quasi-intrinsic regions. These regions have a relatively high defect density; hence, the recombination of 'minority' carriers will be higher than the recombination in the central intrinsic region. Therefore, the fill factor is lower in the quasi-intrinsic regions.

The same experiment was performed with cells having a thickness of 200 nm. The I_{sc} and fill factor are plotted in Fig. 4.8. The cells with a D of 1 μm suffer from the contact resistance and perform badly. The other cells are more or less independent of D . The cells with a D of 10 μm have a larger I_{sc} and a smaller FF than the other cells and this is the case in all experiments on glass wafers, both under top side illumination and under bottom side illumination. The high I_{sc} is probably due to a systematic error in the fabrication of the lithographic masks. There is no observable relation between D and the cell performance of the 200 nm thick cells, so we can repeat the previously drawn conclusion that in thin cells, only those carriers are collected which are generated in the quasi-intrinsic region in between the doped regions.

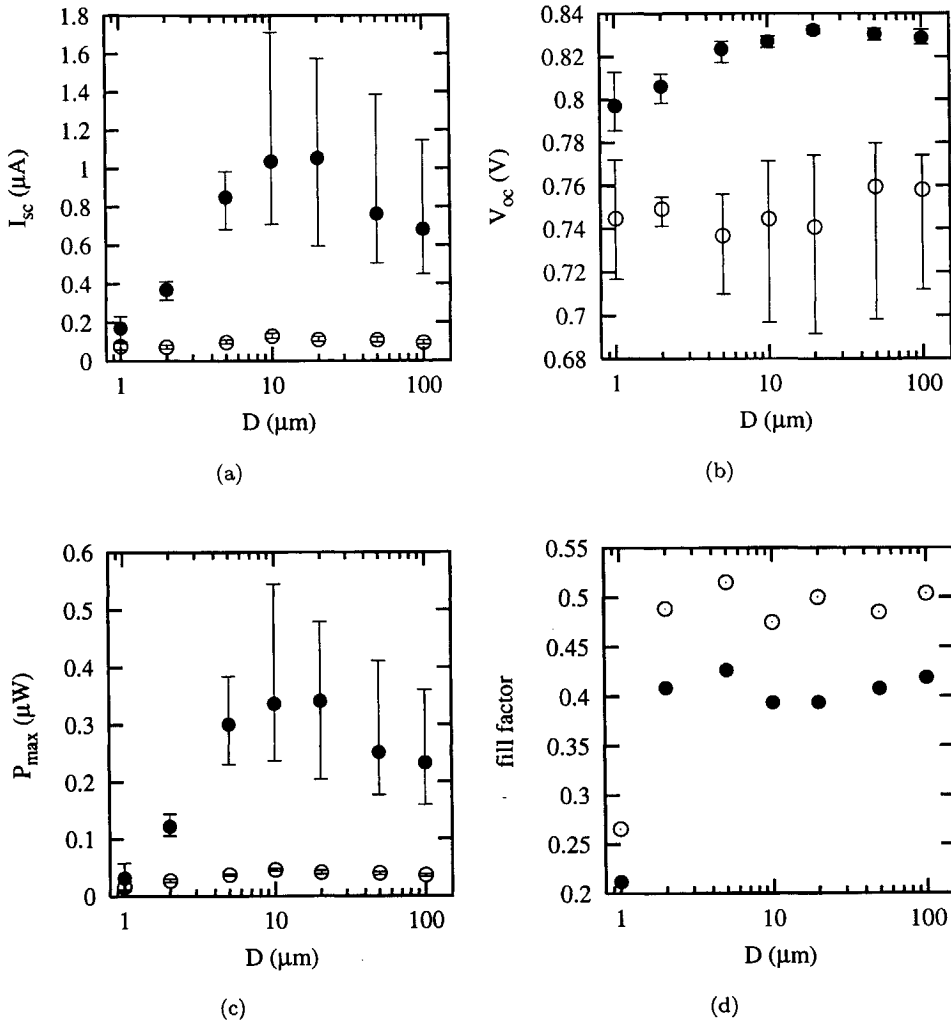


Figure 4.7: Averaged external parameters of five sets of TJSC's on a glass wafer, as a function of the width of the doped regions. The layer thickness is 350 nm. The open circles represent illumination from the top side; the closed circles represent illumination through the substrate. The error bars indicate the lowest and the highest values measured (for clarity, the error bars of the FF were removed, as they are smaller than the dot size).

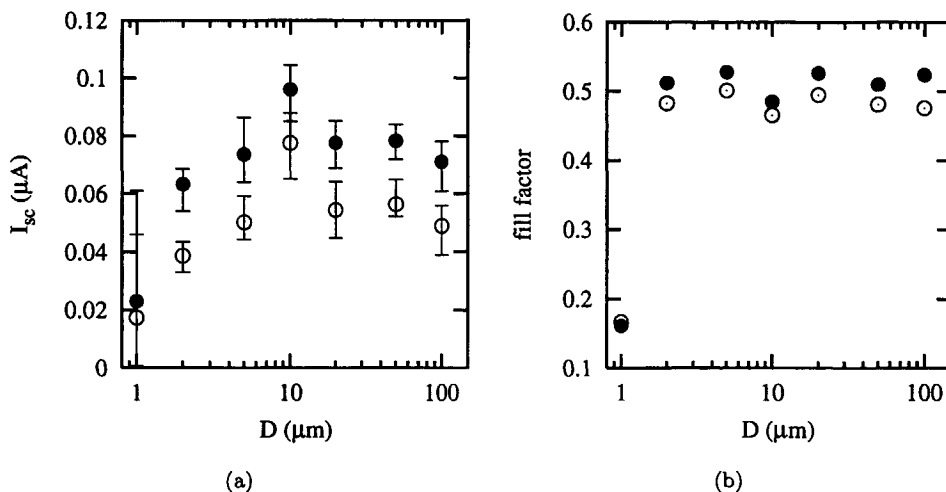


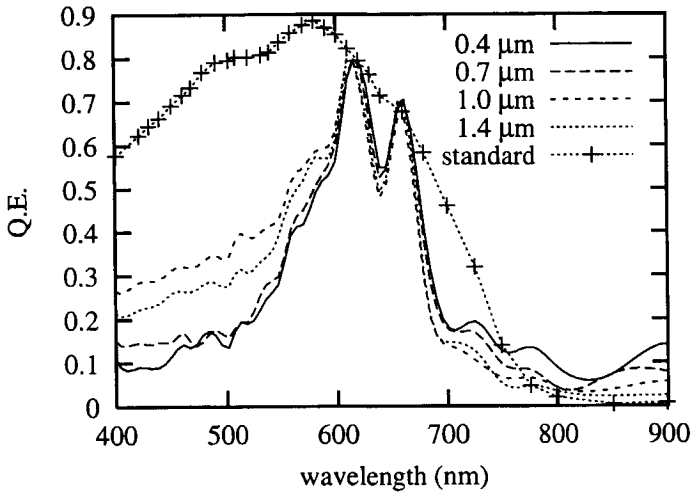
Figure 4.8: Short-circuit current and fill factor of 200 nm thick TJSC's under top side illumination and bottom side illumination. For additional explanation, see caption of Fig. 4.7.

4.5 Spectral response

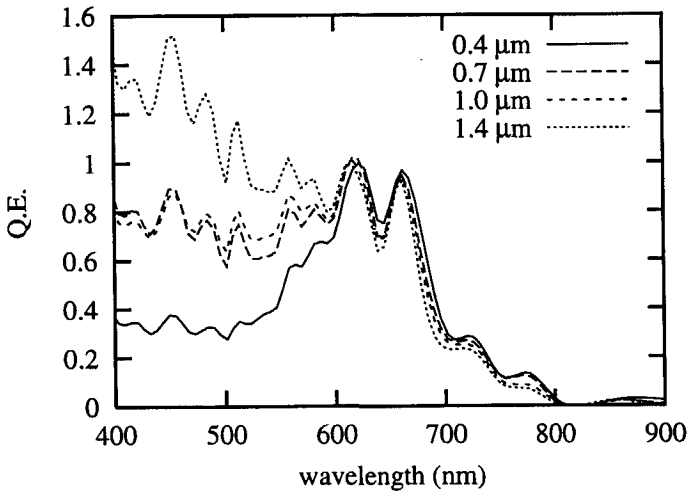
Figure 4.9 shows the external quantum efficiency at bias voltages of 0 V and -4 V of four TJSC's on silicon substrates with different W . The cells were illuminated from the top side. These measurements can only be used for a qualitative analysis, since the photon flux incident on the TJSC is unknown (Sec. 2.7.3). The QE curves of the TJSC's were scaled such that the maxima at ~ 620 nm coincide and that the shape of the curves can be compared with the quantum efficiency of a conventional a -Si:H *pin* solar cell with an *i*-layer thickness of 450 nm, a textured TCO and a silver back contact.

The most pronounced difference between the QE of the TJSC's and the conventional solar cell is the optical interference. A conventional cell has a complicated optical system with a textured TCO and a back reflector and the light is scattered in the cell. Hence, the interference is blurred. The TJSC has flat interfaces and less internal reflections; therefore, the interference fringes are much more pronounced. In the red part of the spectrum, the QE of the TJSC is relatively low. This shows the importance of a back reflector, which increases the optical path length of the longer wavelengths.

When W is increased, the blue response increases relatively to the red response. When a reverse bias voltage of 4 V is applied, this relative increase is enhanced. The difference between the external QE's at zero bias and at large negative biases



(a) bias = 0 V



(b) bias = -4 V

Figure 4.9: Scaled external QE data of TJSC's with different values for the width of the intrinsic region, (a) at zero bias and (b) at a reverse bias voltage of 4 V. The data were scaled in order to match the QE of the standard solar cell at 620 nm (crosses).

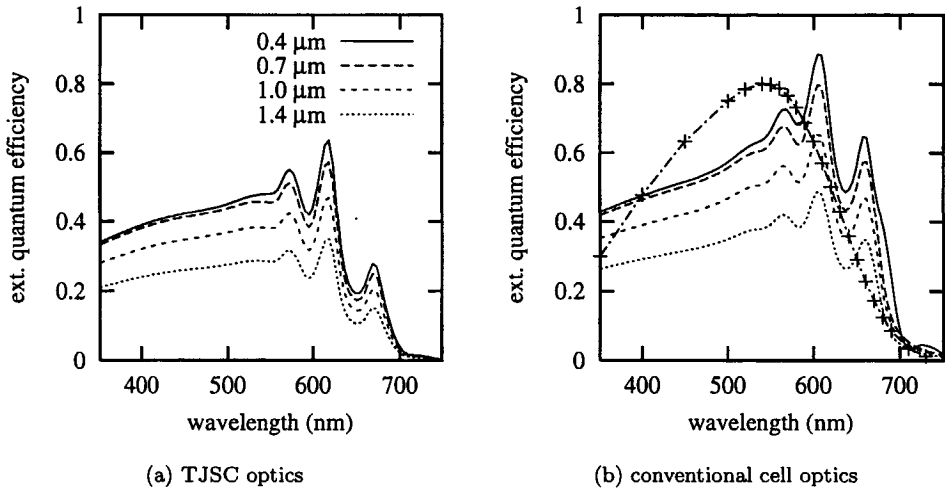


Figure 4.10: Simulated quantum efficiency of TJSC's with different W for (a) a 500 nm thick cell on an oxidised wafer and (b) a 500 nm thick cell with a glass/TCO surface and an Ag back reflector. The crosses in (b) represent the simulated QE of a conventional cell with an i -layer thickness of 450 nm.

is a measure of the collection efficiency of the generated electron-hole pairs (*i.e.*, the difference between the internal and the external QE). Hence, the different blue responses at 0 V and at -4 V indicate that there is virtually no internal electric field underneath the top surface, where blue light is absorbed. The doping concentrations are low under the surface and probably, the electric field is present only at that depth where the doping concentration is high (between, say, 100 and 200 nm deep). At this depth, the lateral doping profile penetrates far into the intrinsic region. Moreover, due to the presence of surface states, the defect density is higher in the part of the cell where blue light is absorbed. When a reverse bias is applied, the electric field persists in the entire intrinsic region, resulting in a higher QE in the blue part of the spectrum.

In order to obtain absolute data of the QE, numerical simulations were carried out. First, the generation profile was calculated in ASA for each wavelength using a constant photon flux ($10^{19} \text{ cm}^{-3}\text{s}^{-1}$).² These profiles were imported in MEDICI to calculate the corresponding photocurrents. The simulated data are shown in Fig. 4.10.a.

The simulations show a better blue response than the measured devices, as

²The optical model GENPRO1 was used [95], which takes optical interference into account. Using the Lambert-Beer equation [106, 110] results in QE curves of comparable shape and height, but without the interference effects.

comparison to the QE at ~ 600 nm. In the simulations, the doped regions are uniform, therefore, the electric field strength does not depend on the depth. Eventual surface charge has not been taken into account either.

The simulated external QE depends strongly on the width of the intrinsic region. This is solely caused by the collection efficiency, since the optical system does not depend on W . We face the problem again of how to define the active area of the TJSC. In these simulations, the entire surface in between the metal contacts was illuminated and this area was also considered in the calculation of the QE. The distance between the contacts is W plus $0.1 \mu\text{m}$ at each side of the intrinsic region. This margin was used in the experimental cells to account for the alignment inaccuracy of the lithographic process (*cf.* Sec. 2.4). If only the area of the intrinsic region would have been used in the calculations, the QE would exhibit a stronger dependence on W .

The computer model also allows an investigation of the effective losses in the efficiency, caused by the poor incoupling of light in the TJSC. Therefore, the QE was simulated for a set of TJSC's in which the optical system was replaced by the optical system of a conventional solar cell, *i.e.*, the generation of a conventional cell (without a p layer) was imported in the device structure of the TJSC. In these simulations, the light enters through 0.5 mm thick glass and 300 nm thick (untextured) TCO. The a -Si:H layer is 500 nm thick and has a silver back reflector underneath. The results are shown in Fig. 4.10.b. The QE increases with $25\sim 50\%$ for all wavelengths. However, below 600 nm, the quantum efficiency is still relatively low in comparison to conventional solar cells (fig. 4.10.b). The difference is due to the short lifetime of holes, which have to travel on average a larger distance towards the p -doped region ($0.5W$) than in conventional cells at short wavelengths. Note that the simulated QE of a conventional cell is not correct for small wavelengths. In MEDICI, the simulated electric field is too low near the p/i interface (Fig. B.2), resulting in a lower collection efficiency of blue light.

4.6 Contact properties

The influence of the metal/semiconductor contact properties on the device performance of a solar cell cannot be ignored. Especially under illumination, the internal resistance of the solar cell can be rather low in comparison to the contact resistance and therefore, it is important to have good ohmic contacts.

When a metal and a semiconductor are brought in contact with each other, a potential barrier arises in the semiconductor due to the difference in work functions of the metal and the semiconductor.³ There are two transport mechanisms of majority carriers across a potential barrier: thermionic emission and tunnelling. When thermionic emission occurs, the metal/semiconductor interface is a Schot-

³In a semiconductor, the relative energy towards the vacuum level is generally expressed by the electron affinity, χ . The work function is equal to χ plus the distance between the conduction band edge and the Fermi level.

tky contact having rectifying behaviour. Schottky contacts generally have a high resistance. When the potential barrier is sufficiently narrow, the majority carriers can tunnel through the barrier, resulting in a more or less ohmic contact with a relatively low contact resistance. An ohmic contact is obtained by

- combining a semiconductor and a metal with comparable work functions in order to obtain a low barrier potential;
- a high doping concentration near the interface in order to decrease the width of the space-charge region.

After deposition of the metal contacts, the device is annealed in order to passivate broken bonds at the metal/semiconductor interface. In case of (amorphous) silicon, aluminium is a good contacting material with regard to the difference between the work functions. However, Al is highly diffusive in Si and special precautions have to be taken to prevent Al diffusion during the contact anneal. Al is a *p*-type dopant in *a*-Si:H and the interaction of diffused atoms with the metastable *a*-Si:H network leads to crystallisation near the contact interface [28]. For conventional *pin* solar cells with a 20 nm thick *n* layer and an Al back contact, it was demonstrated that an anneal between 150°C and 170°C improves the contact properties [27]. However, above 180°C, the *a*-Si:H *n* layer crystallises at the contact interface and above 200°C, the entire *n* layer is counter-doped by Al.

The contacts of the TJSC are defined at a distance of ~ 100 nm from the intrinsic region. This distance is chosen such that even with a large alignment inaccuracy, the contact does not cover the active region. This distance is sufficiently far from the active region that eventual counter-doping of the *n*-region will not deteriorate the *pin* junction. Hence, as a result of the relatively large distance between the contact and the active region of the cell, the thermal budget for annealing the contacts is higher than for conventional solar cells. In order to verify this reasoning, an experiment was carried out in which as-fabricated TJSC's were annealed for one hour at different temperatures. However, we did not observe a change in the device characteristics within a temperature range varying from 150°C to 220°C.⁴ From this result we conclude that annealing the cells for one hour at 150°C is sufficient to obtain good ohmic contacts and that eventual counter-doping or crystallisation does not harm the performance of the TJSC.

The shallow ion implantations (*i.e.*, at the lowest energies for each element in Table 3.1) are of crucial importance for the contact properties. Normally, the ion implantations are carried out at two different energies for each of the dopants. When the shallow implantation is omitted, the *I-V* curve under AM1.5 illumination becomes *S*-shaped (Fig. 4.11.a). This particular shape can be explained by Schottky effects occurring at low current densities. The short-circuit current hardly changes, indicating that the collection efficiency is not affected. The cells which do have shallow implantations exhibit good ohmic contacts. The influence

⁴In these experiments, the deposition temperature of the *a*-Si:H layer was 220°C.

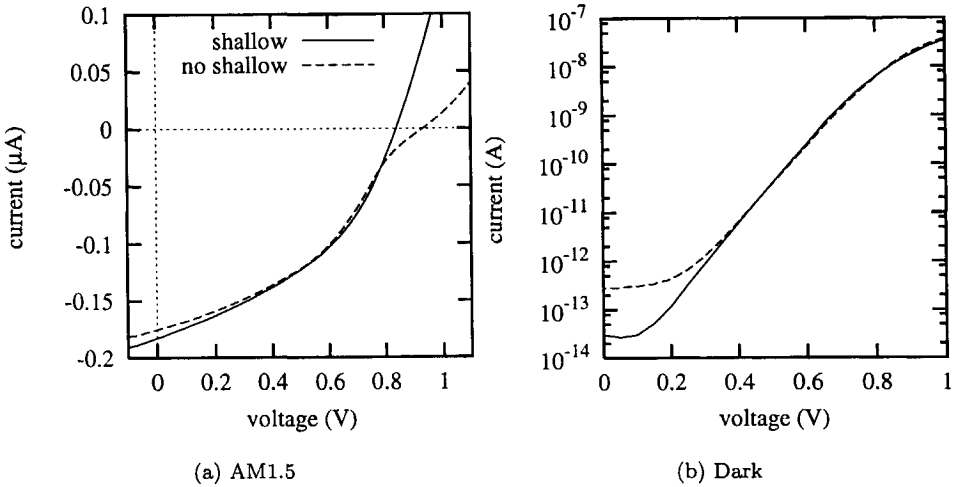


Figure 4.11: Current–voltage characteristics of a -Si:H TJSC's with and without shallow implantations (*i.e.*, the boron implantation at 15 keV and the phosphorus implantation at 25 keV in Table 3.1).

of the shallow implantations is also evident from the dark I - V curves (Fig. 4.11.b). The saturation current increases by one order of magnitude when the shallow implantations are omitted. Probably this is due to leakage currents between the contacts and the intrinsic region.

4.7 Discussion and conclusions

The most characteristic properties of the a -Si:H TJSC have been presented in this chapter. An important issue is the variation of the external parameters of the cells on the width of the intrinsic region, W . The best result was obtained for a cell with a W of $0.7 \mu\text{m}$, having an efficiency of 4.2%, calculated on the active area of the solar cell. This cell has the highest fill factor and degrades significantly less under light soaking than the wider cells. Theoretically, the smaller W , the better the cell performance. However, the smallest cell, having a W of $0.4 \mu\text{m}$, has a low V_{oc} and a high leakage current, which is due to the lateral straggle of doping atoms into the intrinsic region. The spread in the experimental results is relatively large. Obviously, the cell performance has a strong dependence on inaccuracies in the fabrication, *i.e.*, the optical lithography.

From the spectral response measurements it is evident that additional measures should be taken in order to improve the blue response of the TJSC. A

surface passivation and an anti-reflection coating enhance the blue response. Note that these conditions are met when the cell is illuminated from the bottom side, through a glass substrate. For example, the 200 nm thick TJSC's on glass exhibit a 33% higher power output under bottom side illumination than under top side illumination. The enhancement is for approximately two-third ascribed to a better incoupling of light (*i.e.*, the generation rate is 21% higher) and for one-third, *i.e.*, 12% of the total power, caused by other effects, *a.o.* the passivation of surface states by the glass substrate and the higher doping level in the doped regions near the surface of illumination.

When the implantation energy and layer thickness are chosen such that the depth of the profile is substantially smaller than the layer thickness, a 'quasi-intrinsic' region is present under the 'doped' regions. This quasi-intrinsic region increases the active area of the device, resulting in an increase of the short-circuit current up to five times. However, this is at the expense of a lower collection efficiency, which is reflected by the lower fill factor.

The main function of the shallow implantations is to improve the contact properties and to prevent a leakage current from the contact directly into the intrinsic region. The short-circuit current and the fill factor are not improved by these implantations.



Device simulations

5.1 Introduction

In this chapter, some specific features of the TJSC are studied by numerical simulations. These simulations were carried out with ASA when possible, *i.e.*, when a one-dimensional simulation grid is appropriate. Some effects can only be investigated using a two-dimensional structure and those simulations were carried out with MEDICI. Appendix B contains a detailed comparison of both device simulators and discusses the suitability of MEDICI to simulate a -Si:H devices.

The main purposes of device simulations are

- **Parameter extraction.** By using inverse modelling routines [59], unknown parameters of the device or the material can be obtained by fitting the simulated device characteristics to experimental data.
- **Device optimisation.** Once a set of reliable parameters is found and proper physical models are available, the numerical model acquires predictive power. Hence, the design parameters of the device can be varied in simulations in order to optimise its performance.
- **Comprehensive analysis.** Device simulators have the possibility to plot the relevant internal parameters, like the band diagram, recombination, electric field, *etc.* The study of these parameters facilitates the understanding of the behaviour of the device under many different operating conditions.

The geometry of the experimental TJSC's is not known exactly and not all of the necessary parameters of a -Si:H can be measured accurately. Hence, we cannot employ the predictive power of simulations. However, the simulated structure, the physical models, and the material parameters are sufficiently accurate to study the operation principles of the TJSC and to compare the TJSC to conventional a -Si:H solar cells. Therefore, the modelling efforts in this work are mainly focussed on the last point.

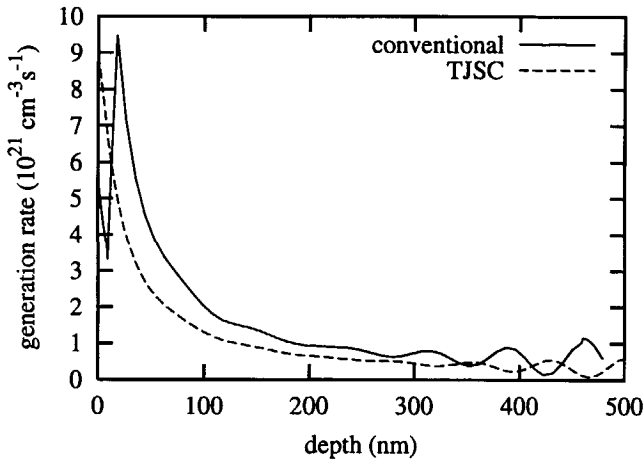


Figure 5.1: Optical generation profiles of a conventional a -Si:H solar cell and the TJSC under illumination from the top side. The profiles were obtained from simulations in ASA under the AM1.5 spectrum, using GENPRO1.

5.2 Vertical effects

One of the objectives of this research project was to construct a solar cell in which the electrical system and the optical system can be optimised independently. However, it is likely that the electrical system is inhomogeneous in the vertical direction, *i.e.*, perpendicular to the surface of illumination. For example, the optical generation and the doping concentration have a pronounced dependence in the vertical direction.

Figure 5.1 shows the optical generation profiles of a conventional a -Si:H solar cell and the TJSC. These profiles were obtained from simulations with ASA with the GENPRO1 model [95] under illumination with the AM1.5 spectrum. The cell has a p-type a -SiC:H layer of 9 nm thick, a 450 nm intrinsic layer, and a 20 nm thick n-type a -Si:H layer on a 0.5 mm Corning glass substrate. A 300 nm thick TCO contact was chosen on the front side and 200 nm thick silver on the back side. The TJSC has an a -Si:H layer thickness of 500 nm, a 550 nm silicon-oxide layer underneath, and a c -Si substrate. Note that in a practical solar cell, the generation rate will be higher, since the optical model GENPRO1 assumes flat interfaces, whereas a real solar cell has a textured TCO front contact. Both cells have a similar exponential decay as a function of depth, although in the conventional cell, the average generation rate is almost 30% higher (excluding the doped layers), caused by the better incoupling of light through the glass/TCO substrate and the silver back contact.

When the activation energy of the doped regions would be determined solely

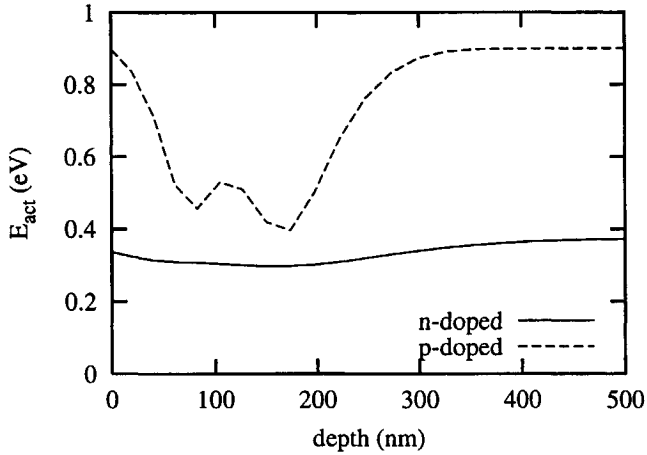


Figure 5.2: Activation energy as a function of depth in the ion implanted regions of the TJSC.

by the *local* doping concentration, a gaussian doping profile would give rise to a parabolic activation energy as a function of depth (Eq. 2.6). However, in case of non-uniform doping, the free charge carriers experience a built-in potential, resulting in local depletion and accumulation of the free carriers. Figure 5.2 shows the activation energy as a function of the depth in the doped regions of the TJSC, calculated by solving the Poisson equation in MEDICI. The profile of E_{act} in the *n* region is flattened due to a redistribution of charge. In the *p* region, however, E_{act} has a clear dependence on the doping profile, because the Fermi level is pinned by the high charge density in the valence band tail. This effect results in a large variation in the activation energy as a function of depth.

The remainder of this section discusses two-dimensional simulations in MEDICI to study the consequences of the optical generation and the doping profile.

One modelling experiment was carried out to compare the vertical profiles of the activation energy to uniformly doped regions with a varying depth, d_i (*cf.* Fig. 4.1). All other geometry parameters were kept constant: $d = 0.5 \mu\text{m}$, $W = 1.0 \mu\text{m}$, and $l = 3 \text{ mm}$. The material parameters for intrinsic *a*-Si:H were used for the doped layers as well (see Table B.2) and the doping concentrations were chosen such that the activation energy is 0.40 eV in the *p* doped region and 0.30 eV in the *n* doped region. Table 5.1 shows the simulated external parameters of these cells.

Another TJSC was simulated with longitudinal doping profiles. These profiles consist of two gaussian functions with longitudinal ranges and straggles which were obtained from Fig. 3.2. These are for boron at 15 keV: $R_p = 40 \text{ nm}$ and $\sigma_p = 15 \text{ nm}$, at 40 keV: $R_p = 150 \text{ nm}$ and $\sigma_p = 50 \text{ nm}$, and for phosphorus at 25 keV:

d_i (μm)	V_{oc} (V)	I_{sc} (μA)	FF
0.1	0.76	0.017	0.48
0.2	0.78	0.020	0.50
0.3	0.79	0.022	0.50
0.4	0.80	0.025	0.49
0.5	0.82	0.027	0.49
<i>long.</i>	0.78	0.021	0.44

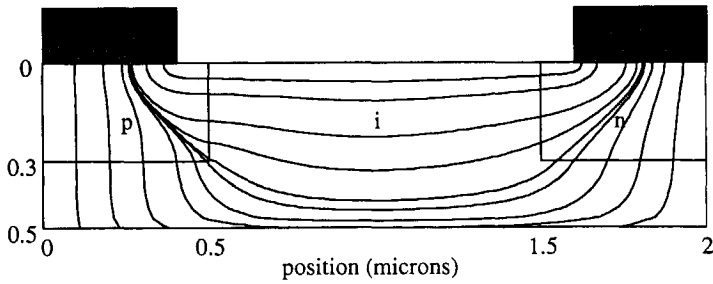
Table 5.1: External parameter simulated in MEDICI. The doping concentration is uniform and the depth of the doped regions, d_i , was varied. Other structure parameters are (cf. Fig. 4.1): $d = 0.5 \mu\text{m}$, $W = 1 \mu\text{m}$, $D = 1 \mu\text{m}$, and $l = 3 \text{mm}$. This series of cells is compared to a cell having a longitudinal doping profile.

$R_p = 40 \text{nm}$ and $\sigma_p = 15 \text{nm}$, and at 110 keV: $R_p = 150 \text{nm}$ and $\sigma_p = 50 \text{nm}$. The V_{oc} and the I_{sc} are comparable to a cell with a d_i of $0.2\sim 0.3 \mu\text{m}$. The fill factor is significantly smaller than the cells with uniformly doped regions. A lower fill factor is an indication of enhanced recombination. Possibly, the generated carriers have to travel a larger distance before being collected by the doped regions. The trajectories of the generated carriers can be studied by simulations of the electric field.

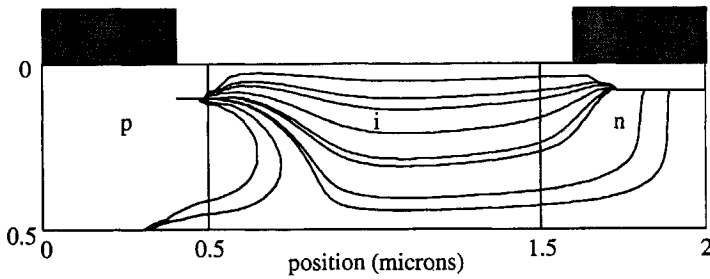
Figure 5.3.a shows the electric field lines of a TJSC in thermal equilibrium. This graph was obtained using the material parameters of Table B.2 and device dimensions (cf. Fig. 4.1): $W = 1 \mu\text{m}$, $D = 0.5 \mu\text{m}$, $d = 0.5 \mu\text{m}$, and $d_i = 0.3 \mu\text{m}$. The latter value was chosen such that I_{sc} and V_{oc} correspond to a simulated TJSC with longitudinal doping profiles (Table 5.1, Sec. 5.2). In the upper part of the intrinsic region, the electric field is in the lateral direction. Deeper in the cell, the limited depth of the ion implanted dopants affects the electric field, resulting in a small vertical component.

The simulation of the electric field lines was also carried out for a structure with a doping profile in the longitudinal direction (Fig. 5.3.b). With these profiles, the electric field is essentially different from the previous case. The potential difference between the maxima in each doping profile is larger than between the contacts, in case of zero bias voltage. This result is interesting, because it means that it is beneficial for the solar cell performance to assure that the peak in the activation energy is very close to the contact. All generated charge carriers are collected at that point in the doped regions where the doping concentration has a maximum and the closer this point to the contact, the shorter the average path length of the generated carriers. This explains the lower fill factor of the simulated TJSC with a longitudinal doping profile (Table 5.1).

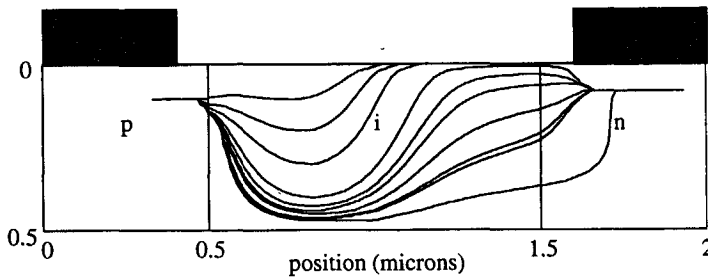
The electric field changes drastically when the cell is illuminated (Fig. 5.3.c). In that case, the electric field has a substantial vertical component. Evidently, illumination induces additional positive charge in the p/i interface region. This



(a) thermal equilibrium



(b) with longitudinal profile



(c) illuminated

Figure 5.3: Electric field lines simulated in MEDICI for a TJSC in thermal equilibrium (a), as (a) with a longitudinal doping profile (b), and as (b) under AM1.5 illumination at I_{sc} (c). The device dimensions are (cf. Fig. 4.1): $W = 1 \mu\text{m}$, $D = 0.5 \mu\text{m}$, and $d = 0.5 \mu\text{m}$.

charge is caused by

- Excess electrons and holes which are generated in equal concentrations, however, electrons are collected easier than holes, because they have a higher drift mobility.
- The changed occupation level of the dangling bond states under illumination.

Simmons and Taylor gave an elucidate description of the occupation of defect levels under nonequilibrium conditions in terms of the quasi-Fermi levels [73]. Under illumination, the Fermi level splits into quasi-Fermi levels for electrons and holes, E_{fn} and E_{fp} , respectively. Below E_{fp} , all states are occupied, between E_{fp} and E_{fn} , the states are partially occupied, and above E_{fn} all states are empty [73, 106]. In the larger part of the intrinsic region, the Fermi level is in the upper part of the band gap. The dangling bond states have an energy in between E_{fp} and E_{fn} (when the cell is illuminated), hence, the occupation level these states decreases under illumination. Hence, the concentration of positively charged dangling bond states increases when the cell is illuminated. In the upper part of the cell, the generation rate is higher, resulting in more positive charge than in the lower part of the cell. This difference in space-charge density induces a vertical component in the electric field of a TJSC under illumination.

The vertical component in the electric field is a serious drawback of the design of the TJSC and harms its performance. Under normal operating conditions, a solar cell is forward biased, yielding a smaller built-in electric field. Hence, the relative contribution of the vertical field component becomes even larger.

5.3 Lateral straggle

The external parameters of the smallest measured cell (in which $W = 0.4 \mu\text{m}$) differ significantly from the larger cells (Fig. 4.2). The V_{oc} is very low in comparison to the larger cells and the fill factor of ~ 0.5 is slightly lower than expected (the smallest cell should have the highest FF). The dark $I-V$ measurements of the smallest cell exhibit a deviating dark $I-V$ behaviour as well: the saturation current is more than one order of magnitude larger than in the wider cells, indicating a high leakage current. A possible reason for the anomalies at a W of $0.4 \mu\text{m}$ is the lateral straggle of the doping atoms from the doped regions into the intrinsic region (Sec. 3.2). This section gives an impression of the influence of lateral straggle of doping atoms on the performance of the TJSC. This is done by one-dimensional simulations in the lateral direction.

The shape of the lateral doping profile is difficult to determine experimentally. Hence, we have to make some guesses for the grading parameters. According to Monte-Carlo simulations (Sec. 3.2), the lateral profile has a more or less gaussian profile as described in Eq. 3.2 [21]. Simulations in TRIM give a lateral straggle, σ_l , of 50 nm for both boron implanted at 40 keV and phosphorus implanted at 110 keV

(see Fig. 3.2.b). In order to obtain the profile of the active doping concentrations, we use the results derived from Fig. 3.6,

$$\begin{aligned} N_{A,D} &\sim N_{db} \approx \sqrt{N_{imp}} \\ &= C \exp\left(\frac{-y^2}{4\sigma_l^2}\right). \end{aligned} \quad (5.1)$$

The prefactor C was chosen such that the activation energies are 0.40 and 0.30 in the bulk of the p region and n region, respectively.

Besides the straggle, it is also important to know the range of the profile in the lateral direction, *i.e.*, the distance into the intrinsic region at which doping atoms influence the material properties. The active doping concentration is more or less proportional to the defect density, N_{db} , (Sec. 3.4.4). At implantation doses of $\sim 10^{15}$ cm $^{-2}$, it follows from Table 3.2 and Fig. 3.6 that N_{db} is ~ 300 times higher in phosphorus implanted a -Si:H and ~ 1000 times higher in boron implanted a -Si:H with respect to undoped a -Si:H. The lateral range can be calculated from the distance at which N_A and N_D decrease to 10^{-3} and 3×10^{-2} of the maximum concentration, respectively. According to Eq. 5.1, such a reduction occurs in a lateral range of 240~260 nm, taking $\sigma_l = 50$ nm. These values are in agreement with the experimental observations: the cells with a W of 0.4 μm are affected by an overlap of the lateral straggles, whereas the cells with a W of 0.7 μm do have a 'pure intrinsic' part in between the doped regions. Consequently, the ranges of the lateral straggle must be in between 200 nm and 350 nm (assuming equal ranges for boron and phosphorus implantations).

The simulations were carried out with ASA using the parameters listed in Table B.2. In the doped regions, a uniform doping concentration was used. The active doping concentrations and the defect density were graded into the intrinsic region according to Eq. 5.1 with a σ_l of 50 nm. For the structure with a W of 0.4 μm , N_{db} is 3.8×10^{16} cm $^{-3}$ in the centre of the intrinsic region, due to the overlap of both doping profiles. The characteristic energy of the valence band tail depends on the logarithm of the defect density [62, 84]. A gaussian grading would then yield a parabolic dependence of E_{v0} on y . However, ASA only allows linear grading of E_{v0} and E_{c0} , so we have assumed a linear grading of the band tails between these values in the intrinsic region and the doped regions. These gradings extend over a range of 250 nm.

Figure 5.4 compares the band diagrams in thermal equilibrium for a -Si:H pin junctions with abrupt and with graded interfaces. The width of the intrinsic region is 0.4 μm , since at this size, the effect of the lateral straggle is post pronounced. Both the dark I - V and the I - V curve under illumination were simulated, the latter with a uniform generation rate of 1×10^{21} cm $^{-3}$ s $^{-1}$, corresponding to the generation rate in a TJSC at a depth of 200 nm. The results are listed in Table 5.2. Obviously, a gaussian doping profile results in a higher electric field in the center of the intrinsic region than when abrupt interfaces are used. In that case, the

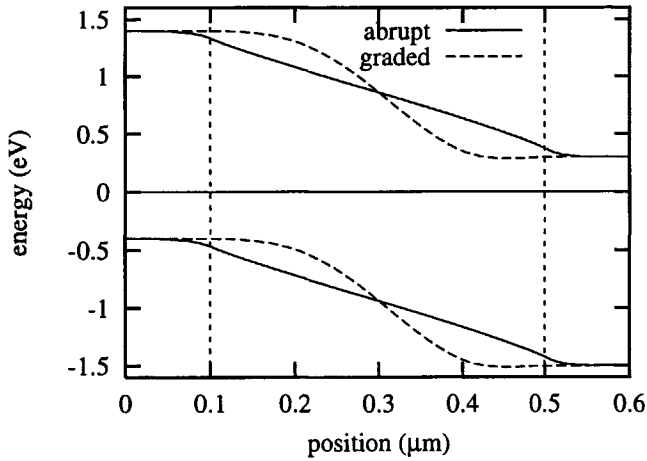


Figure 5.4: Band diagrams in equilibrium of a a -Si:H pin diodes with abrupt doping interfaces (indicated by the vertical dashed lines), with gaussian grading of the doping concentration, and with gaussian grading of both the doping profile and the DOS.

bands are more strongly bent near the p/i interface and the i/n interface. The depletion region is effectively narrower. This effect reduces I_{sc} , because the 'active area', where photovoltaic conversion occurs, is smaller. For a cell with a W of $0.7 \mu\text{m}$, the effectively smaller depletion region yields *less* recombination, thus increasing the fill factor and reducing the ideality factor of the dark I - V curve. In the simulated cell with a W of $0.4 \mu\text{m}$, the defect density is higher in the centre of the cell, resulting in *more* recombination. The leakage current increases, resulting in an increase of J_0 by one order of magnitude. However, the V_{oc} of the $0.4 \mu\text{m}$ wide cell is hardly affected by the lateral grading. In the experiments of Sec. 4.2 the V_{oc} of the $0.4 \mu\text{m}$ wide cell is very low. We did not take into account the fact that the lateral straggle is a function of the depth (*i.e.*, the longitudinal profile). However, we have restricted ourselves to one-dimensional simulations, since these provide a better insight into the influence of the lateral straggle of dopants.

5.4 Conclusions

From the simulation experiments presented in this chapter, the following conclusions can be drawn

1. The longitudinal doping profile cannot be described properly by a uniformly doped region with an effective depth, d_i . The short-circuit current and the open-circuit voltage can be matched with a d_i of $0.2\sim 0.3 \mu\text{m}$, however, the fill factor is lower. This is due to the fact that in case of longitudinal doping

<i>parameter</i>	$W = 0.4 \mu\text{m}$		$W = 0.7 \mu\text{m}$	
	<i>abrupt</i>	<i>graded</i>	<i>abrupt</i>	<i>graded</i>
V_{oc} (V)	0.82	0.80	0.83	0.83
I_{sc} (mA/cm ²)	7.6	4.6	11.4	8.7
FF	0.73	0.67	0.65	0.71
J_0 (10 ⁻¹² A/cm ²)	2.2	16	5.4	1.9
m	1.66	1.63	1.67	1.58

Table 5.2: Parameters of simulated one-dimensional α -Si:H *pin* solar cell with $W = 0.4$ and $0.7 \mu\text{m}$ with abrupt interfaces and with gaussian grading of the doping concentration and the DOS parameters. The illuminated characteristics were simulated with a uniform generation rate of $1 \times 10^{21} \text{ cm}^{-3} \text{ s}^{-1}$.

profiles, the electric field is pointed towards the maxima of the boron and phosphorus profiles.

2. The inhomogeneous optical generation as a function of depth gives rise to a higher space-charge density in the top of the TJSC (near the surface of illumination). Hence, the electric field has a substantial vertical component.
3. The lateral scattering of doping atoms results in an effectively narrower space-charge region. This effect enhances the collection efficiency in the centre of the intrinsic region, however, the active area of the TJSC is smaller.



Series Connections

6.1 Introduction

The open-circuit voltage of solar cells is up to 0.6 V for *c*-Si based and 0.80~1.0 V for single-junction *a*-Si:H solar cells. For many applications this voltage is too low and the cells have to be connected in series. Conventional solar cells have contacts on the front side and the back side of the device and in order to establish a connection between two cells, an interconnect must be made which connects the front contact of one cell to the back contact of the next cell. The most commonly used technique for monolithic series connections is by selective laser scribing (see Fig. 6.1) [56]. This technique is used three times in a production process: after depositing the TCO front contact, after depositing the *a*-Si:H *pin* structure, and after depositing the metal back contact. The laser intensity is tuned such that the underlying layers are not affected. The typical line width for laser scribing is 50 μm . Each layer is patterned at a different position, such that the groove in the *a*-Si:H layers is filled by the back contact. At this position the back contact is connected to the TCO. The TCO's of two adjacent cells are isolated, since the *a*-Si:H layers in between have a relatively high resistivity.

The TJSC has planar contacts. This feature allows series connections of TJSC's without additional process steps [43]. The relative simplicity of fabricating arrays of TJSC's is inherent to the lateral design. This chapter discusses series connected arrays of TJSC's and in particular the interconnects between adjacent cells. Section 6.2 discusses arrays in which the interconnect is formed by the junction between the *n* region of one cell and the *p* region of the adjacent cell. Section 6.3 discusses arrays in which the connection is established by a thin aluminium bar that covers the *np* junction. Series connections consisting of 2 up to 100 cells have been fabricated and are compared with the characteristics of a single cell. This comparison provides information on the electrical losses of an interconnect.

In literature, several solar cells were reported with a lateral design in order to facilitate series connections. The *c*-Si vertical multi-junction solar cell was

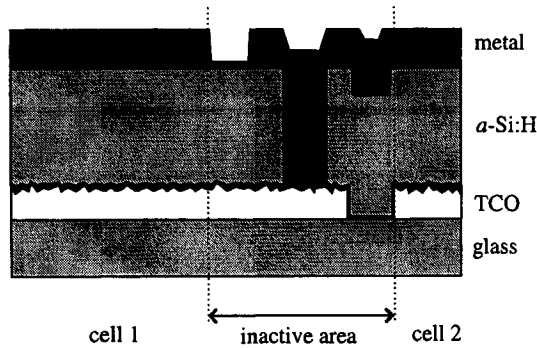


Figure 6.1: Schematic drawing of a monolithic series connection of conventional $a\text{-Si:H}$ solar cells. Note that the drawing is not on scale.

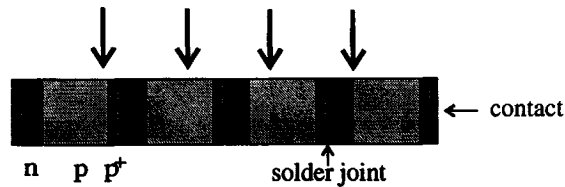


Figure 6.2: Schematic drawing vertical multi-junction solar cell (after Fahrenbruch [15]).

developed in 1976 in order to obtain a high output voltage [15]. The lay-out of such a solar cell array cell is shown in Fig. 6.2. This array consists of 50~100 crystalline npp^+ solar cells which are soldered on top of each other. The stack is sliced perpendicular to the junction and polished. The contacts are on the top and the bottom of the stack and the cell is illuminated from the side wall. The vertical multi-junction solar cell was designed for concentrator systems. This is a construction of mirrors or lenses that focusses the incoming light from a large area onto a relatively small solar cell. The advantage of using a vertical multi-junction structure in a concentrator system is that the voltage increases rather than the current, thus reducing the electrical losses due to internal resistances. In addition, the active area is not reduced by a contact grid. The only loss of area comes from the solder joints, which are relatively small.

A disadvantage of the vertical design of this $c\text{-Si}$ -based solar cell is that photo-generated minority carriers could have an extra diffusion component due to the gradient in the concentration of excess carriers between the illuminated surface and the bottom of the cell as a result of the inhomogeneous generation profile. This effect can explain the relatively low conversion efficiency of 8% (AM0), although that result was ascribed to a non-optimised lay-out of the cell.

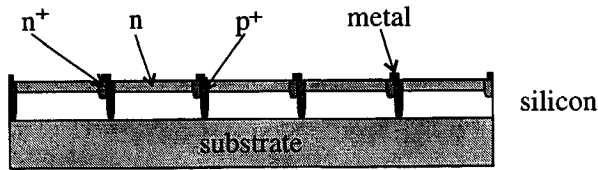


Figure 6.3: Film-silicon solar cells connected in series (after Takato *et al.* [94]).

It is not useful to apply *a*-Si:H solar cells in a concentrator system. The aim of such a system is to reduce the amount of expensive silicon, whereas *a*-Si:H is cheap and suitable for large-area applications. Moreover, the high illumination intensity enhances the Staebler–Wronski effect in *a*-Si:H. Therefore, it is not beneficial to use the TJSC for this purpose.

Another solar cell array was reported in film silicon technology by Takato *et al.* in 1998 [94]. Figure 6.3 shows a schematic lay-out of the cell array. Film silicon solar cells are (poly-)*c*-Si solar cells with a thickness of 20~50 μm , deposited on a ‘non-silicon’ substrate [112]. The reported cell array has a non-conductive substrate (Silicon-on-Insulator wafer) and the Si layer is lightly *p* doped. At the top surface an *n*-type emitter is made by diffusion of phosphorus. The emitter region is contacted by a grid of diffused *n*⁺-type wells and the bulk region is contacted by *p*⁺-type wells. In this specific design, the film thickness is made unusually thin, only 3 μm , such that the *p*⁺-type wells are diffused through the entire layer thickness. Now the *n*⁺-type and the *p*⁺-type wells form an ohmic tunnel/recombination junction and in order to reduce the series resistance, the junction is covered by a metallisation on top of the wells. Although this series connection works quite well, the efficiency is relatively low for a *c*-Si cell: ~6%, which is caused by the small layer thickness.

6.2 Interconnecting *np* junctions

The simplest way to fabricate an array of TJSC’s is by positioning the cells such that the *n* region of one cell touches the *p* region of the adjacent cell in such a way, that a tunnel/recombination junction is obtained. This situation is similar to the *np* junction in conventional tandem solar cells [30]. In fact, a tunnel/recombination junction is a reverse-biased diode which is always in breakdown. In the breakdown region, the *I*-*V* characteristic of such a junction is ohmic rather than rectifying.

We have fabricated arrays of TJSC’s in which the *np* junctions are used to connect adjacent cells (Fig. 6.4). The arrays consist of 1, 2, 5, 10, and 20 cells. The length of each cell is 2.5 mm, the widths of the intrinsic region and each of the doped regions are 1 μm . The layer thickness is 500 nm. Figure 6.5 shows the open-circuit voltage and the fill factor of these arrays. The electrical losses at each

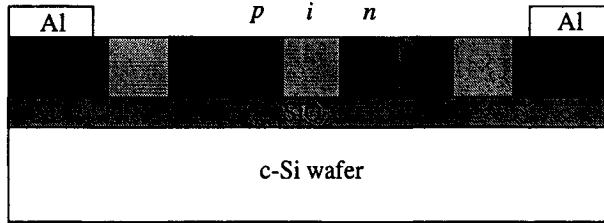


Figure 6.4: Schematic lay-out of an array of TJSC's, where the np junctions form an interconnect.

connection are evident from these figures, as the V_{oc} does not scale linearly with the number of cells. The loss of the open-circuit voltage, V_{loss} , can be calculated in each data point by

$$V_{loss}(n) = \frac{nV_{oc}(1) - V_{oc}(n)}{n - 1}, \quad (6.1)$$

where n is the number of cells. The average of V_{loss} is 0.63 V over the data in Fig. 6.5.a, whereas the V_{oc} of a single cell is 0.75 V. Obviously, the junction operates as a solar cell in the opposite direction. The behaviour of lateral a -Si:H np junctions was studied in a separate experiment. The fabrication process is equal to the process as described in Sec. 2.2 and in App. A.2, using a modified lay-out as shown in Fig. 6.10 (in which $l = 0$). The np diodes are made in a 500 nm thick a -Si:H layer; the length of the cells is 0.5 mm and the distance between the junction and the (planar) contact is 25 μm . Figure 6.6 shows the I - V curve of a single lateral np junction illuminated with a 100 mW/cm^2 halogen light source. This diode has a V_{oc} of 0.65 V, which is close to the observed voltage drop in the cell arrays.

The operation principle of a tunnel/recombination junction is based on non-localised generation-recombination processes. According to the trap-assisted tunnelling model [32] one of the requirements for nonlocal recombination is that the space-charge region of the junction is sufficiently narrow to ensure a high built-in electric field ($>10^7$ V/cm). The ion implanted np junction does not meet this requirement, since the lateral spread of the implanted doping atoms results in compensated doping at the interface between the n region and the p region. Hence, the width of the space-charge region increases considerably. This effect also explains the photovoltaic effect in the a -Si:H np junction in Fig. 6.6. Photovoltaic conversion can only occur in the space-charge region, since the minority carrier diffusion length is negligible. The diode in Fig. 6.6 shows that a relatively large region of compensated doping is present at the interface of a lateral implanted np junction.

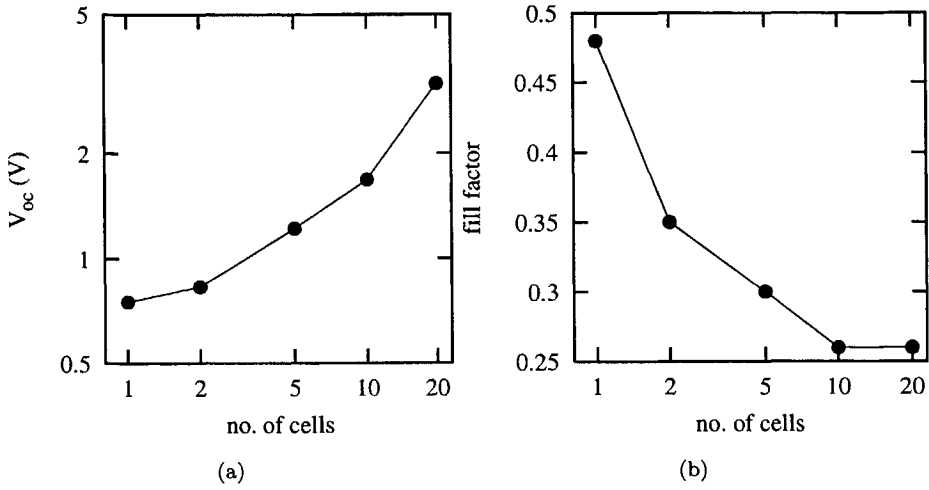


Figure 6.5: Open-circuit voltage and fill factor of several arrays of cells as shown in Fig. 6.4.

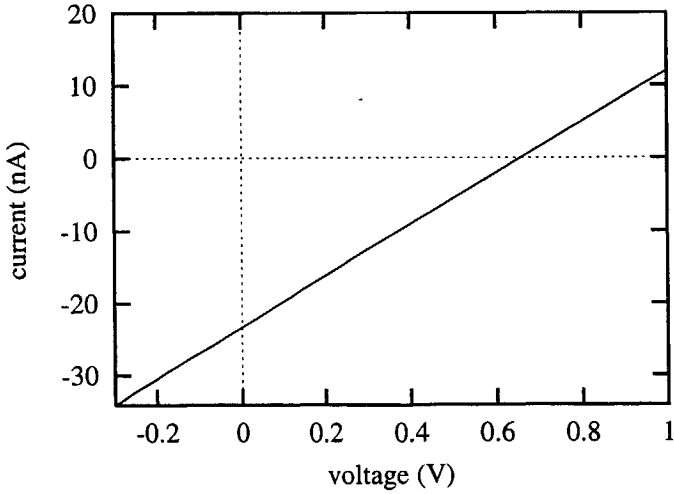


Figure 6.6: $I-V$ curve of an np junction under illumination.

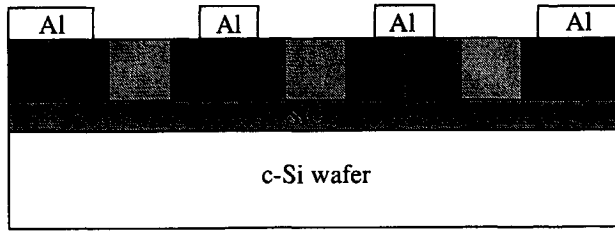


Figure 6.7: Schematic lay-out of an array of TJSC's with metal interconnects.

6.3 Metal interconnects

In order to overcome the electrical losses in the np junctions between adjacent cells, we have fabricated arrays of cells in which the np junctions are short-circuited by a narrow aluminium bar as shown schematically in Fig. 6.7. These bars were made in the same process step as the aluminium contacts. Hence, the fabrication of these arrays does not require additional process steps.

Arrays have been fabricated that consist of 1, 2, 5, 20, and 100 cells. The length of the cells is 2.5 mm, the width of the intrinsic region is $1.0\ \mu\text{m}$ and the width of each of the doped regions is $2\ \mu\text{m}$. The width of the Al bar that covers the np junction is defined as $3.6\ \mu\text{m}$ on the lithographic mask.

The open-circuit voltage, the fill factor, and the efficiency of the best series are plotted in Fig. 6.8. The device with 100 cells in series has a V_{oc} of 66.4 V and at the maximum power point, which is at 47 V, the efficiency is 0.27% (where the entire device area is considered). With this design, a linear relation between the open-circuit voltage and the number of cells is observed. The voltage loss at each connection is 26 mV for the devices up to 20 cells, using Eq. 6.1. The fill factor of the device with 100 cells in series has decreased by 14%. The normalised $I-V$ curves of the cells are shown in Fig. 6.9. The deviation of the curve of the device of 100 cells is remarkable. The voltage loss per connection is 0.11 V, which is much larger than in the devices up to 20 cells. A plausible explanation is contamination during the fabrication process. The larger the area of the device, the larger the probability that dust particles affect the lithographic process or the ion implantations. The increased short-circuit current was reproducible and observed at all wafer positions. We do not have an explanation for this effect.

Note that this cell geometry cannot be used when the solar cell is illuminated through a transparent substrate (Sec. 4.4). In that case, the quasi-intrinsic region underneath the cells are conductive and the generated charge carriers will not be collected. A test array consisting of 100 cells in series was fabricated on a glass wafer, resulting in a V_{oc} of 41 V when illuminated from the top side and 10 V when illuminated through the substrate. The short-circuit current is 64% higher when illuminated through the substrate, however, this difference is small in comparison

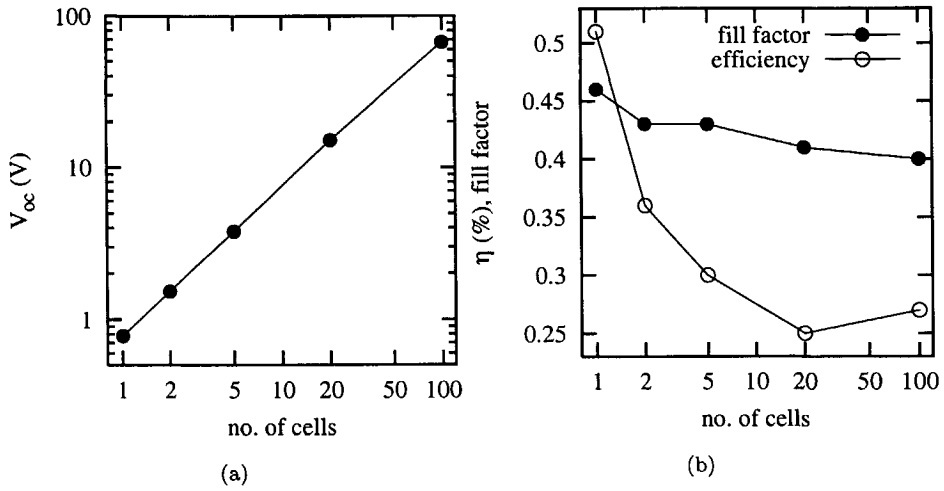


Figure 6.8: Open-circuit voltage, fill factor, and efficiency of arrays of cells as shown in Fig. 6.7. The efficiency is a percentage and is calculated from the entire device area.

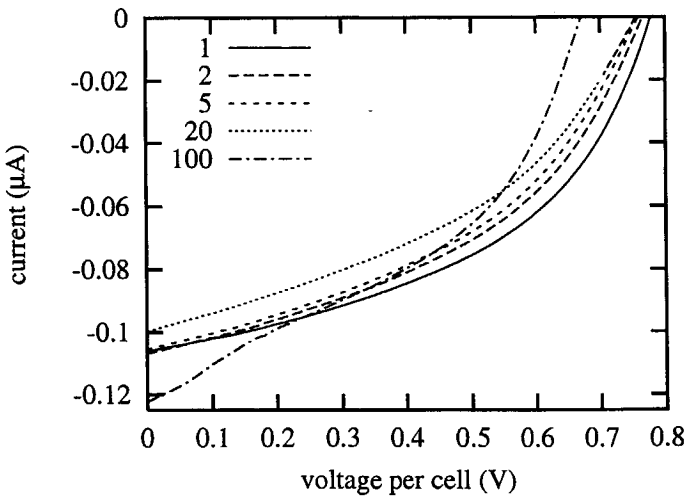


Figure 6.9: I - V curves of arrays with metal interconnects.

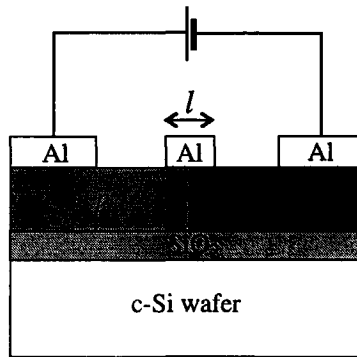


Figure 6.10: Schematical lay-out of test devices to measure the minimum bar width in order to prevent photovoltaic effects in the np junction.

to the results discussed in Sec. 4.4.

The performance of the devices depends strongly on the position of the device on the wafer. The best result of the array of 100 cells is 66.4 V and has been obtained in the centre of the wafer. At the wafer edges, the V_{oc} is 38-45 V. Obviously, the fabrication of the Al bars is a critical process step, in particular the RIE etch. The etch rate in the centre is lower than at the edges of the wafer. Since the etch recipe is not completely isotropic, over-etching leads to smaller dimensions of the metal bars that cover the np junctions. When the metal bar becomes too narrow, it does not completely cover the junction and photovoltaic effects occur as described in the previous section.

Another wafer was fabricated in which the width of the doped regions was $1\ \mu\text{m}$ and the Al bar was $2\ \mu\text{m}$ in width. The best result obtained on this wafer was 65.8 V on an array of 100 cells with a conversion efficiency of 0.40%. The enhanced efficiency is solely caused by the smaller area of the device. However, the fabrication process was more difficult to control, resulting in a larger spread of the array performance over the wafer area.

The minimum bar width required to cover the space-charge region was determined in an additional experiment. Lateral np junctions were fabricated with an Al bar of different widths on top of the junction (Fig. 6.10). The I - V curves of these devices were measured under illumination with a $100\ \text{mW}/\text{cm}^2$ halogen light source. Figure 6.11 shows the extracted V_{oc} as a function of bar width, l . The required bar is much larger than typical widths of the space-charge region of an a -Si:H np junction. This is ascribed to the previously mentioned compensated doping and to light scattering under the Al bar. Figure 6.11 illustrates that the doped regions have to be wider than the lithographic resolution of $0.5\ \mu\text{m}$. For example, when the width of the Al bar is $3\ \mu\text{m}$, the loss of V_{oc} is $\sim 10\%$.

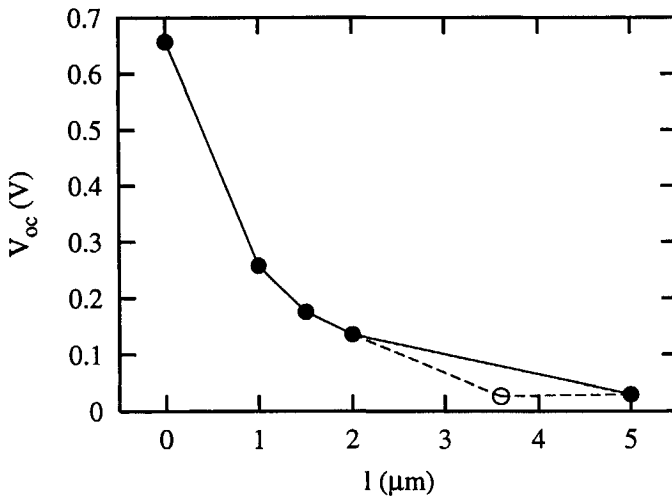


Figure 6.11: V_{oc} of a single np junction with a covering Al bar as in Fig. 6.10. The open circle represents the calculated voltage loss at the junctions in Fig. 6.8.a.

6.4 Conclusions

The TJSC array of 100 cells has an area consumption of only 1.25 mm^2 . However, although this is probably the world's smallest solar cell array, further reduction of the area consumption is limited. These limitations are not only determined by fabrication technology, but also by semiconductor physics. Since the doped regions do not contribute to power conversion, the efficiency will be relatively low. However, these miniature solar cell arrays have potential for applications that require a high voltage and hardly consume power, such as described in Sec. 6.1. For these applications, the number and the length of the cells in the array can be adjusted to optimise the voltage and current at maximum power point for the requirements of the application.



Defect Distribution in a -Si:H *pin* diodes

7.1 Introduction

It is well known that the defect density in a -Si:H depends on the position of the Fermi level during deposition of the material, when the defect states are formed. This dependency is a result of the equilibration of defect states, which is described by the defect-pool model (Sec. 7.2.1). In the intrinsic region of a *pin* diode, the Fermi level depends on the position in the device with respect to the doped regions. Consequently, the defect density is higher near the interfaces than in the bulk of the intrinsic region. At least, it depends on the fabrication history of the diode whether or not defect equilibration leads to a spatial dependence of the defect density. In a conventional layered a -Si:H *pin* diode, the Fermi level in the intrinsic region experiences the presence of the underlying p layer (Sec. 7.2.2). However, the fabrication history of the TJSC is quite different. During deposition of the intrinsic a -Si:H layer, the Fermi energy is essentially constant (ignoring band bending at the interfaces), so the created defect DOS is uniform in space. When the doping atoms are implanted, the Fermi energy in the doped regions is shifted and becomes dependent on the position within the intrinsic region. Here the question arises whether the defect density remains uniform in space, or re-equilibrates according to the change in the Fermi level. In the latter case, the defect density depends on the position, like in conventional *pin* diodes.

Defect states or *traps* are manifested in two ways: they act as trapping centers for free charge, thereby modifying the space charge, and they are recombination centres. Measuring the dark I - V relation is an excellent tool to study the distribution of recombination centres in the diode [42]. This chapter analyses the dark I - V characteristics of conventional a -Si:H *pin* diodes and TJSC's. The relation between the recombination and the dark I - V curve is explained in Sec. 7.2.3. The characteristics of the TJSC are analysed experimentally (Sec. 7.3) and by simula-

tions (Sec. 7.4) and compared to conventional *pin* solar cells. In Sec. 7.5, a model is presented that explains the ideality factor of both types of a -Si:H diodes.

7.2 Theory

7.2.1 The defect-pool model

The disorder in amorphous silicon gives rise to defect states in the band gap and these states play a dominant role in the electronic properties of the material. There is considerable evidence that the formation of defect states is governed by thermodynamic equilibrium reactions during deposition of the material [80, 81]. One of the pioneering publications on this topic is by Bar-Yam *et al.* [2]. They assumed an amorphous ground state, which is a perfect atomic network with well defined energy bands. Dangling bond states have a higher energy, but they can be created by thermodynamic excitations from the ground state. When the temperature of the system is below the temperature of equilibration, T^* , the dangling bonds are frozen.

Stutzmann demonstrated the existence of a universal relation between the Urbach energy (representing the number of weak bonds) and the number of defect states (*i.e.*, dangling bonds) [84]. From this result it was concluded that the main mechanism of defect creation is the conversion of weak bonds into dangling bonds. Simply spoken, during material deposition, which occurs at the temperature T^* , the weak bonds can break and form two dangling bonds. Dangling bonds have a higher energy and this reaction can occur due to thermodynamic fluctuations. After deposition the cooling rate is faster than the time required to modify the thermal equilibrium and the defect states are frozen in. Inherent to the disorder of the network, the dangling bond can take a range of energy levels. When the charge of the defect is taken into account, this leads to energy bands of positive, neutral, and negative charge states, the so-called defect pool. The energetic distribution of the defect pool can be calculated by analyzing the laws of mass action for the chemical reactions involved in the defect formation. Many researchers have worked on the development of a proper model to describe the defect pool [61, 68, 82, 107]. One of the most complete defect-pool models (DPM) was developed by Powell and Deane in 1996 [62], in which the influence of hydrogen reactions is analysed in detail. Important parameters in this model are the Fermi energy, T^* , the disorder (*i.e.*, the slope and density of the valence band tail), and the hydrogen content.

Figure 7.1 shows the energetic distribution of defect states as calculated by the DPM, for three positions of the Fermi level, corresponding to *p*-type, intrinsic, and *n*-type a -Si:H. A very important result of the DPM is that the DOS changes drastically upon doping of the material. *N*-type a -Si:H has a large number of negatively charged states in the lower half of the band gap, whereas *p*-type a -Si:H has a large number of positively charged states in the upper half of the band gap. In addition, the total defect density is much higher in doped a -Si:H than in

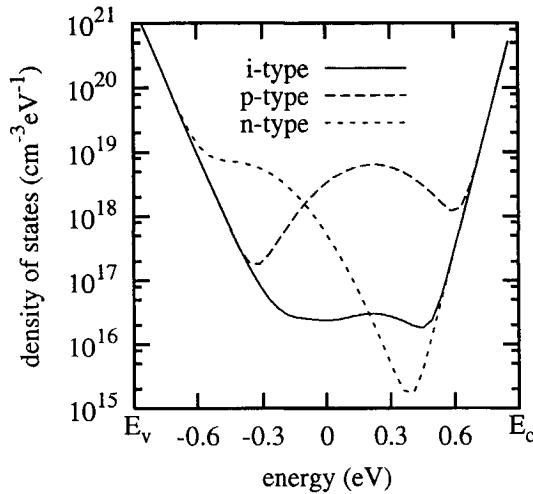


Figure 7.1: Energetic DOS distribution in the band gap of a -Si:H according to the DPM [62]. Functions are plotted for intrinsic ($E_F = 0$ eV), for p -type ($E_F = -0.6$ eV), and for n -type a -Si:H ($E_F = 0.6$ eV). Other important parameters are: $E_g = 1.80$ eV, the characteristic energy of the gaussian pool, $E_{db0} = 0.144$ eV, $E_{corr} = 0.2$ eV, $E_{v0} = 0.056$ eV, $N_{v0} = 2 \times 10^{21}$ cm $^{-3}$ eV $^{-1}$, $T^* = 500$ K, and a hydrogen concentration of 5×10^{21} cm $^{-3}$.

intrinsic material.

7.2.2 Defect distribution in pin diodes

The defect-pool model has large consequences for the spatial distribution of defect states in the intrinsic layer of an a -Si:H pin diode. The early work in this field was done by Branz and Crandall [8], who calculated the defect density as a function of the Fermi level and solved the Poisson equation of a p - i junction, using a position-dependent defect density. The term *defect density* is used to denote the concentration of dangling bonds. The concentration of band-tail states is assumed constant.

In the intrinsic layer, the position of the Fermi level depends on the distance from the p/i interface. In the vicinity of the p layer the Fermi level is below the intrinsic Fermi level. Consequently, the DOS has a ' p type'-like distribution with a relatively high defect density (Fig. 7.1). In the centre of the intrinsic region the Fermi level is near midgap, corresponding to an ' i type'-like DOS, and near the i/n interface, an ' n type'-like distribution is established.

The simulation package ASA is able to solve the Poisson equation for a pin structure having an equilibrated DOS according to the DPM [110]. Figure 7.2 shows the defect density as a function of the position in a pin diode. Near the

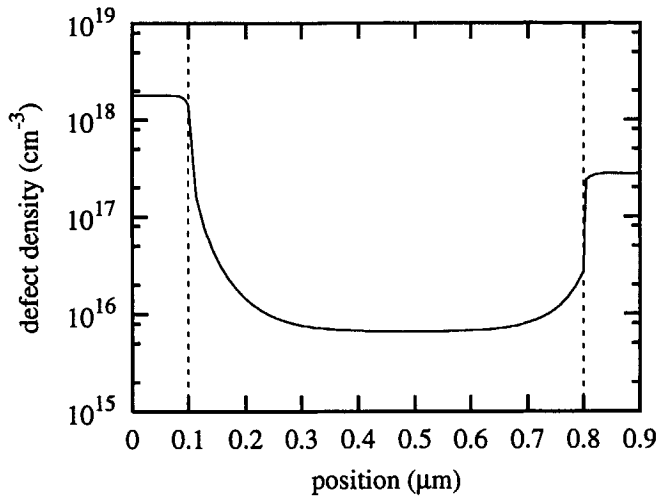


Figure 7.2: Defect density according to the defect pool model [62] for an *a*-Si:H *pin* diode, using the parameters in Table B.2. The vertical line on the left-hand side is the *p/i* interface; on the right-hand side it is the *i/n* interface.

p/i interface, the defect density is more than one order of magnitude higher than in the bulk of the intrinsic region. The defect density has an exponential dependence on the distance between the actual Fermi level and the intrinsic Fermi level. The latter is slightly above midgap, so the defect density is higher near the *p/i* interface than near the *i/n* interface, although the activation energy of the *p* layer is generally higher (here 0.38 eV for the *p* layer and 0.28 eV for the *n* layer).

Near the *p/i* interface the space-charge density is very high due to the high defect density. This is reflected by severe band bending, which is evident from the simulation results shown in Fig. 7.3. For comparison, the band diagrams are shown of *a*-Si:H *pin* diodes with a defect density as in Fig. 7.2 and with a spatially uniform defect density. The defect density is very high in the doped regions; hence, there is virtually no space charge density in these regions. It is evident from the figure that the equilibration of defects result in significant band bending in the *p/i* interface region. Consequently, the Fermi energy is at a higher level in the larger part of the intrinsic region.

7.2.3 Charge transport in *a*-Si:H *pin* diodes

The forward current in *a*-Si:H *pin* diodes has been analysed extensively in literature. Several conduction mechanisms have been proposed, like diffusion through the intrinsic region [11] and tunnelling through the *p/i* interface [50]; at present, however, there is substantial evidence that the forward current is driven by bulk

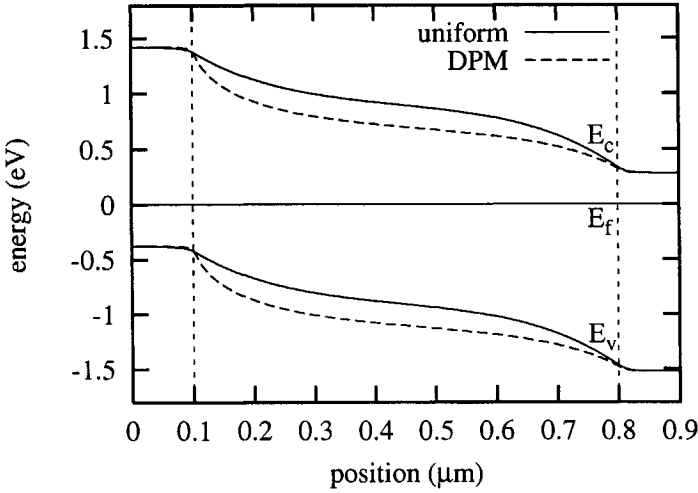


Figure 7.3: Simulated band diagrams in thermal equilibrium of an a -Si:H pin diode using the parameters in Table B.2.

recombination processes in the depletion region of the pin diode [4, 23].

The forward current through an a -Si:H diode is induced by recombination processes. Hence, it can be calculated by integrating the recombination rate at all trap states in the device. Recombination occurs in the depletion region, which is essentially equal to the intrinsic layer of thickness W . Following the zero-Kelvin approximation of Simmons and Taylor [73], the recombination current density is written as

$$J_{rec}(V) = q \int_0^W R_{srh} \left[\int_{E_{fp}(x,V)}^{E_{fn}(x,V)} N(x, E) dE \right] dx, \quad (7.1)$$

where the inner integral is the DOS between the quasi-Fermi levels for holes and electrons.¹ The Shockley-Read-Hall recombination rate per trap level, R_{srh} , is given by [24, 70]

$$R_{srh} = \frac{\sigma_e \sigma_h v_{th} (np - n_i^2)}{\sigma_e (n + n') + \sigma_h (p + p')} \quad (7.2)$$

where v_{th} is the thermal velocity, σ_e and σ_h are the capture rates for electrons and holes, respectively, and n' and p' express the emission rate. The recombination rate has a maximum when $\sigma_e n = \sigma_h p$. However, the spatial dependence of the defect density has also a pronounced effect on the recombination profile. In case

¹For simplicity it is assumed that the quasi-Fermi levels for *free* charge carriers are equal to those for *trapped* charge, which were defined and used according to Simmons and Taylor [73].

of an equilibrated DOS, the product of R_{srh} and the defect density (*i.e.*, the inner integral in Eq. 7.1) results in a peak in the recombination near the *p/i* interface, where the defect density is highest, although $\sigma_e n \neq \sigma_h p$.

The shape of the recombination profile can be verified experimentally by varying the width of the intrinsic region, W . A change of W will change the electric field and the free carrier concentrations in the centre of the intrinsic region. When a uniform defect distribution is assumed, the recombination current depends on W . However, in case of an equilibrated DOS (Fig. 7.2), the recombination peaks near the *p/i* interface, where the band bending is more or less fixed by the high space-charge density. In this case a change in W will not affect the recombination in this part of the junction.

7.3 Results

7.3.1 Procedure

In the fabrication process of the TJSC's which are analysed in this section, the annealing step after ion implantation (Sec. A.2, step (7)) was omitted. After deposition of the contacts, the cells were annealed for 1 hour at 120°C instead of the regular 150°C. This allowed us to study the effect of annealing on the diode characteristics, since during the fabrication of the cells, the temperature does not exceed 120°C. In Sec. 4.2 it was pointed out that the cells with a W of 0.4 μm have overlapping doped regions. Therefore, we will only analyse the larger cells in this section. The current density is obtained by dividing the measured current by $l \times d$ (see Fig. 4.1), where $l = 3$ mm and $d = 500$ nm.

7.3.2 Experimental results

Figure 7.4.a shows the forward I - V curves of the TJSC's as fabricated. The curves exhibit a clear dependence on the width of the intrinsic region. This indicates that in these devices, recombination occurs in the bulk of the intrinsic region rather than at the interfaces. Obviously, the cells are not equilibrated. A series resistance can also give rise to a dependence on the width, however, the I - V curves are strongly rectifying, whereas a series resistance has a linear I - V relation.

Table 7.1 lists the saturation current densities, J_0 , and the ideality factors, m , of the TJSC's before and after annealing. They were obtained by fitting the linear parts of the curves (*i.e.*, $0.25 < V < 0.70$ V) to the equation

$$J(V) \approx J_0 \exp\left(\frac{qV}{mkT}\right). \quad (7.3)$$

The ideality factors of the TJSC's are significantly larger than those of conventional *pin* diodes (Sec. 7.3.3). In Sec. 7.5, the ideality factor is discussed in detail.

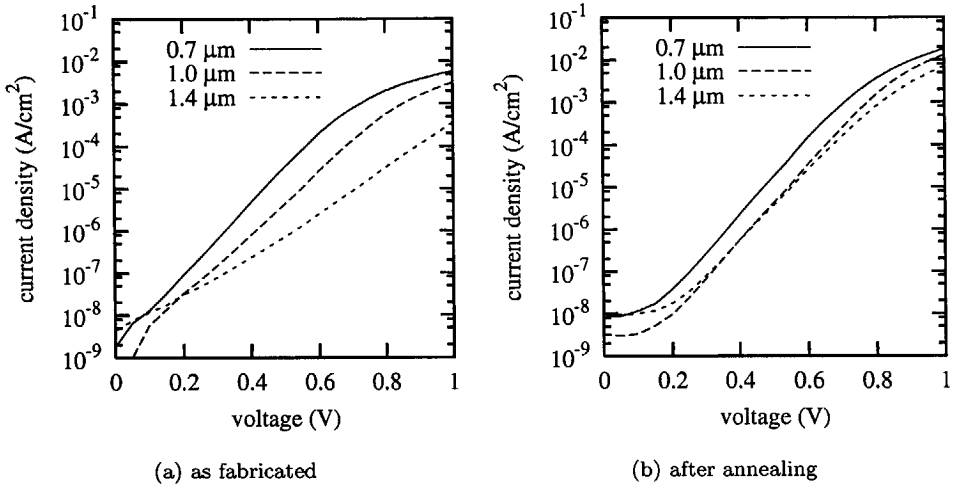


Figure 7.4: Dark forward characteristics of TJSC's with different widths of the intrinsic region, measured (a) as fabricated and (b) after annealing for 1 hour at 193°C.

W (μm)	as fabricated		after annealing	
	J_0 (A/cm^2)	m	J_0 (A/cm^2)	m
0.7	2.8×10^{-9}	2.09	5.8×10^{-10}	1.87
1.0	8.3×10^{-10}	2.26	1.4×10^{-10}	1.87
1.4	2.3×10^{-9}	3.31	2.6×10^{-10}	2.02

Table 7.1: Parameters of the measured dark I - V curves for different widths of the intrinsic region, fitted to Eq. 7.3.

After annealing the TJSC's for one hour at the deposition temperature (193°C), the I - V curves were measured again (Fig. 7.4.b). These curves have a much smaller dependence on the width of the intrinsic region, from which it can be concluded that the defects in the intrinsic region re-equilibrate during the anneal. A similar result was obtained after an anneal for 15 min. at 240°C. The saturation current and the ideality factor have decreased after annealing, so the total recombination is lower.

Annealing has a relatively small effect on the activation of doping atoms. The activation energy of the p -doped region did not change; the activation energy of the n -doped region decreased by 30 meV. We assume that this change can be ignored, since the current in the intrinsic region is limited by holes rather than electrons.

7.3.3 Comparison to conventional solar cells

In Sec. 7.2.3 it was shown that defect equilibration in an a -Si:H diode can be demonstrated by measuring the dark I - V curves of a set of diodes with different W (*i.e.*, different thicknesses of the intrinsic layer). In this section, conventional a -Si:H diodes are analysed by this method. The acronyms '*pin*' and '*nip*' refer to the sequence in which the layers were deposited.

One can imagine that the defect distribution in the intrinsic layer depends on the deposition sequence of the device. Suppose the deposition of a conventional a -Si:H *pin* diode. First the p layer is deposited. The deposition of the intrinsic layer is initiated on top of the p -layer. Here a ' p type'-like DOS is formed in the intrinsic layer, since the underlying p layer forces the Fermi level in the lower part of the band gap. As the intrinsic layer grows thicker, more and more charge of the p layer is compensated, and the Fermi level moves towards midgap. Correspondingly, the defect density decreases and one arrives at an ' i type'-like DOS in the centre of the intrinsic layer. At the i/n interface the situation is complicated. When the n layer is deposited, the Fermi level in the intrinsic layer is shifted in the upper part of the band gap. However, at the moment that the defects were created, the Fermi energy was still at its intrinsic level. It depends on the deposition time and temperature of the n -layer whether or not the DOS in the intrinsic layer equilibrates to the change in the Fermi level. Charged deep-level spectroscopy measurements [55] have indicated that at the time scale required to deposit an n layer, the defect state in the intrinsic layer do not have the opportunity to complete a redistribution upon the new position of the Fermi level [91]. Newly created defects are neutral rather than negatively charged as in an equilibrated ' n type' distribution.

Figure 7.5.a shows the forward characteristics of a set of a -Si:H *pin* diodes. They have i -layer thicknesses of 300, 450, 600, and 750 nm. The area of the silver back contact is 2.5 mm² and outside this area, the n layer was removed by RIE etching in order to prevent current spreading [106] using the etch recipe in

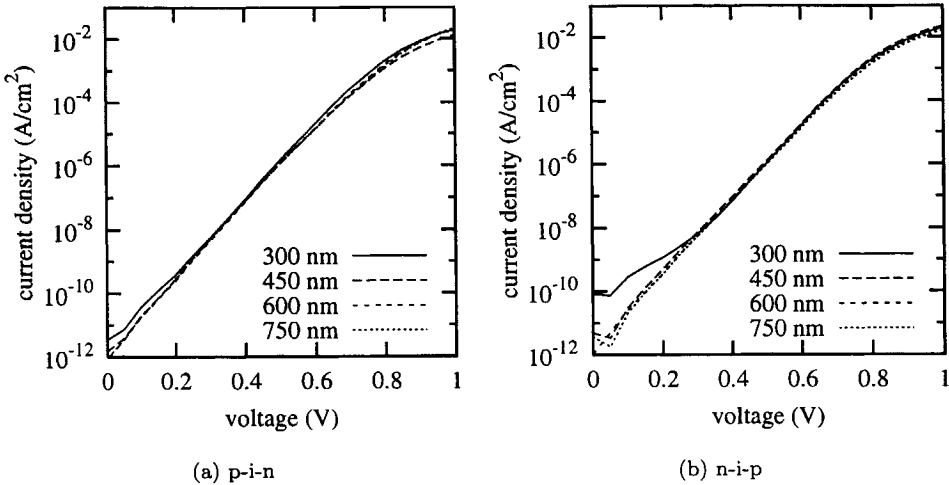


Figure 7.5: Dark forward characteristics of conventional a -Si:H diodes with (a) a pin deposition sequence and (b) an nip sequence. The thickness of the intrinsic layer was varied.

Sec. A.2, step (9b). There is no dependence of the dark current on the thickness of the intrinsic layer.

The dark I - V curve of an equilibrated diode is dominated by the recombination at the p/i interface. Hence, we cannot use this method to study equilibration at the i/n interface. In an nip structure, the p layer is deposited on top of the intrinsic layer, where the DOS is ' i type'-like. The deposition temperature of the p -doped a -SiC:H layer is lower than the temperature of the i -layer (160°C vs. 193°C). Moreover, the p layer is very thin (9 nm). Still the diodes are well equilibrated (see Fig. 7.5.b). The parameters of the diodes are comparable: for the pin structure $J_0 = (1.7 \pm 0.2) \times 10^{12}$ A/cm² and $m = 1.44 \pm 0.02$; for the nip structure $J_0 = (2.1 \pm 0.4) \times 10^{12}$ A/cm² and $m = 1.47 \pm 0.01$. Therefore, it can be concluded that during deposition of the final layer and the subsequent cooling down (inside a vacuum chamber), the defects in the intrinsic layer have sufficient thermal energy to re-equilibrate to the position of the Fermi level which was established by the last layer.

7.4 Numerical analysis

The band diagram and the defect density were shown previously (Figs. 7.2 and 7.3). Those data were simulated in thermal equilibrium, *i.e.*, only the Poisson

<i>parameter</i>	<i>value</i>	<i>parameter</i>	<i>value</i>
E_g	1.80 eV	N_{db}^a	$2 \times 10^{16} \text{ cm}^3$
N_c	$1 \times 10^{20} \text{ cm}^{-3}$	μ_e	$10 \text{ cm}^2/\text{Vs}$
N_v	$5 \times 10^{19} \text{ cm}^{-3}$	μ_h	$3 \text{ cm}^2/\text{Vs}$
N_{c0}, N_{v0}	$1 \times 10^{21} \text{ cm}^{-3} \text{ eV}^{-1}$	$\sigma_{tails}^0, \sigma_{tails}^{+/-}$	$7 \times 10^{-10} \text{ cm}^2/\text{s}$
E_{c0}	0.027 eV	σ_{db}^0	$3 \times 10^{-9} \text{ cm}^2/\text{s}$
E_{v0}	0.045 eV	$\sigma_{db}^{+/-}$	$3 \times 10^{-8} \text{ cm}^2/\text{s}$

Table 7.2: Parameters for simulations in ASA used to simulate the dark *I*-*V* curves.

^aNot used when the DPM is applied.

equation had to be solved. In the following, the recombination profile and the resulting *I*-*V* curves are simulated. The simulations were performed in ASA using the input parameters listed in Table 7.2. For simplicity, the parameters of intrinsic *a*-Si:H were used for the doped regions as well. Figure 7.6 shows the *I*-*V* curves of simulated *pin* diodes with a uniform defect density (*i.e.*, before annealing) and with a nonuniform defect density calculated by the defect pool model [62]. The simulated *I*-*V* curves confirm the experimental results: in case of a uniform defect density, the *I*-*V* curves depend on *W*, whereas in case of an equilibrated DOS, the *I*-*V* curves are independent on *W* at low bias voltages. The ideality factors of the diodes with a uniform defect density correspond to the measured cells before annealing (Table 7.3). However, after equilibration, the ideality factors are still substantially larger than those of conventional *a*-Si:H diodes (1.60 *vs.* 1.44). The difference is caused by the band gap, E_g and the characteristic energy of the valence band tail, E_{v0} of the *p*-layer, since these parameters are different in *p*-type *a*-SiC:H. With a band gap of 1.85 eV (the offset being in the conduction band tail) and an E_{v0} of 0.06 eV, the simulated *I*-*V* curves match the experimental curves very well for bias voltages up to 0.7 V [40]. The dependence of the *I*-*V* curves on these parameters is caused by the fact that near the *p/i* interface, the space-charge density increases due to the increased charge in the valence band tail of the *p* layer.

The experimental TJSC's exhibit a much larger *m* and a higher J_0 after annealing. A plausible explanation is that the defect equilibration is not completely finished. However, increasing the anneal time or the temperature does not lead to substantially smaller ideality factors. Another possible cause of the differences between simulated and experimental results is the two-dimensional design of the TJSC. For example, the longitudinal doping profile, which changes the current path through the diode and leads to variations in the splitting between the quasi-Fermi levels in the vertical direction (Sec. 5.2).

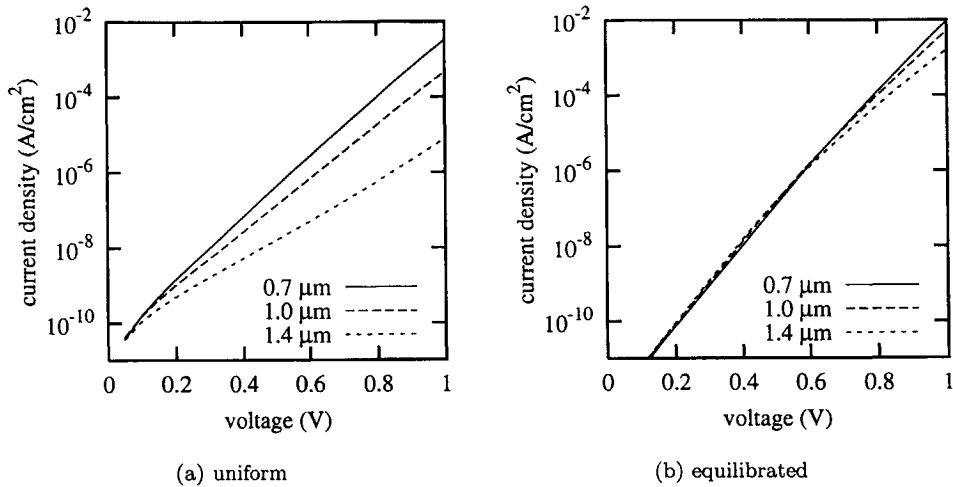


Figure 7.6: Simulated I - V curves of pin diodes with (a) a uniform defect density and (b) equilibrated DOS according to the defect-pool model. The width of the intrinsic region was varied.

W (μm)	uniform		equilibrated	
	J_0 (A/cm^2)	m	J_0 (A/cm^2)	m
0.2	2.20×10^{-11}	1.77	1.70×10^{-12}	1.60
0.4	1.05×10^{-10}	1.89	2.61×10^{-12}	1.60
0.7	2.11×10^{-10}	2.07	3.49×10^{-12}	1.59
1.0	2.28×10^{-10}	2.37	5.11×10^{-12}	1.62
1.4	2.79×10^{-10}	3.29	8.01×10^{-12}	1.69

Table 7.3: Parameters of simulated pin diodes for different widths of the intrinsic region and with uniform and equilibrated defect densities.

7.5 The ideality factor

For crystalline diodes it is generally assumed that recombination in the depletion region results in an ideality factor of 2 and that diffusion through the depletion region results in an ideality factor of 1 [22]. The ideality factor is 1.44 for conventional *a*-Si:H *pin* diodes and 1.9~3.3 for TJSC's over a large voltage range, therefore, the recombination model used to describe crystalline diodes cannot be applied straightforwardly to amorphous silicon diodes.

Van Berkel *et al.* derived an expression for the ideality factor in *a*-Si:H diodes [4]. They solved Eq. 7.1 for the typical distribution of $N(E)$ in *a*-Si:H (neglecting the dependence on the position, x). Only those trap states contribute to the recombination which have an energy in between the quasi-Fermi levels for holes and electrons [73]. When the applied voltage increases, E_{fp} moves further into the valence-band tail and hence, the number of trap states in between the quasi-Fermi levels increases exponentially. This yields an ideality factor of $m^{-1} = (m_0)^{-1} + (m^*)^{-1}$, where m_0 equals 2 and m^* depends on the slope of the valence band tail (which has in general a higher defect density than the conduction band tail). However, numerical simulations show that the recombination at band tail states is negligible in comparison to the recombination at dangling-bond states, since the latter have larger capture rates [79, 103] and are closer to midgap. When the voltage is varied, the number of recombination centres (*i.e.*, the inner integral in Eq. 7.1) does not change that much as van Berkel assumes [4]. For example, when the voltage is increased from 0.2 V to 0.6 V, the number of states in between the quasi-Fermi levels increases only by a factor of six (see Fig. 7.7), whereas the total current increases nearly five orders of magnitude (see Fig. 7.5).

We have used a different approach to explain ideality factors between 1 and 2 [40]. As the inner integral in Eq. 7.1 appears to be almost independent of the bias voltage, the only voltage dependence of the recombination rate is on the electron and hole concentrations in the extended states, which are given by

$$\begin{aligned} n &= n_i \exp\left(\frac{E_{fn} - E_{f0}}{kT}\right), \\ p &= n_i \exp\left(\frac{E_{f0} - E_{fp}}{kT}\right). \end{aligned} \quad (7.4)$$

Under nonequilibrium conditions, the distance between the quasi-Fermi levels equals the applied bias voltage,

$$qV = E_{fn} - E_{fp}. \quad (7.5)$$

Recombination in the depletion region results in an ideality factor of 2 when the following assumptions are made [22]:

1. the quasi-Fermi levels are shifted equally from the equilibrium Fermi level, *i.e.*, $E_{fn} = E_{f0} + qV/2$ and $E_{fp} = E_{f0} - qV/2$;

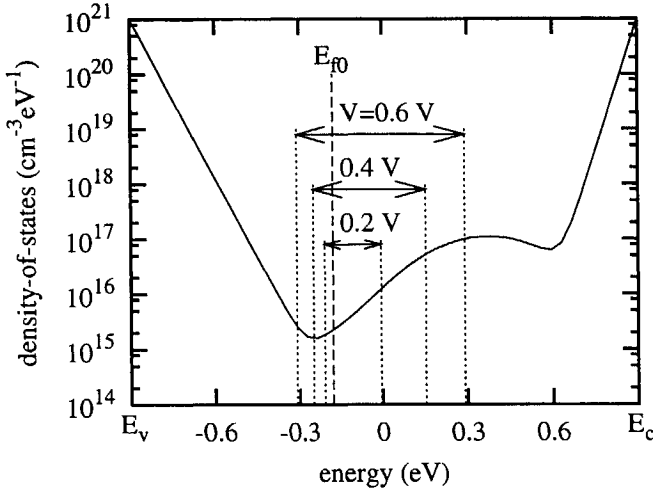


Figure 7.7: Density-of-states, equilibrium Fermi level (E_{f0}) and quasi-Fermi levels at bias voltages of 0.2, 0.4, and 0.6 V at 30 nm from the p/i interface. The DOS was calculated by solving the Poisson equation and the DPM (freeze-in temperature 500 K).

2. the recombination occurs only in that part of the diode where $\sigma_e n = \sigma_h p$;
3. $n, p \gg n_i, n', p'$.

Under these conditions Eq. 7.2 yields

$$R_{srh} \cong \frac{\sigma_e \sigma_h n p}{\sigma_e n + \sigma_h p} \propto \frac{n_i}{2} \exp\left(\frac{qV}{2kT}\right). \quad (7.6)$$

However, in $a\text{-Si:H}$ pin diodes the recombination peaks near the p/i interface, where an applied voltage has only little influence on the band bending. Therefore, when a voltage is applied, the shift of E_{fn} will be larger than of E_{fp} and the first assumption is not correct. This is illustrated in Fig. 7.7, where the DOS and the quasi-Fermi levels at several bias voltages are plotted in an $a\text{-Si:H}$ pin diode at 30 nm from the p/i interface. At this position the recombination profile has a peak when $V = 0.4 \sim 0.5$ V. The shift in E_{fn} with respect to E_{f0} is about 80% of the total distance between the quasi-Fermi levels (note that in Eq. 7.6 it was assumed to be 50%). Due to the high defect density in the p/i interface region, the recombination peaks in a region where $\sigma_h p > \sigma_e n$. Hence, Eq. 7.6 is rewritten as

$$R_{srh} \cong \sigma_e n = \sigma_e n_i \exp\left(\frac{qV}{mkT}\right), \quad (7.7)$$

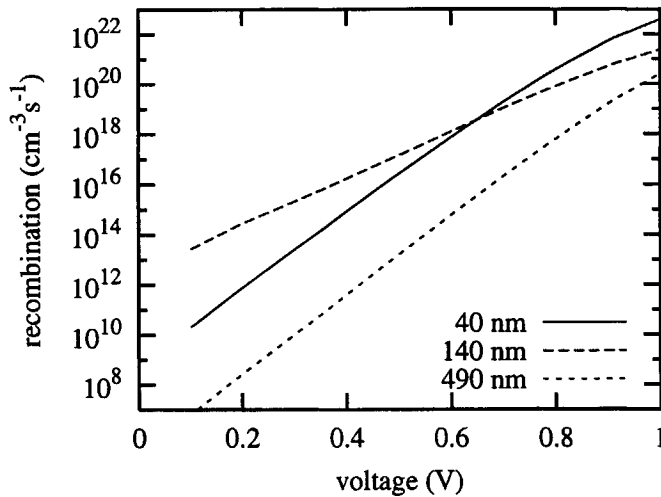
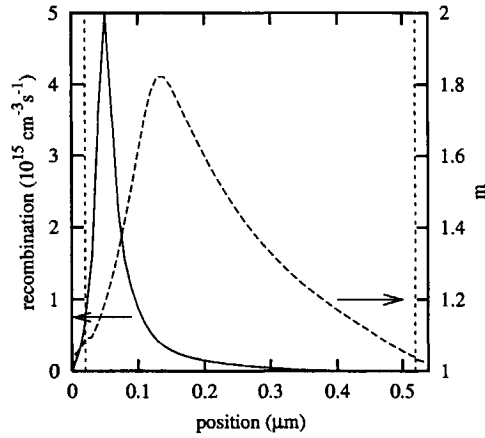


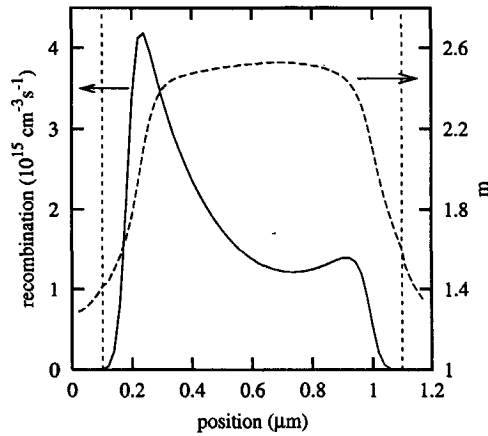
Figure 7.8: Recombination rate as a function of the forward bias voltage in a conventional pin solar cell, simulated with ASA using the DPM. The solid line represents the recombination rate at 40 nm (30 nm from the p/i interface), the long-dashed line the recombination at 140 nm (where $n \approx p$), and the short-dashed line is the recombination at 490 nm (near the i/n interface).

where $m \approx (0.80)^{-1} = 1.25$. This value is a 'local' ideality factor, which can also be calculated numerically. Therefore, the recombination was calculated in ASA at each grid point at several bias voltages. Figure 7.8 shows R_{grh} vs. V at three of those grid points in the intrinsic region, which are located near the p/i interface (at a position of 40 nm, or 30 nm from the p/i interface), at the point where $n \approx p$ (140 nm), and near the i/n interface (at 490 nm). These curves exhibit a well defined exponential part for $V < 0.8$ V. In the exponential parts, the curves were fitted to Eq. 7.7 in order to obtain the 'local' ideality factor as a function of the position in the pin junction (Fig. 7.9.a). At the position of the peak in the recombination profile (at 40 nm), the local ideality factor yields 1.20 and increases to 1.82 at the position where $\sigma_e n \approx \sigma_h p$ (at 140 nm). However, at this position, the defect density and the recombination are much lower, so the contribution to the total current density of the diode is small.

The presented model explains ideality factors between 1 and 2, however, it cannot explain values larger than 2, which were observed in the measurements and simulations of the TJSC's (Table 7.1). In the centre of the $1.0 \mu\text{m}$ wide diode, the quasi-Fermi levels for electrons and holes can both shift from the equilibrium Fermi level, this region is not in the vicinity of a doped layer. Simulations show indeed that the shift of E_{fn} is between 52% and 60% (on average $\sim 56\%$) of the total splitting of the quasi-Fermi levels for bias voltages of 0.2 V and 0.6 V, respectively.



(a) DPM



(b) uniform

Figure 7.9: Recombination (solid line) at 0.4 V and 'local' ideality factor (dashed) as a function of the position in an $a\text{-Si:H}$ pin diode, (a) simulated with the DPM for a conventional pin solar cell and (b) with a uniform defect density, as in a TJSC.

This would yield an ideality factor between 1.8 and 2.

In order to explain values of m larger than 2, we have also studied the influence of the *total* distance between the quasi-Fermi levels. For large W 's, the splitting of the quasi-Fermi levels appeared to be smaller than the applied voltage. Hence, Eq. 7.5 does not apply. Apparently, a substantial fraction of the holes injected from the *p*-doped region recombines in the left-hand side of the intrinsic region and similarly, electrons injected from the *n*-doped region recombine in the right-hand side, which is reflected by the local maxima in the recombination profile (Fig. 7.9.b). In the centre of the intrinsic region, the distance between E_{fn} and E_{fp} varies from $0.62 \times qV$ at a voltage of 0.2 V to $0.69 \times qV$ at 0.6 V (on average ~ 0.65). Thus, replacing the factor qV in Eq. 7.7 by $0.65 \times qV$ results in $m \approx (0.65 \times 0.56)^{-1} = 2.7$. At a distance of 100 nm from the *p/i* interface the relative shift of E_{fn} is larger ($\sim 70\%$ of the total splitting). Here, the calculation gives an m of 1.8. These values are consistent with the simulated profile of the 'local' ideality factor (Fig. 7.9.b). It is difficult to derive an analytical expression for the ideality factor of the entire diode in terms of the 'local' ideality factor, since the total current is found by integration of the recombination in the device (see Eq. 7.1). The solution requires an expression for $J_0(x)$ (the 'local' current density) as well.

7.6 Summary and conclusions

We have examined the recombination profile in *a*-Si:H *pin* diodes in general and in particular in the TJSC. The recombination was studied by analyzing the forward current-voltage characteristics, which are proportional to the total recombination in the device. By varying the width of the intrinsic region, the recombination profile changes in case of a spatially uniform defect distribution. This is the case for unannealed TJSC's. However, when the devices are annealed, the current has a much smaller dependence on the width of the intrinsic region. This indicates that most of the recombination occurs in a narrow region near the *p/i* interface. In this case, the recombination and the current density have a much smaller dependence on the width of the intrinsic region than before annealing. This dependence is completely absent in conventional *a*-Si:H *pin* and *nip* diodes.

We found that two effects are responsible for ideality factors unequal to the theoretically predicted value of 2:

1. The shift in the quasi-Fermi level for holes is smaller than the shift in the electron level, resulting in ideality factors between 1 and 2;
2. The splitting of the quasi-Fermi levels is smaller than the applied voltage, resulting in ideality factors larger than 2.

The first effect occurs in equilibrated *a*-Si:H *pin* and *nip* diodes, in which the recombination peaks in a narrow region near the *p/i* interface where the band

bending is fixed by a high space-charge density. The second effect occurs when the recombination is spread out over a wide region, like in unannealed TJSC's, which have a uniform defect density and a relatively large intrinsic region.



Chapter VIII

Conclusions

The concept of fabricating a thin-film solar cell with a transverse junction has been realised in amorphous silicon. A fabrication process has been developed, which is completely compatible to standard manufacturing of integrated circuits. The fabricated transverse solar cells have an open-circuit voltage of ~ 0.80 V and fill factors of $0.45\sim 0.50$. The short-circuit currents are relatively low, resulting in conversion efficiencies of $2\sim 3\%$, taking only the active area (*i.e.*, the area of the intrinsic region) into account. The performance of the cell has a strong dependence on the geometry. The highest efficiency is obtained when the width of the intrinsic region is ~ 0.7 μm . The following points have to be taken into account when interpreting these results

- The incoupling of light is relatively poor in the characterised cells. The optical system can be optimised, *e.g.*, by applying an anti-reflection coating and a back reflector. Only 40% of the AM1.5 spectrum is absorbed in the active layer of the TJSC, whereas in conventional *a*-Si:H solar cells, the internal quantum efficiency is 80–90%.
- The areas of the doped regions have not been taken into account. It depends on the fabrication technology (*i.e.*, the resolution of the lithographic patterning) what sizes of the doped regions can be obtained. A simple guess is that the doped regions have the same size as the intrinsic region; in that case the active area is one-third of the total area in case of straight junctions, or one-half when an interdigitated finger pattern is used.
- It is difficult to estimate the exact width of the intrinsic region. The values used in this thesis are based on the sizes as they were defined on the lithographic masks. However, the actual projected size depends on the process parameters and has a (line width) inaccuracy of approximately 100 nm.

In the best-case scenario, a better light incoupling increases the efficiency with a factor of two, roughly, and when the area of the doped regions is taken into account,

the efficiency reduces with a factor of two. Thus, the resulting efficiency will be 2~3%. Evidently, an a -Si:H TJSC cannot compete with conventional solar cells when comparing the device characteristics. Moreover, the fabrication technology is much more complicated (*i.e.*, much more expensive) than of conventional solar cells. Especially the optical lithography and the ion implantations are process steps which are difficult to scale up to large areas.

The fill factor is not determined by the aforementioned technological issues, however, the measured values are lower than in conventional a -Si:H solar cells (~ 0.50 *vs.* ~ 0.70). The fill factor is a good measure of the quality of a solar cell and it is unlikely that the fill factor is improved by a better light incoupling or by a different fabrication technology. The low fill factor is caused by the poor carrier collection of the device. A fundamental difference with conventional a -Si:H solar cells is that in the latter, the holes are generated near the p/i interface. Hence, the holes are collected earlier than in the TJSC, where they have to pass on average half the intrinsic region. The lateral straggle of the ion implanted doping atoms results in more recombination in the interface regions and decreases the effective area of the solar cell. Another effect that reduces the fill factor is the significant vertical component of the electric field. Under illumination, more positive charge is generated in the top of the cell than in the bottom. Hence, the generated charge carriers do not travel the shortest distance towards the doped regions, but they follow a curved trajectory.

Obviously, this solar cell is not suitable for power-generation applications. However, there are various applications where a small or even miniature solar cell is useful and where the efficiency is of minor importance. Some examples were discussed in this thesis and they all have in common that they are stand-alone applications, *e.g.*, pocket calculators, smart cards, and disposable electronics. When a high voltage is required, *e.g.*, in sensor and actuator systems, the TJSC is even more interesting, because series connections are easily achieved on small areas. Furthermore, the TJSC is compatible with the manufacturing of integrated circuits, so a TJSC could very well supply the power for a microchip on a single piece of silicon wafer. Using the TJSC as a photodetector is another application where the efficiency is less important. Here the main requirements are that the device is sufficiently small, produces a measurable signal under reverse bias, and has a relatively flat spectral response. The spectral response of the cell can be improved by optimizing the optical system and by passivating the defect states at the surface of the amorphous silicon layer.

Last but not least, the research on the TJSC has been useful for a theoretical study of defect equilibration in a -Si:H *pin* diodes. This research has resulted in a model that explains the origin of the ideality factor and mainly discusses the consequences for conventional a -Si:H solar cells. The TJSC has been very useful as a characterisation tool in order to understand the relation between the defect distribution and the dark current-voltage characteristics of a -Si:H diodes.

———— Appendix A ————

Flow Charts

A.1 General remarks

This appendix contains the most recent flow charts for the fabrication of TJSC's in the DIMES cleanroom facilities. For processing on glass substrates, the flow chart was adapted (Sect. A.3).

The optical lithography consists of three main process steps, which in turn can be divided in several substeps. The parameters and specifications of the lithographic process are listed in Table A.1. The coating and the development processes have fixed parameters. The only variable in the lithographic process is the exposure dose of the wafer stepper, which depends on the reflectivity of the substrate and the desired angle of the photoresist profile. After development, the lithographic pattern was checked under a microscope for the linewidth and the overlay accuracy.

A.2 Crystalline wafer substrates

1. Substrate

n-type Wacker 100 mm test wafers, thickness 0.5 mm; $2-5 \Omega^{-1}\text{cm}^{-1}$, dopant phosphorus.

2. Alignment marks (Zero layer)

- (a) Lithography mask COMURK; Exposure dose 105 mJ/cm^2 .
- (b) RIE etch Sigma Trikon etcher.
- (c) Removal photoresist in acetone at 40°C .
- (d) Cleaning 100% HNO_3 10 min. and 65 % fuming HNO_3 (110°C) 10 min.
- (e) Rinse & Dry.

<i>coating</i>	priming	HMDS 5 min.
	spinning	SPR3012 photoresist thickness 1.4 μm .
	prebake	1 min. 95°C
<i>exposure</i>	ASML PAS5000/50 wafer stepper [1] (<i>i</i> -line, $\lambda=365$ nm)	resolution 0.5 μm . accuracy <125 nm. variable energy
<i>development</i>	postbake	1 min. 95°C
	spray puddle	MF322 developer 45 s.
	rinse & dry	
	postbake	1 min. 100°C

Table A.1: Process parameters and specifications of the lithographic process.

3. Oxidation

Thermal oxidation in a Tempress horizontal 4" furnace at atmospheric pressure.

Temperature: 1100°C

Flows : O₂ 2.25 slm

: H₂ 3.85 slm

Time : 38.5 min.

Thickness : ~550 nm

4. α -Si:H Deposition

PECVD Deposition of intrinsic α -Si:H in the multi-chamber AMOR-system.

Substrate temp.: 193°C

Flow : SiH₄ 40 sccm

Pressure : 0.70 mbar

Power : 2.4 W

Dep. rate : ~2.2 Å/s

5. Phosphorus implantation

(a) Lithography mask IN; Exposure dose 105 mJ/cm².

(b) Ion Implantation: P⁺ 110 keV 5·10¹⁵ cm⁻².

(c) Ion Implantation: P⁺ 25 keV 1.5·10¹⁵ cm⁻².

(d) Removal photoresist in Tepla O₂-plasma stripper at 1000 W with end-point detection.

(e) Cleaning 100% HNO₃ 10 min.

(f) Rinse & Dry.

6. Boron implantation

- (a) Lithography mask IP; Exposure dose 105 mJ/cm².
- (b) Ion Implantation: B⁺ 40 keV 5·10¹⁵ cm⁻².
- (c) Ion Implantation: B⁺ 15 keV 1.5·10¹⁵ cm⁻².

Repeat steps (5d)–(5f)

7. Annealing

195°C for 1 h in air. This process step has been altered or omitted in some experiments described in Ch. 7.

8. Metallisation

- (a) Removal native oxides in 0.55% HF 3 min.
- (b) Rinse & Dry.
- (c) E-beam evaporation of 300 nm Al with Leybold L560.
- (d) Lithography mask IC; Exposure dose 120 mJ/cm².
- (e) RIE etch in Alcatel GIR300 etcher.

Temperature: 50°C

Flows : BF₃ 3.5 sccm

: Cl₂ 3.5 sccm

: N₂ 122 sccm

Pressure : 0.03 mbar

Power : 40 W

Visual end-point detection when structures are opened at wafer edge.

- (f) RIE passivation in Alcatel GIR300 etcher.

Temperature: 50°C

Flows : SF₆ 60 sccm

: N₂ 122 sccm

Pressure : 0.03 mbar

Power : 40 W

Time : 1 min.

(This step was omitted in the experiments of Sect. 6.3.)

- (g) Wet etch until all structures are opened. The etchant contains 65% H₃PO₄, 9% HNO₃, and 14% CH₃COOH. (This step was omitted in the experiments of Sect. 6.3.)
- (h) Rinse & Dry.
- (i) Removal photoresist in acetone at 40°C.
- (j) Cleaning 100% HNO₃ 10 min.
- (k) Rinse & Dry.

9. Isolation (Mesa etch)

- (a) Lithography mask MESA; Exposure dose 105 mJ/cm^2 .
- (b) RIE-etch in Alcatel GIR300 etcher.
 - Temperature: room temperature
 - Flows : SF_6 45 sccm
 - : He 70 sccm
 - Pressure : 0.09 mbar
 - Power : 50 W
 - Etch Rate : $\sim 43 \text{ \AA/s}$

Repeat steps (8i)–(8k)

- 10. **Alloying (Al/Si contact anneal)**
 130°C for 1 h in air.

A.3 Glass substrates

1. Substrate

Corning 7740 100 mm glass wafer, thickness 0.5 mm.

2. Alignment marks (Zero layer)

- (a) E-beam evaporation of 300 nm Al.
- (b) Lithography mask COMURK; Exposure dose 120 mJ/cm^2 .
- (c) Wet etch and cleaning (Sect. A.2, step (8g)–(8k)). Time: 50 s ($\sim 120 \text{ nm}$).
- (d) Lithography with open reticle; Exposure dose 120 mJ/cm^2 . The photoresist residue at the wafer edge was *not* removed.
- (e) Wet etch until window opened and cleaning (Sect. A.2, step (8g)–(8k)).

3. a-Si:H Deposition

See Sect. A.2, step (4).

4. Isolation (Mesa etch) See Sect. A.2, steps (9a)–(9b).

- (a) E-beam evaporation of 50 nm Al (to close transparent area of wafer). Alignment marks are covered by shadow mask.
- (b) Lift-off Al (of step (4a)) in acetone at room temperature in ultrasonic bath.
- (c) Cleaning 100% HNO_3 10 min.
- (d) Rinse & Dry.

5. Implantations

Process as described in Sect. A.2, steps (5)–(6). The beam current is limited to $50 \mu\text{A}$, in order to prevent excessive heating, since the glass substrate has a low heat conductivity.

6. Annealing

See Sect. A.2, step (7).

7. Metallisation

See Sect. A.2, step (8). The native oxide removal was done for less than 30 s to prevent deterioration of the alignment marks in Al. The wafer edge (including alignment marks) are covered with photoresist during etching. The additional Al layer (step (4a)) is removed instantaneously.

8. Alloying (Al/Si contact anneal)

See Sect. A.2, step (10).



———— Appendix B ————

Two-Dimensional Device Simulations

B.1 Introduction

In this thesis, several simulations of TJSC's were presented. Device simulations are used to visualise the internal parameters, like the band diagram, the electric field, and the recombination. Furthermore, the dependence of the external parameters on the geometry of the solar cell can be studied.

The one-dimensional device simulator ASA has been developed for simulations of amorphous silicon solar cells [106, 110]. For simulations of the TJSC a two-dimensional device simulator is required. Two-dimensional device simulators are commercially available [33, 72, 98], however, they are designed for crystalline semiconductors and have limited ability to model the quasi-continuous defect DOS in *a*-Si:H. Two commercial device simulators, ATLAS [71] and MEDICI [99], were investigated for their suitability to model the TJSC. The program ATLAS is user-friendly, however, it contains several bugs in the routines that evaluate the trap statements. Therefore, MEDICI was used in this thesis. This appendix investigates MEDICI for its suitability to model amorphous silicon solar cells.

B.2 Comparison of ASA and Medici

The heart of a device simulator is a routine that solves the Poisson equation and the continuity equations for electrons and holes [106, 110]. The Poisson equation is used to calculate the space-charge density and the continuity equations are used to calculate the concentrations of electrons and holes in the valence and the conduction band, respectively. For amorphous and crystalline semiconductors, these equations are the same. However, for the description of the defect states in the band gap, additional models are required. The defect states in amorphous silicon play a twofold role as trapping centres, which influence the space-charge

<i>description</i>	ASA	MEDICI
dimensionality	1	2
optical models	imported profile Lambert-Beer [106] multi-layer optics ^a [95]	imported profile ray-tracing
defect discretisation	unlimited	max. 50 levels ^b
occupation statistics of defects	Fermi-Dirac (band tails) Sah-Shockley [65] (dangling bonds)	Fermi-Dirac
defect models	exponential band tails gaussian dangling bonds defect-pool models ^d	analytical expressions ^c
doping level	from activation energy input parameter	input parameter

^a*i.e.*, GENPRO1.

^bMax. 20 levels in obsolete versions (before version 1999.4.0).

^cExample given in Fig. B.4.

^dDescribed by Refs. [61, 62, 67]

Table B.1: Comparison of device simulators ASA and MEDICI.

density, and as recombination centres. When α -Si:H devices are simulated, the description of defect states have to be assessed both for charge trapping and for recombination.

The main differences between ASA and MEDICI are listed in Table B.1. Several optical models are implemented in ASA to calculate the generation rate as a function of the position in the device. The ray-tracing analysis in MEDICI is less suitable for thin-film optics, therefore, the generation profiles were calculated with one of the models in ASA and imported in MEDICI. The most important differences are in the description of the defect states as trap levels and as recombination centers, *i.e.*,

- a. In MEDICI, the defect DOS is discretised into a maximum of 50 energy levels; in ASA the discretisation is unlimited and can be optimised for each of the band tails and the dangling-bond states separately;
 - b. In ASA, the dangling-bond states are modelled as amphoteric states, *i.e.*, they are both a donor state (the transition from the empty D^+ to the singly occupied D^0 state) and an acceptor state (the transition from the D^0 to the doubly occupied D^- state). In MEDICI, defects are either empty or singly occupied.
- ad b. The conventional Fermi-Dirac occupation statistics do not apply for am-

photic levels. For example, one can imagine that the D^0/D^- transition can be made only when the D^0 state is filled. Hence, the three occupation levels are correlated. Sah and Shockley described the occupation statistics of a three-level state in the band gap of a semiconductor [65]. These statistics are implemented in ASA [106]. The recombination rate according to the Shockley–Read–Hall statistics [24, 70], is also adapted, since it depends on the occupancy of the defect. In MEDICI, the traps are described as two-level states, using the conventional Fermi–Dirac distribution and Shockley–Read–Hall recombination. However, it is possible to express an amphoteric state as two decoupled states, one acceptor state and one donor state [25]. In order to account for the degeneracy of an amphoteric state, the energy levels of the D^+/D^0 and the D^0/D^- are shifted,

$$\begin{aligned} E_{dec}^{+/0} &= E_{amph}^{+/0} - kT \ln 2 \\ E_{dec}^{0/-} &= E_{amph}^{0/-} + kT \ln 2 \end{aligned} \quad (\text{B.1})$$

i.e., the correlation energy is increased by $2kT \ln 2$. The errors of the decoupled approach have been analysed in several ways [25, 89, 106]. They all conclude that the error in the occupation level is negligible and that the error in the recombination rate is insignificant as long as both quasi-Fermi energies are not closer than kT to the energy of the defect state [89] (*e.g.*, less than 10% when $\sigma_{db}^{+,-}/\sigma_{db}^0=10$ [106]). Furthermore, the decoupled approach requires that the correlation energy, $E_{corr} \gg kT$ [25]. This condition is met for $E_{corr}=0.2$ eV. The capture rates can be adjusted to obtain an acceptable recombination rate.

B.3 The accuracy of Medici

B.3.1 Discretisation error

The quasi-continuous DOS in the band gap is discretised into a number of energy levels with a specific concentration. In MEDICI these levels are distributed equidistantly over the band gap. The error caused by the discretisation induces inaccuracies in the occupation of the trap levels and in the recombination. This section considers the error in the occupancy only, although the recombination is also affected.

The error in the discretisation into n levels is defined as

$$\Delta = \frac{\sum_{i=1}^n f_{fd}(E_i)N(E_i)}{\lim_{n' \rightarrow \infty} \sum_{i=1}^{n'} f_{fd}(E_i)N(E_i)}, \quad (\text{B.2})$$

where $N(E)$ describes the valence band tails and conduction band tails, and the (decoupled) dangling bond states, using the parameters in Table B.2. Equation B.2 was calculated analytically for the valence and conduction band tails and the (decoupled) dangling bonds. Figure B.1 shows the discretisation error of the valence

<i>parameter</i>	<i>p-layer</i>	<i>i-layer</i>	<i>n-layer</i>
thickness (μm)	0.10	0.50	0.10
E_{act} (eV)	0.40	0.90	0.30
E_g (eV)	1.80		
N_c (cm^{-3})	8×10^{20}		
N_v (cm^{-3})	4×10^{20}		
μ_e ($\text{cm}^2/\text{V s}$)	10		
μ_h ($\text{cm}^2/\text{V s}$)	3		
N_{c0} ($\text{cm}^{-3}\text{eV}^{-1}$)	1×10^{21}		
N_{v0} ($\text{cm}^{-3}\text{eV}^{-1}$)	1×10^{21}		
E_{c0} (eV)	0.036	0.027	0.048
E_{v0} (eV)	0.060	0.045	0.080
N_{db} (cm^{-3})	1×10^{18}	1×10^{16}	1×10^{18}
E_{db0} (eV)	0.144		
E_{corr} (eV)	0.20		
$\sigma_{\text{tail}}^0, \sigma_{\text{tail}}^{+,-}$ (cm^3s^{-1})	7×10^{-10}		
σ_{db}^0 (cm^3s^{-1})	3×10^{-9}		
$\sigma_{db}^{+,-}$ (cm^3s^{-1})	3×10^{-8}		

Table B.2: Simulation parameters used for comparison of ASA and MEDICI.

band tail when E_f is equal to E_{act} in the *p* layer, for the conduction band tail when E_f is equal to E_{act} in the *n* layer, and for the dangling bond states when E_f is at midgap. At these positions of the Fermi level, the error is maximal for each type of trap state, since the gradient in the Fermi-Dirac distribution function is largest at E_f . The error in the trapped-charge density is highest in the conduction-band tail, because it is the steepest part of the defect DOS; therefore, it requires a finer discretisation. In MEDICI the energy levels are uniformly distributed over the energy gap, hence, for a number of 50 levels, it means that both band tails have 16 discretisation levels and the dangling bond states ~ 20 (note that the band tails and dangling bonds have overlapping energy ranges). From Fig. B.1 it follows that the error in the trapped-charge density is at most 10% in the conduction band tail and less than 1% in the valence band tail and the dangling bond states.

B.3.2 Comparison of band diagrams

The equilibrium band diagrams in ASA and MEDICI are compared in Figure B.2. For this comparison, a one-dimensional *pin* structure was simulated both in ASA and in MEDICI using the parameters are listed in Table B.2. The band diagrams are nearly overlapping in the larger part of the *pin* structure, except in the doped regions, where the Fermi level is in one of the band tails. This difference is due to the discretisation error in MEDICI. The trapped-charge density is lower in MEDICI

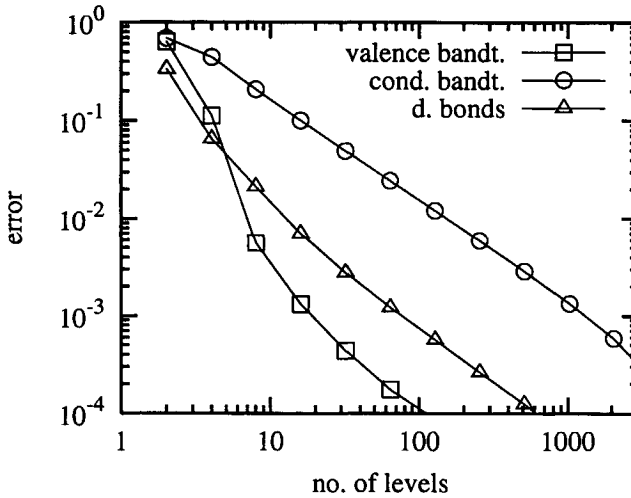


Figure B.1: Error in trapped-charge density due to discretisation of the valence band tail with $E_f = E_{\text{act}}$ of the p layer, the conduction band tail with $E_f = E_{\text{act}}$ of the n layer, and the dangling bond states with E_f at midgap, using the decoupled approach. The material parameters of intrinsic a -Si:H were used.

than in ASA, resulting in depletion of the doped regions.

B.3.3 Nonequilibrium conditions

The dark I - V curves (Fig. B.3.a) in ASA and MEDICI have the same ideality factors, however, the saturation current is higher in the MEDICI simulation. The ideality factor is a measure of the shape of the recombination profile (Sect. 7.5) and these profiles have indeed a similar shape (Fig. B.3.b). Obviously, the recombination at decoupled dangling bond states (MEDICI) is higher than at amphoteric states (ASA). The enhanced recombination also results in a smaller I_{sc} , V_{oc} , and fill factor (Fig. B.3.c). Note that I_{sc} and V_{oc} are related via the ideality factor [40]. Besides, the depletion extends into the n layer, resulting in a higher hole concentration and hence, more recombination in the n layer (Fig. B.3.d).

In order to account for the different recombination rates at amphoteric and decoupled trap states, the capture rates used in MEDICI were optimised to fit the I - V curve under illumination to the simulated curve in ASA, using an inverse modelling routine [59]. An excellent fit is obtained with $\sigma_{db}^0 = 6.57 \times 10^{-10} \text{ cm}^3\text{s}^{-1}$, $\sigma_{db}^{+,-} = 7.96 \times 10^{-10} \text{ cm}^3\text{s}^{-1}$, and $\sigma_{tail}^{+,0,-} = 1.18 \times 10^{-10} \text{ cm}^3\text{s}^{-1}$. However, the recombination profiles do not match under these conditions. An attempt to fit the recombination profiles at I_{sc} by optimizing the capture rates did not lead to satisfying results. Apparently, the error in the space-charge density leads to

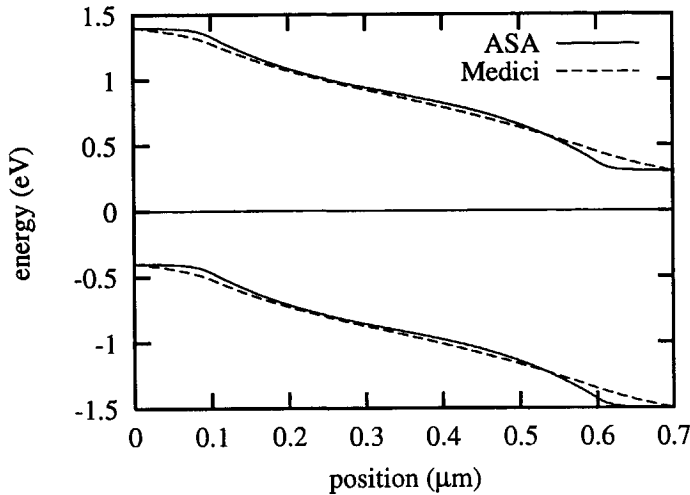


Figure B.2: Comparison of band diagrams in thermal equilibrium simulated in ASA and in MEDICI.

different recombination profiles and the space-charge density does not depend on the capture rates.

B.4 Example input of Medici

Figure B.4 shows an example of the typical input statements to describe the typical exponential band tails and gaussian dangling bonds of α -Si:H in the device simulator MEDICI.

The parameters in the trap statements are defined as follows: @eg: band gap (eV), @ncb, @nvb: DOS at conduction and valence band edges ($\text{cm}^{-3}\text{eV}^{-1}$), @ecb, @evb: characteristic energy of band tails (eV), @ndb: dangling bond concentration (cm^{-3}), @edb: characteristic energy of gaussian states (eV), @crtail, @crdbn, @crdbc: capture rates of band tail states, neutral and charged dangling bonds, @off1, @off2: peak positions of dangling bond states (see Eq. B.2), and @fener: energy (internal parameter in eV). Note that Shockley-Read-Hall recombination is implemented in the trap statement, so additionally defining the SRH model is ambiguous.

When trap statements are defined, MEDICI often encounters convergence problems when the initial solution is calculated. Therefore, the Poisson equation is solved first (carriers=0), and this solution is used as an initial guess for the continuity equations (carriers=2). Convergence problems can also occur in the first solve statement under illumination. Therefore, the generation rate is ramped up in a loop (see Ref. [106]). For additional explanation of the statements, we refer to the users manual [99].

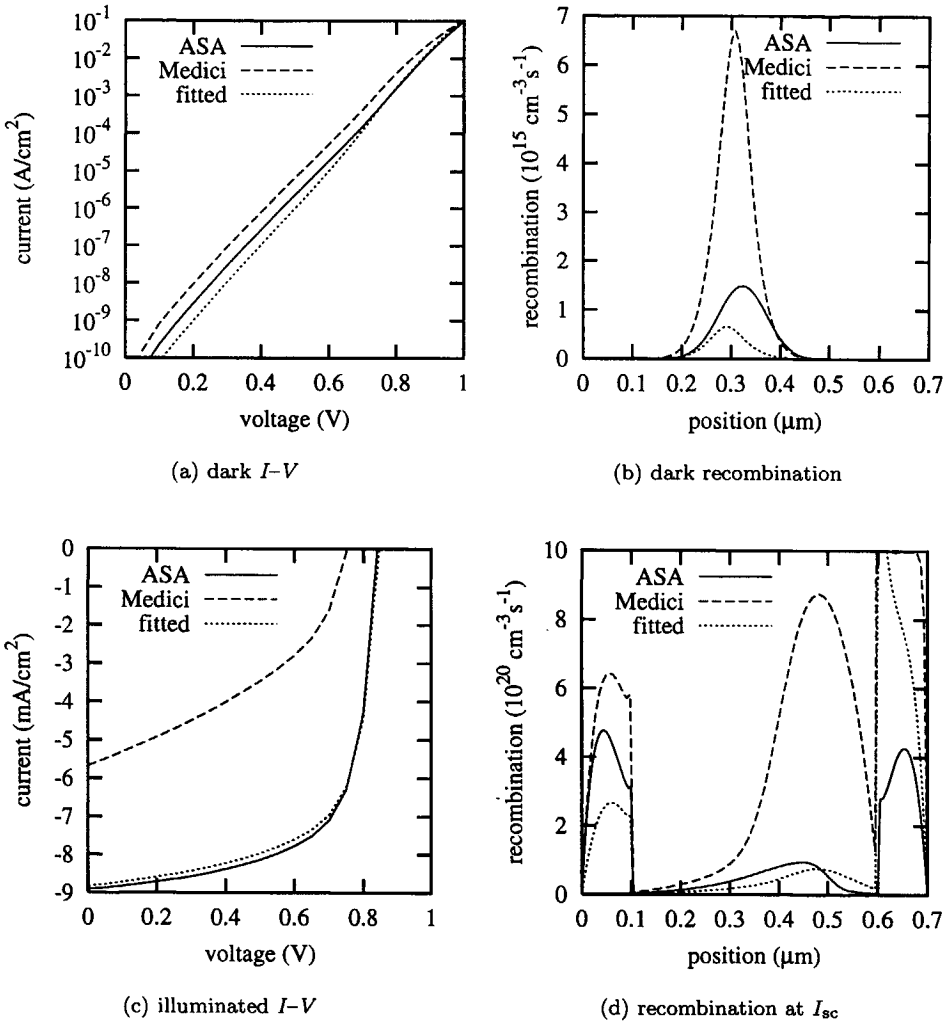


Figure B.3: Simulated dark and illuminated ($G=10^{21} \text{ cm}^{-3} \text{ s}^{-1}$) $I-V$ characteristics and recombination profile under dark ($V=0.2 \text{ V}$) and illuminated ($V=0 \text{ V}$) conditions. The solid lines are simulations in ASA, the dashed lines are simulations in MEDICI, and the dotted lines are simulations in MEDICI using optimised capture rates to fit the dark $I-V$ characteristics in ASA.

```

trap      distrib n.level=50
$         Conduction band tail (acceptors)
trap      n.tot="@ncb*exp((@fener-@eg/2)/@ecb)"
+         taun="1/(@crtail*@ncb*@ecb*exp((@fener-@eg/2)/@ecb))"
+         taup="1/(@crtail*@ncb*@ecb*exp((@fener-@eg/2)/@ecb))"
+         cond="(@fener>@eg/2-0.6)&(@region=ilayer)"
$         Valence band tail (donors)
trap      n.tot="-@nvb*exp(-(@fener+@eg/2)/@evb)"
+         taun="1/(@crtail*@nvb*@evb*exp(-(@fener+@eg/2)/@evb))"
+         taup="1/(@crtail*@nvb*@evb*exp(-(@fener+@eg/2)/@evb))"
+         cond="(@fener<-(@eg/2-0.6))&(@region=ilayer)"
$         Dangling bond acceptor states
trap      n.tot="@ndb/@edb/2.5*exp(-0.5*((@fener-@off1)/@edb)**2)"
+         taun="1/(@crdbc*@ndb*exp(-0.5*((@fener-@off1)/@edb)**2))"
+         taup="1/(@crdbn*@ndb*exp(-0.5*((@fener-@off1)/@edb)**2))"
+         cond="@region=ilayer"
$         Dangling bond donor states
trap      n.tot="-@ndb/@edb/2.5*exp(-0.5*((@fener-@off2)/@edb)**2)"
+         taun="1/(@crdbn*@ndb*exp(-0.5*((@fener-@off2)/@edb)**2))"
+         taup="1/(@crdbc*@ndb*exp(-0.5*((@fener-@off2)/@edb)**2))"
+         cond="@region=ilayer"
:         :
symbolic  newton carriers=0
method   n.damp
solve    initial
symbolic  newton carriers=2
solve    v1=0
loop     steps=4
         assign name=phg n.val=1e13 ratio=100
         photogen a1=@phg
         solve v1=0
l.end
photogen let.file=gp.asa ...

```

Figure B.4: Example input of analytical expression to describe the DOS in α -Si:H.



Appendix C

Analysis of Thin-Film Transistors

Amorphous silicon thin-film transistors (TFT's) were fabricated in the same process as the TJSC. The TFT's were made in a so-called bottom gate configuration, *i.e.*, the wafer substrate was used as the gate electrode and a 200 nm thick thermally grown SiO_2 acts as a gate dielectricum. In this configuration, the design of the TFT is similar to the TJSC (see Fig. C.1). An $a\text{-Si:H}$ n -channel TFT consists of an intrinsic channel region in between two n -doped regions (the source and the drain). The devices have a channel length of 20 μm and a channel width of 1000 μm . The source and drain were formed by the same phosphorus implantations as used for the fabrication of TJSC's (Table 3.1).

The TFT characteristics are shown in Fig. C.2. The devices have a threshold voltage of 8 V and a field-effect mobility of $0.4\sim 0.8\text{ cm}^2\text{V}^{-1}\text{s}^{-1}$ in the saturation regime. The mobility is comparable to reported values [52, 58, 63, 76] and the threshold voltage is also comparable for other bottom-gate configurations [76]. Note that the threshold voltage depends strongly on the defect distribution in the $a\text{-Si:H}$ channel [52, 104] and the type of gate dielectricum [52]. For example, replacing the thermally grown SiO_2 by a plasma deposited oxide, decreased the threshold voltage to 6 V without influencing the mobility. P -channel TFT's can be integrated with TJSC's similarly to n -channel TFT's without additional process steps. The field-effect mobility of p -channel TFT's is low ($\sim 2 \times 10^{-2}\text{ cm}^2\text{V}^{-1}\text{s}^{-1}$),

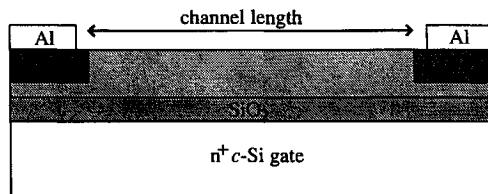


Figure C.1: Schematical drawing of an $a\text{-Si:H}$ TFT in a bottom-gate configuration.

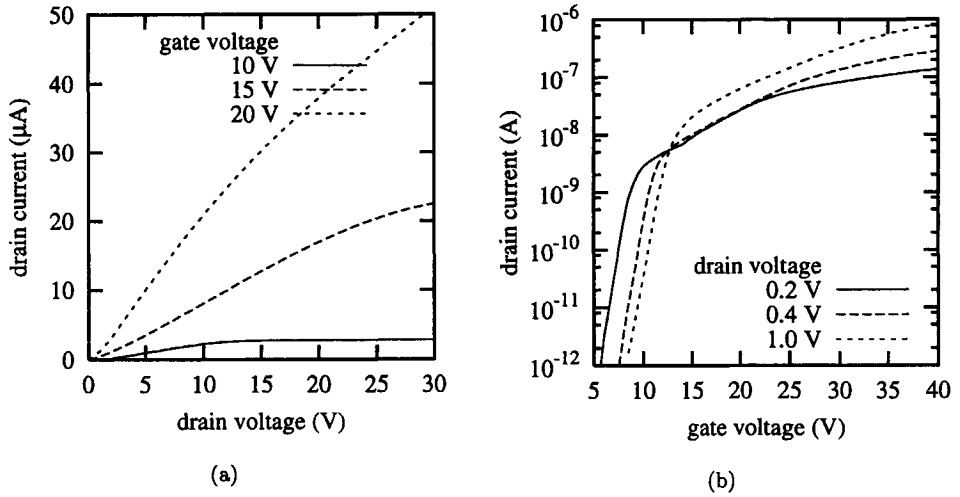


Figure C.2: Characteristics of $a\text{-Si:H}$ n -channel TFT with a channel length of $20 \mu\text{m}$, a channel width of $1000 \mu\text{m}$ in a bottom gate configuration with 200 nm thick thermally grown gate oxide. The device was fabricated in the same process as a TJSC.

however, it is comparable to reported values of $\mu\text{c-Si:H}$ p -channel TFT's [12].



List of Symbols and Abbreviations

α	Absorption coefficient	cm^{-1}
χ	Electron affinity	eV
Φ	Implantation dose	cm^{-2}
η	Efficiency	
λ	Wavelength	nm
μ_e	Electron mobility	$\text{cm}^2\text{V}^{-1}\text{s}^{-1}$
μ_h	Hole mobility	$\text{cm}^2\text{V}^{-1}\text{s}^{-1}$
$\mu\text{c-Si:H}$	Hydrogenated microcrystalline silicon	
ν	Photon frequency	s^{-1}
σ_d	Dark conductivity	$\Omega^{-1}\text{cm}^{-1}$
$\sigma_{db}^{+,0,-}$	Capture rate of dangling bond states in each charge state, respectively	cm^3s^{-1}
σ_{ph}	Photoconductivity	$\Omega^{-1}\text{cm}^{-1}$
σ_l	Lateral straggle of doping profile	nm
σ_e	Capture rate for electrons	cm^3s^{-1}
σ_h	Capture rate for holes	cm^3s^{-1}
σ_p	Longitudinal straggle of doping profile	nm
$\sigma_{tail}^{+,0}$	Capture rate of conduction bandtail states in each charge state, respectively	cm^3s^{-1}
$\sigma_{tail}^{0,-}$	Capture rate of valence bandtail states in each charge state, respectively	cm^3s^{-1}
τ	Lifetime	s
$a\text{-SiC:H}$	Hydrogenated amorphous silicon-carbide	
$a\text{-SiGe:H}$	Hydrogenated amorphous silicon-germanium	
$a\text{-Si:H}$	Hydrogenated amorphous silicon	
$c\text{-Si}$	Crystalline silicon	
D	Width of doped regions	μm
D^+	Positively charged dangling bond	
D^0	Neutral dangling bond	

D^-	Negatively charged dangling bond	
d	Layer thickness	nm
d_i	Depth of doped regions	nm
DBP	Dual-Beam Photospectroscopy	
DOS	Density Of States	$\text{cm}^{-3}\text{eV}^{-1}$
DPM	Defect-Pool Model	
E	Energy	eV
E_{act}	Activation energy	eV
E_c	Conduction-band edge	eV
E_{c0}	Characteristic energy conduction bandtail	eV
E_{corr}	Correlation energy	eV
E_f	Fermi energy	eV
E_{f0}	Equilibrium Fermi level	eV
E_{fi}	Intrinsic Fermi level	eV
E_{fn}	Quasi-Fermi level for electrons	eV
E_{fp}	Quasi-Fermi level for holes	eV
E_g	(mobility) Bandgap	eV
E_{Tauc}	Tauc energy (optical bandgap)	eV
E_v	Valence-band edge	eV
E_{v0}	Characteristic energy valence bandtail	eV
FF	fill factor	
f_{fd}	Fermi-Dirac occupation function	
G	Generation rate	$\text{cm}^{-3}\text{s}^{-1}$
h	Planck's constant	eV s
I	Current	A
I_0	Saturation current	A
I_{sc}	Short-circuit current	A
J	Current density	A/cm^2
J_0	Saturation current density	A/cm^2
J_{sc}	Short-circuit current density	A/cm^2
k	Boltzmann's constant	eV/K, J/K
l	Length of junction	mm
MEMS	Micro Electro-Mechanical System	
m	Ideality factor	
N_A	Acceptor concentration	cm^{-3}
N_c	Effective density of conduction-band states	cm^{-3}
N_{c0}	Density of states at conduction-band edge	$\text{cm}^{-3}\text{eV}^{-1}$
N_D	Donor concentration	cm^{-3}
N_{db}	Dangling-bond density	cm^{-3}
N_{imp}	Impurity concentration	cm^{-3}
N_v	Effective density of valence-band states	cm^{-3}
N_{v0}	Density of states at valence-band edge	$\text{cm}^{-3}\text{eV}^{-1}$
n	Electron concentration	cm^{-3}

n_i	Intrinsic carrier concentration	cm^{-3}
p	Hole concentration	cm^{-3}
P_{ill}	Illumination intensity	mW/cm^2
P_{max}	Maximum power point	W
PECVD	Plasma Enhanced Chemical Vapour Deposition	
PR	Photoresist	
q	Electron charge	C
QE	Quantum Efficiency	
R_p	Longitudinal projected range of doping profile	
R_{srh}	Schockley-Read-Hall recombination rate	nm s^{-1}
RIE	Reactive-Ion Etching	
RT	Reflection-Transmission	
SiO_2	Silicon di-oxide	
T	Temperature	K
T^*	Freeze-in temperature	K
t	Time	s
TCO	Transparent Conductive Oxide	
TFT	Thin-Film Transistor	
TJSC	Transverse Junction Solar Cell	
V	Voltage	V
V_{oc}	Open-circuit voltage	V
v_{th}	Thermal velocity	cm/s
W	Width of intrinsic region	μm
x	Vertical position	nm
y	Lateral position	nm



Bibliography

- [1] ASM Lithography. *Announcing the world's first 0.5 micron i-line wafer stepper* (Specifications of the PAS 5000/50, 1990).
- [2] Y. Bar-Yam, D. Adler, and J.D. Joannopoulos. *Structure and electronic states in disordered systems*. Phys. Rev. Lett. **57**, 467, 1986.
- [3] C. van Berkel, N.C. Bird, C.J. Curling, and I.D. French. *2D image sensing arrays with nip diodes*. Mat. Res. Soc. Symp. Proc. **297**, 939, 1993.
- [4] C. van Berkel, M.J. Powell, A.R. Franklin, and I.D. French. *Quality factor in a-Si:H nip and pin diodes*. J. Appl. Phys. **73**, 5264, 1994.
- [5] J.P. Biersack and L. Haggmark. *A Monte Carlo computer program for the transport of energetic ions in amorphous targets*. Nucl. Instrum. Methods **174**, 257, 1980.
- [6] M. Böhm *et al.* *Image sensors in thin film on ASIC technology - status and future trends*. Mat. Res. Soc. Symp. Proc. **507**, 175, 1998.
- [7] H.M. Branz. *Hydrogen collision model: quantitative description of metastability in amorphous silicon*. Pys. Rev. B **59**, 5498, 1999.
- [8] H.M. Branz and R.S. Crandall. *Defect equilibrium thermodynamics in hydrogenated amorphous silicon: consequences for solar cells*. Solar Cells **27**, 159, 1989.
- [9] D.C. Carlson and C.R. Wronski. *Amorphous silicon solar cell*. Appl. Phys. Lett. **28**, 671, 1976.
- [10] G. de Cesare, P. di Rosa, S. la Monica, R. Salotti, R. Rita, and L. Schirone. *Addressable photosensing elements for 2-dimensional image sensors using a-Si alloy p-i-n diodes*. Mat. Res. Soc. Symp. Proc. **297**, 933, 1993.
- [11] I. Chen and S. Lee. *On the current-voltage characteristics of amorphous hydrogenated Schottky diodes*. J. Appl. Phys. **53**, 1045, 1982.

- [12] Y. Chen and S. Wagner. *Inverter made of complementary p and n channel transistors using a single directly deposited microcrystalline silicon film*. Appl. Phys. Lett. **75**, 1125, 1999.
- [13] P.G. Le Comber, W.E. Spear, and A. Ghaith. *Amorphous silicon field-effect device and possible application*. Elec. Lett. **15**, 179, 1979.
- [14] A.T.W. Driessen. Internal communication.
- [15] A.L. Fahrenbruch and R.H. Bube. *Fundamentals of solar cells* (Academic Press, New York, 1983).
- [16] F.J. Fonseca and R. Galloni. *Electrical activation of potassium and phosphorus implanted ions in hydrogenated amorphous silicon*. Philos. Mag. B. **67**, 107, 1993.
- [17] N. Fukuda, H. Tanaka, K. Miyachi, Y. Ashida, Y. Ohashi, and A. Nitta. *Fabrication of amorphous silicon solar cells with high performance such as fill factor of 0.77 and conversion efficiency of 12.0%*. IEEE Photovoltaic Specialists Conf. Proc. 1998.
- [18] R. Galloni, M. Ruth, A. Desalvo, and Y.S. Tsuo. *Low energy ion-beam post hydrogenation of phosphor-implanted amorphous silicon films*. Phys. B **170**, 273, 1991.
- [19] R. Galloni, Y.S. Tsuo, D.W. Baker, and F. Zignani. *Doping and hydrogenation by ion implantation of glow discharge deposited amorphous silicon films*. Appl. Phys. Lett. **56**, 241, 1990.
- [20] R. Galloni, Y.S. Tsuo, and F. Zignani. *Ion implantation and hydrogen passivation in amorphous silicon films*. Nucl. Instrum. Methods Phys. Res. B **39**, 386, 1989.
- [21] M.D. Giles. in *VLSI Technology* ed. by S.M. Sze (McGraw-Hill Int., 1988), second edn.
- [22] *For example*, A.S. Grove. *Physics and Technology of Semiconductor Devices* (J. Wiley & Sons, New York, 1967), first edn.
- [23] M. Hack and M. Shur. *Theoretical modeling of amorphous silicon-based alloy pin solar cells*. J. Appl. Phys. **54**, 5858, 1983.
- [24] R.N. Hall. *Electron-hole recombination in germanium*. Phys. Rev. **87**, 387, 1952.
- [25] V. Halpern. *The statistics of recombination via dangling bonds in amorphous silicon*. Philos. Mag. B **54**, 473, 1986.

- [26] Y. Hamakawa, H. Okamoto, and Y. Nitta. *A new type of amorphous silicon photovoltaic cell generating more than 2.0 v*. Appl. Phys. Lett. **35**, 187, 1979.
- [27] M.S. Haque, H.A. Naseem, and W.D. Brown. *Degradation and failure mechanisms of a-Si:H solar cells with aluminum contacts*. Proc. 1st World Conference on Photovoltaic Energy Conversion p. 642, 1994.
- [28] M.S. Haque, H.A. Naseem, and W.D. Brown. *Interaction of aluminum with hydrogenated amorphous silicon at low temperatures*. J. Appl. Phys. **75**, 3928, 1994.
- [29] L.J. Hornbeck. *128 × 128 Deformable mirror device*. IEEE Trans. Elec. Dev. **30**, 539, 1983.
- [30] J. Hou, J. Xi, F. Kampas, S. Bae, and S.J. Fonash. *Non-local recombination in tunnel junctions of multijunction amorphous Si alloy solar cells*. Mat. Res. Symp. Proc **336**, 717, 1994.
- [31] J. Hsieh and W. Fang. *A novel microelectrostatic torsional actuator*. Sensors and Actuators **79**, 64, 2000.
- [32] G.A.M. Hurkx, D.B.M. Klaassen, and M.P.G. Knuvers. *A new recombination model for device simulation including tunneling*. IEEE Trans. Elec. Dev. **39**, 331, 1992.
- [33] Integrated Systems Engineering AG. <http://www.ise.com/>, 1997.
- [34] L. Jiang, J.H. Lyou, E.A. Schiff, Q. Wang, and Q. Yuan. *Open-circuit voltage physics in amorphous silicon solar cells*. Mat. Res. Soc. Symp. Proc. **609**, A18.3.1, 2000.
- [35] D. Jousse, J. Saïd, and J.C. Bruyère. *Boron doping of amorphous silicon hydrogenated silicon films prepared by r.f. sputtering*. Thin Solid Films **124**, 49, 1985.
- [36] S. Kalbitzer, G. Müller, P.G. Le Comber, and W.E. Spear. *The effects of ion implantation on the electrical properties of amorphous silicon*. Philos. Mag. B **41**, 439, 1980.
- [37] L.E. Katz. in *VLSI Technology* ed. by S.M. Sze (McGraw-Hill Int., 1988), second edn.
- [38] H. Koinuma, H. Fujioka, C. Hu, T. Koida, and M. Kawasaki. *Structure and numerical simulation of field effect solar cell*. Mat. Res. Soc. Symp. Proc **426**, 95, 1996.

- [39] M.A. Kroon and R.A.C.M.M. van Swaaij. *Activation energy of boron and phosphorus implanted amorphous silicon*. submitted to Thin Solid Films 2001.
- [40] M.A. Kroon and R.A.C.M.M. van Swaaij. *Spatial effects on ideality factor of amorphous silicon pin diodes*. J. Appl. Phys. **90**, 994, 2001.
- [41] M.A. Kroon, R.A.C.M.M. van Swaaij, and J.W. Metselaar. *a-Si:H transverse junction solar cell with interdigitated finger pattern: calculations of efficiency and series resistance*. Proc. of 1st workshop on Semiconductor Advances of Future Electronics (SAFE) p. 319, 1998.
- [42] M.A. Kroon, R.A.C.M.M. van Swaaij, and J.W. Metselaar. *I-V characteristics of a-Si:H p-i-n diodes with uniform and non-uniform defect distributions*. Mat. Res. Soc. Symp. Proc. **609**, A10.3.1, 2000.
- [43] M.A. Kroon, R.A.C.M.M. van Swaaij, and J.W. Metselaar. *Miniature high-voltage a-Si:H solar cell for integration in micro-electronic devices*. Proc. 16th European Photovoltaic Solar Energy Conference, Glasgow p. B118, 2000.
- [44] M.A. Kroon, R.A.C.M.M. van Swaaij, M. Zeman, V.I. Kuznetsov, and J.W. Metselaar. *Hydrogenated amorphous silicon transverse junction solar cell*. Appl. Phys. Lett. **72**, 209, 1998.
- [45] M.A. Kroon, R.A.C.M.M. van Swaaij, M. Zeman, and J.W. Metselaar. *Study of the design of the a-Si:H transverse junction solar cell*. Proc. 2nd World Conference on Photovoltaic Solar Energy Conversion, Vienna 1, 914, 1998.
- [46] J.B. Lee, Z. Chen, M.G. Allen, and A. Rohatgi. *A hybrid microsystem using a high voltage solar cell array as a power supply*. International Symposium on Microelectronics, Boston, MA p. 438, 1994.
- [47] J.B. Lee, Z. Chen, M.G. Allen, A. Rohatgi, and R. Arya. *A high voltage solar cell array as an electrostatic MEMS power supply*. Proc. IEEE Micro Electro Mechanical Systems p. 331, 1994.
- [48] F. Lemmi, J.T. Rahn, and R.A. Street. *Lateral conduction in structured amorphous silicon $p^+ - i - n^+$ photodetectors*. J. non-Cryst. Solids **266-269**, 1203, 2000.
- [49] C. Longeaud, J.P. Kleider, D. Mencaraglia, A. Amaral, and C.N. Carvalho. *Determination of the density of states in p-doped hydrogenated amorphous silicon by means of the modulated photocurrent experiment*. J. non-Cryst. Solids **164-166**, 423, 1993.

- [50] H. Matsuura, A. Matsuda, H. Okushi, and K. Tanaka. *Dark current transport mechanism of pin hydrogenated amorphous silicon diodes*. J. Appl. Phys. **58**, 1578, 1985.
- [51] W.M. Moreau. *Semiconductor Lithography* (Plenum Press, New York, 1988).
- [52] P.N. Morgan. *Ph.D. thesis* (Cambridge University (UK), 1995).
- [53] G. Müller, S. Kalbitzer, and H. Mannsperger. *A chemical-bond approach to doping, compensation and photo-induced degradation in amorphous silicon*. Appl. Phys. A **39**, 243, 1986.
- [54] G. Müller, H. Mannsperger, and S. Kalbitzer. *Substitutional doping of amorphous silicon: A comparison of different doping mechanisms*. Philos. Mag. B **53**, 257, 1986.
- [55] V. Nádazdy, R. Durný, and E. Pincik. *Evidence for the improved defect-pool model for gap states in amorphous silicon from charge DLTS experiments on undoped a-Si:H*. Phys. Rev. Lett. **78**, 1102, 1992.
- [56] S. Nakano *et al.* *Laser patterning method for integrated type a-Si solar cell submodules*. Jpn. J. Appl. Phys. **25**, 1936, 1986.
- [57] J. Nakata, S. Wagner, H. Glesková, P.A. Stolk, and J.M. Poate. *Recovery kinetics of phosphorus ion-implanted a-Si:H*. Mat. Res. Symp. Proc. **420**, 653, 1996.
- [58] S. Nishida, H. Ushida, and S. Kaneko. *A new self-aligned a-Si TFT using ion doping and chromium silicide formation*. Mat. Res. Soc. Symp. Proc. **219**, 303, 1991.
- [59] G.J.L. Ouwering. *Ph.D. thesis* (Delft University of Technology, 1989).
- [60] K.E. Petersen. *Micromechanical membrane switches on silicon*. IBM J. Res. Develop. p. 376, 1979.
- [61] M.J. Powell and S.C. Deane. *Improved defect-pool model for charged defects in amorphous silicon*. Phys. Rev. B. **48**, 10815, 1993.
- [62] M.J. Powell and S.C. Deane. *Defect-pool model and the hydrogen density of states in hydrogenated amorphous silicon*. Phys. Rev. B. **53**, 10121, 1996.
- [63] M.J. Powell, C. Glasse, J.E. Curran, J.R. Hughes, I.D. French, and B.F. Martin. *A fully self-aligned amorphous silicon TFT technology for large area image sensors and active-matrix displays*. Mat. Res. Soc. Symp. Proc. **507**, 91, 1998.
- [64] A.J. van Roosmalen, J.A.G. Baggerman, and S.J.H. Brader. *Dry etching for VLSI* (Plenum Press, New York, 1991).

- [65] C.T. Sah and W. Shockley. *Electron-hole recombination statistics in semiconductors through flaws with many charge conditions*. Phys. Rev. **109**, 1103, 1958.
- [66] M.B. Schubert *et al.* *Amorphous silicon photodiodes for replacing degenerated photoreceptors in the human eye*. Mat. Res. Soc. Symp. Proc. **467**, 913, 1997.
- [67] G. Schumm. *Chemical equilibrium description of stable and metastable defect structures in a-Si:H*. Phys. Rev. B. **49**, 2427, 1994.
- [68] G. Schumm and G.H. Bauer. *Equilibrium and non-equilibrium gap state distribution in a-Si:H*. J. Non-Cryst. Solids. **137&138**, 315, 1991.
- [69] R.D. Schutz. in *VLSI Technology* ed. by S.M. Sze (McGraw-Hill Int. Editions, 1988), second edn.
- [70] W. Shockley and W.T. Read Jr. *Statistics of the recombination of holes and electrons*. Phys. Rev. **87**, 835, 1952.
- [71] Silvaco Int. *Atlas Users Manual version 1.5.0*, 1997.
- [72] Silvaco Int. <http://www.silvaco.com/>, 1997.
- [73] J.G. Simmons and G.W. Taylor. *Nonequilibrium steady-state statistics and associated effects for insulators and semiconductors containing an arbitrary distribution of traps*. Phys. Rev. B. **4**, 502, 1971.
- [74] W.E. Spear and P.G. Le Comber. *Substitutional doping of amorphous silicon*. Solid State Commun. **17**, 1193, 1975.
- [75] D.L. Staebler and C.R. Wronski. *Reversible conductivity changes in discharge-produced amorphous Si*. Appl. Phys. Lett. **31**, 292, 1977.
- [76] B. Stannowski, A.M. Brockhoff, and R.E.I. Schropp. *Stability study of thin-film transistors made by hot-wire chemical vapor deposition*. Proc. 2nd workshop on semiconductor advances for future electronics (SAFE) p. 467, 1999.
- [77] R.A. Street. *Doping and the Fermi energy in amorphous silicon*. Phys. Rev. Lett. **49**, 1187, 1982.
- [78] R.A. Street. *Localized states in doped a-Si:H*. J. Non-Cryst. Solids **77&78**, 1, 1985.
- [79] R.A. Street. *Hydrogenated amorphous silicon* (Cambridge University Press, Cambridge (UK), 1991), first edn.
- [80] R.A. Street, M. Hack, and W.B. Jackson. *Mechanisms of thermal equilibration in doped amorphous silicon*. Phys. Rev. B **37**, 4209, 1988.

- [81] R.A. Street, J. Kakalios, C.C. Tsaj, and T.M. Hayes. *Thermal-equilibrium processes in amorphous silicon*. Phys. Rev. B **35**, 1316, 1987.
- [82] R.A. Street and K. Winer. *Defect equilibria in undoped a-Si:H*. Phys. Rev. B **40**, 6236, 1989.
- [83] R.A. Street *et al.* *Two dimensional amorphous silicon image sensor arrays*. Mat. Res. Soc. Symp. Proc. **377**, 757, 1995.
- [84] M. Stutzmann. *The defect density in amorphous silicon*. Philos. Mag. B **60**, 531, 1989.
- [85] M. Stutzmann. *A comment on thermal defect creation in hydrogenated amorphous silicon*. Philos. Mag. Lett. **66**, 147, 1992.
- [86] M. Stutzmann, D.K. Biegelsen, and R.A. Street. *Detailed investigation of doping in hydrogenated amorphous silicon and germanium*. Phys. Rev. B **35**, 5666, 1987.
- [87] M. Stutzmann, W.B. Jackson, and C.C. Tsai. *Kinetics of the Staebler-Wronski effect in hydrogenated amorphous silicon*. Appl. Phys. Lett. **45**, 1075, 1984.
- [88] M. Stutzmann, W.B. Jackson, and C.C. Tsai. *Light-induced metastable defects in hydrogenated amorphous silicon: A systematic study*. Phys. Rev. B **32**, 23, 1985.
- [89] V. Suntharalingam and H.M. Branz. *On modeling trivalent dangling bonds with bivalent levels*. Mat. Res. Soc. Symp. Proc. **336**, 153, 1994.
- [90] K. Suzuki, R. Sudo, Y. Tada, M. Tomotani, T. Feudel, and W. Fichtner. *Comprehensive analytical expression for dose dependent ion-implanted impurity concentration profiles*. Solid-St. Elec. **42**, 1998.
- [91] R.A.C.M.M. van Swaaij, V. Nádazdy, M. Zeman, E. Pincik, and J.W. Metselaar. *Defect re-distribution in amorphous silicon below equilibration temperature*. J. Non-Cryst. Solids. **266-269**, 553, 2000.
- [92] J.A. Swanson and P.V. Horton. *The photovoltaic cell*. United States Patent Office no. 2,986,591, 1961.
- [93] S.M. Sze. *Semiconductor sensors* (Wiley, New York, 1994).
- [94] H. Takato, T. Sekigawa, and R. Shimokawa. *Fabrication of integrated silicon-on-insulator solar cells*. Proc. 2nd World Conference on Photovoltaic Solar Energy Conversion, Vienna p. 1810, 1998.
- [95] G. Tao. *Ph.D. thesis* (Delft University of Technology, 1994).

- [96] Y. Tawaka, M. Kondo, H. Okamoto, and Y. Hamakawa. *Hydrogenated amorphous silicon carbide as a window material for high efficiency a-Si solar cells*. Solar En. Mater. **6**, 299, 1982.
- [97] Technology Modeling Associates Inc. *Tsuprem-4 User's Manual version 6.5*, 1997.
- [98] Technology Modeling Associates Inc. <http://www.avanticorp.com>, 1998.
- [99] Technology Modeling Associates Inc. *Medici Users Manual version 4.0.0*, 1998.
- [100] M. Topič, F. Smole, A. Groznic, and J. Furlan. *New bias-controlled three-color detectors using stacked a-SiC:H/a-Si:H heterostructures*. Mat. Res. Soc. Symp. Proc. **377**, 779, 1995.
- [101] M. Trijssenaar. *Ph.D. thesis* (Delft University of Technology, 1995).
- [102] H.K. Tsai and S.C. Lee. *Amorphous SiC/Si three-color detector*. Appl. Phys. Lett. **52**, 275, 1988.
- [103] Q. Wang, H. Antoniadis, E.A. Schiff, and S. Guha. *Electron-drift-mobility measurements and exponential conduction-band tails in hydrogenated amorphous silicon-germanium alloys*. Phys. Rev. B. **47**, 9435, 1993.
- [104] R.B. Wehrspohn, S.C. Deane, I.D. French, I.G. Gale, M.J. Powell, and R. Brüggeman. *Urbach energy dependence of the stability in amorphous silicon thin-film transistors*. Appl. Phys. Lett. **74**, 3374, 1999.
- [105] J.H. Wei and S.C. Lee. *Electrical and optical properties of implanted amorphous silicon*. J. Appl. Phys. **76**, 1033, 1994.
- [106] J.A. Willemen. *Ph.D. thesis, Delft University of Technology* (Universal Press, Veenendaal, the Netherlands, 1998).
- [107] K. Winer. *Defect formation in a-Si:H*. Phys. Rev. B **41**, 12150, 1990.
- [108] J. Yang, A. Banerjee, K. Lord, and S. Guha. *Correlation of component cells with high efficiency amorphous silicon alloy triple-junction solar cells and modules*. Proc. 2nd World Conference on Photovoltaic Energy Conversion p. 387, 1998.
- [109] L. Yang and L.F. Chen. *Thickness dependence of light induced degradation in a-Si:H solar cells*. J. Non-Cryst. Solids. **127&138**, 1189, 1991.
- [110] M. Zeman, M.A. Kroon, and J.J.G. van den Heuvel. *ASA Users Manual version 3.0*, 1999.

- [111] J.F. Ziegler. *SRIM Instruction Manual* (IBM Research, Yorktown, NY (USA), April 16, 1997).
- [112] A.J.M.M. van Zutphen. *Ph.D. thesis* (Delft University of Technology, 2001). to be published.



Summary

This thesis describes the research which was carried out during the last four years on the *transverse junction solar cell*. This solar cell is a novel concept, which is fabricated with standard technology for micro-electronics. The initial aim was to study the feasibility of the concept, however, after the conclusions had been drawn, the research project focussed on some specific properties of this solar cell.

In a solar cell, the light is converted to electricity in two steps: first, electrons are excited from a semiconducting material (generation of electron-hole pairs). Second, these free charge carriers are separated by an internal electric field. This field is established at the interface of a *p*-type and an *n*-type semiconductor. The electric field persists in an intrinsic region in between the *p*-type and the *n*-type region. In the configuration of a conventional amorphous silicon solar cell, this *pin* junction is a stacked-layer structure, in which the direction of the electric field is perpendicular to the illuminated surface. The transverse junction solar cell has the specific feature that the *pin* junction is perpendicular to the illuminated surface. Such a configuration has several advantages

- The light can enter directly into the intrinsic region. Only in this region, the generated charge carriers can be collected. In a conventional solar cell the light must pass the *p* layer and a transparent contact.
- The contacts are positioned on top of the *p* region and the *n* region. Therefore, several transverse junction solar cells can be easily connected in series, such that a higher output voltage is obtained.
- The transverse junction solar cell is made using standard technology for the fabrication of micro-electronic components. Hence, these solar cells can be integrated in microchips.

The idea for this cell is not new; the transverse concept has been used several times for (poly)crystalline solar cells. However, the novelty of this work is that the transverse concept has been applied to a thin-film solar cell, made of amorphous silicon. Amorphous silicon is grown at a relatively low temperature ($< 250^{\circ}\text{C}$), which allows deposition on a range of substrates, like glass, plastic foil, . . . , and microchips. For example, with an integrated solar cell a self-supplying chip can be

made. Such an integration is particularly interesting for micromechanical devices (MEMS) which require a high voltage, that is not supplied by the peripheral electronic circuit. Series connected arrays of transverse junction solar cells have been fabricated on a very small scale. For example, an array consisting of 100 cells provides an open-circuit voltage of 66 V on a length scale of only 0.3 mm.

The performance of the transverse junction solar cell has been analyzed extensively. The open-circuit voltage is ~ 0.80 V, which is slightly less than in conventional amorphous silicon solar cells. The *fill factor* is relatively low (~ 0.50), which is due to the fact that the mean path length of the generated holes is larger than in conventional solar cells, thus increasing the probability of recombination. The short-circuit current is two-and-a-half times less than in conventional solar cells. This is partly due to the enhanced recombination and partly due to the poor incoupling of light. The light incoupling can be improved by an anti-reflection coating at the top side and back reflector at the bottom side of the active layer of the solar cell. Furthermore, spectral response measurements have indicated that the blue response of the transverse junction solar cell is relatively low. An important cause of the poor blue response is that under illumination, the electric field has a substantial vertical component, which increases the path length of the photo-generated carriers before collection. Hence, the recombination probability increases. Two-dimensional computer simulations show that this vertical field component is due to additional space charge in the top of the cell under illumination. In the top part of the cell, the optical generation is higher, resulting in a higher positive space-charge density than deeper in the cell.

The performance of the transverse junction solar cell depends strongly on inaccuracies and variations in the fabrication process. Besides, the width of the intrinsic region should be at least 0.5 micrometers in order to prevent overlay of the doped regions, due to lateral scattering of the implanted doping atoms. The resulting conversion efficiency of the transverse junction solar cell is 2–3%, calculated on the active area of the cell, *i.e.*, the area of the doped regions has not been taken into account. The area loss can be reduced by illuminating the cell from the bottom side, through a transparent substrate. If the thickness of the cell is larger than the depth of the doped regions, 'quasi-intrinsic' regions are present in between the doped regions and the substrate. Photovoltaic conversion occurs in these regions as well, thus increasing the active area. Such a configuration resulted in $\sim 70\%$ higher short-circuit current as compared to illumination from the top side, for a cell with $1 \mu\text{m}$ wide doped regions. However, the fill factor is lower.

Finally, the transverse junction solar cell has been applied as a test device to study the thermodynamic equilibration of defect states. At first sight, the defect density is a property of amorphous silicon; however, the defect density depends on the Fermi energy. In a *pin* junction, the Fermi energy depends on the position in the device; hence, the defect density has also a spatial distribution. This distribution was analyzed by dark current–voltage measurements. In transverse junction solar cells, the spatial distribution of defects is fundamentally different

from conventional amorphous silicon solar cells. The difference is caused by the fabrication process, in which the defects are formed under different thermodynamic conditions. The dark current in an amorphous silicon diode is completely determined by recombination of electron-hole pairs at *dangling bond* states. It turned out that existing physical models do not describe the origin of the dark current correctly. Therefore, using the device simulator ASA, a new model was derived to describe the dark current-voltage characteristics. This model applies to conventional amorphous silicon solar cells as well as to the transverse junction solar cell.



Samenvatting

Dit proefschrift beslaat het onderzoek dat de afgelopen vier jaar verricht is aan de *transversale junctie zonnecel*. Dit is een nieuw concept zonnecel, dat met technologieën uit de micro-elektronica gemaakt wordt. Aanvankelijk was de aard van dit onderzoek een haalbaarheidsstudie, maar nadat de conclusies getrokken waren, verschoof het aandachtsgebied naar een aantal bijzondere eigenschappen van deze zonnecel.

In een zonnecel wordt licht in twee stappen omgezet in elektriciteit: eerst worden elektronen uit een halfgeleidend materiaal vrij gemaakt (generatie van elektron-gat paren) en vervolgens worden deze vrije ladingsdragers gescheiden onder invloed van een intern elektrisch veld. Dit veld is verkregen aan de overgang tussen een *p*-type halfgeleider en een *n*-type halfgeleider. Hiertussen bevindt zich nog een intrinsiek deel, waarover het interne elektrische veld heerst. Gewoonlijk is deze *pin* overgang een gestapelde structuur, waardoor het elektrische veld loodrecht op het belichte oppervlak van de zonnecel staat. Het bijzondere aan de transversale junctie zonnecel is dat de *pin* overgang dwars op het belichte oppervlak staat, waardoor het elektrische veld parallel loopt. Dit heeft een aantal voordelen

- Het licht kan direct op het intrinsieke gebied invallen. Alleen hier worden de gegenereerde ladingsdragers namelijk gescheiden. In een gewone zonnecel moet het licht eerst door de *p*-laag en een transparant contact;
- De contacten bevinden zich bovenop het *p*-gebied en het *n*-gebied. Hierdoor zijn meerdere transversale junctie zonnecellen gemakkelijk in serie te schakelen, waardoor een hogere uitgangsspanning verkregen wordt;
- De transversale junctie zonnecel wordt gemaakt met technologieën die compatibel zijn met de fabricage van micro-elektronische componenten. Daardoor kunnen deze zonnecellen geïntegreerd worden met microchips.

Het idee voor deze cel is niet nieuw; op (poly)kristallijne zonnecellen is het transversale concept al een aantal keren toegepast. De noviteit is echter dat het hier een dunne-film zonnecel betreft, die van amorf silicium gemaakt is. Amorf silicium wordt bij een relatief lage temperatuur ($< 250^{\circ}\text{C}$) gegroeid, waardoor dit materiaal op diverse substraten gedeponeerd kan worden, zoals glas, kunststof

folie, ... en microchips. Zo kan bijvoorbeeld een chip gemaakt worden die gevoed wordt door een geïntegreerde zonnecel. Dit is met name interessant voor allerlei micromechanische componenten (MEMS) die een hoge voedingsspanning vereisen, die niet door de omliggende elektronica geleverd wordt. Met succes zijn serieschakelingen gefabriceerd op zeer kleine schaal. Bijvoorbeeld, een serieschakeling bestaande uit 100 cellen, levert een openklemspanning van 66 V over een lengte van slechts 0.3 mm.

De werking van de transversale junctie zonnecel is uitgebreid geanalyseerd. De openklemspanning is ~ 0.80 V, wat slechts een fractie lager is dan gewone amorf silicium zonnecellen. De *fill factor* is aan de lage kant (~ 0.50). Dit komt doordat de gemiddelde weglengte van de gegenereerde gaten langer is dan in gewone zonnecellen, waardoor de kans op recombinatie toeneemt. De kortsluitstroom is tweeënhalve keer zo laag als in gewone zonnecellen. Dit komt door de hogere kans op recombinatie en door de slechtere inkoppeling van het licht in de cel. De lichtinkoppeling kan overigens eenvoudig verbeterd kunnen worden door een anti-reflectielaag aan de bovenzijde en een reflecterend materiaal aan de onderzijde van de zonnecel aan te brengen. Verder blijkt uit spectraalresponsmetingen dat de gevoeligheid voor blauw licht te wensen over laat. Een belangrijke oorzaak hiervoor is dat het interne elektrische veld een aanzienlijke verticale component heeft, waardoor de gegenereerde ladingsdragers via een omweg naar de gedoteerde gebieden gaan. Deze extra veldcomponent wordt veroorzaakt door de extra ruimtelading die ontstaat onder belichting van de cel, zo blijkt uit twee-dimensionale simulaties. Bovenin de cel is de optische generatie hoger, waardoor er daar meer positieve ruimtelading is dan onder in de cel.

De karakteristieken van de transversale junctie zonnecel zijn zeer gevoelig voor onnauwkeurigheden en variaties in het fabricageproces. Verder moet het intrinsieke gebied minimaal een halve micrometer breed zijn om te voorkomen dat de gedoteerde gebieden elkaar gaan overlappen ten gevolge van laterale verstrooiing van de geïmplanteerde doteringsatomen. Al met al is het rendement van de transversale junctie zonnecel zo'n 2 à 3%, berekend over het actieve oppervlak. Het verlies aan oppervlak door de gedoteerde gebieden is dus niet meegerekend. Dit verlies kan overigens beperkt worden als de zonnecel vanaf de onderzijde, door een transparant substraat, belicht wordt. Indien de dikte van de cel groter is dan de diepte van de gedoteerde gebieden, bevindt zich een quasi-intrinsiek gebied tussen deze gebieden en het substraat. Ook hier vindt fotovoltaïsche conversie plaats, waardoor het actieve oppervlak groter wordt. In deze configuratie wordt de kortsluitstroom zo'n 70% hoger in vergelijking met belichting van de bovenzijde wanneer de gedoteerde gebieden 1 μm breed zijn. Dit leidt echter wel tot een lagere *fill factor*.

Ten slotte heeft de transversale junctie zonnecel gefungeerd als een teststructuur om de thermodynamische equilibratie van defecttoestanden te onderzoeken. Op het eerste gezicht is de defectdichtheid een eigenschap van het amorf silicium, maar deze hangt wel af van het Fermi-niveau. In een *pin* overgang is dit niveau afhankelijk van de positie en daarom heeft de defectdichtheid ook een

plaatsafhankelijkheid. Door middel van donkerstroom–spanningsmetingen is de ruimtelijke verdeling van defecten in de *pin* junctie geanalyseerd. Deze blijkt in de transversale junctie zonnecel fundamenteel anders te zijn dan in gewone amorf silicium zonnecellen. Dit is een gevolg van verschillen in het fabricageproces, waardoor de defecten onder andere thermodynamische condities gevormd worden. De donkerstroom in een amorf silicium diode wordt geheel bepaald door recombinatie van elektron–gat paren in *dangling-bond* toestanden. Bestaande modellen voor de donkerstroom–spanningskarakteristiek bleken niet correct te zijn. Daarom is met behulp van het simulatieprogramma ASA een nieuw model voor deze karakteristiek afgeleid, dat zowel op gewone amorf silicium zonnecellen als op transversale junctie zonnecellen van toepassing is.



Nawoord

Dit proefschrift bevat de wetenschappelijke resultaten van vier jaar onderzoek. Alle twijfel, de frustraties en het cynisme heb ik achterwege gelaten, want terugkijkend op mijn promotietijd wil ik toch een tevreden gevoel en veel goede herinneringen overhouden. De gezelligheid en de prettige samenwerking met veel collega's gaven belangrijke steun en doorzettingsvermogen bij het volbrengen van dit werk. Dan denk ik vooral terug aan die memorabele avonden met kuitenbier in Stads-herberg de Mol, met Slowaakse wodka thuis bij Miro, op Koninginnedag in Café Bebop en al die avonden doorzakken op en rond de Beestenmarkt met onder andere Paul, Erik, Barry, Marcel, Wibó, Jurgen en Roelof. Verder de donderdagavondse etentjes thuis bij Ray, Wibó, Marcel, Léon of Ad, waarbij vooral Léons keuken het moest ontgelden door chocoladecake en pannenkoeken. Met Marcel en Barry naar Feyenoord in de Kuip. De zeildagen op de Kaagerplas, waar je altijd nat werd, ook als je niet overboord ging. De barbecues op het grasveldje voor bij DIMES en op de zomerse donderdagavond in het Delftse Hout. De onvergetelijke rondreis door Amerika met Bas. Met Ad door Wenen en met Paul door San Francisco struinen

...

Maar ook tijdens werktijden was er veel te beleven, waarvoor ik dank verschuldigd ben. Ten eerste mijn kamergenoten. Ray Hueting bracht mij snel alle ins & outs van de vakgroep bij. Joost Willemen leerde mij heel veel over amorf silicium zonnecellen en over computersimulaties. Barry van Dijk bedank ik voor de koffie, het lotgenotengevoel dat ons beiden af en toe becroop en de vele plaagstoten die je scherp houden. Bas Korevaar was ook een aanwinst voor de sfeer op de kamer en met hem heb ik veel aangename gesprekken gehad. Ook Amir Vosteen heeft mij vaak gemotiveerd om de klus te klaren.

En dan moest er ook nog eens onderzoek gedaan worden. Veel technici hebben mij geholpen bij het maken van de zonnecellen. Ben Girwar en Jan van Staden bedank ik voor het deponeren van de lagen en voor veel goede raad. Bert Goudena verzorgde mijn cleanroom cursus en had een flexibele instelling als ik weer eens met een ongebruikelijk proces of materiaal wilde experimenteren. De technici van de cleanroom zorgden voor een prettige en constructieve werksfeer, waarbij ik in het bijzonder de leden van het 'GeKa'-team en het implantatieteam wil bedanken voor hun inzet en hun adviezen: Henk van Zeijl, Alfred Apon, Tom Scholtes, John Slabbekoorn, Jurgen Bertens en Ruud Klerks. Voor de hulp bij het

meetwerk bedank ik Arjan Driessen en Erik Jan Geluk. Ook Amir Vosteen en Joost van den Heuvel hebben een belangrijke bijdrage geleverd aan het opbouwen van de apparatuur en het interpreteren van de resultaten. Jan Chris Staalenburg bedank ik voor het oplossen van veel ellende die veroorzaakt werd door de heren Hewlett, Packard en, niet te vergeten, Gates en zijn kornuiten. Marian Roozenburg en Jeanne Sirks bedank ik voor al het regelwerk, met name waar dat het organiseren van talloze borrels, feestjes en etentjes betrof.

Mijn promotie-onderzoek was niet mogelijk geweest zonder de bijdrage van de stafleden van de zonnecelgroep: René van Swaaij, Vladimir Kuznetsov, Miro Zeman en Wim Metselaar. Hierbij bedank ik in het bijzonder voor de dagelijkse begeleiding van René, die een substantiële bijdrage heeft geleverd aan de totstandkoming van dit proefschrift. Mijn promotor Kees Beenakker wist de perikelen van een promovendus altijd een ander cachet te geven met zijn heldere visies. Met name in de laatste fase was hij een stimulerende kracht achter mijn proefschrift.

Ook alle overige promovendi, technici en studenten van de vakgroep Elektronische Componenten, Technologie en Materialen wil ik bedanken voor de gezelligheid en de prettige werksfeer. Voorts bedank ik Attie-Jan Grasso voor de opmaak van het kaft.

Rest mij vooral om ontzettend dankbaar te zijn voor heel veel steun en warmte van mijn vrienden, familie, mijn ouders en Catelijne.

*Delft, 30 mei 2001,
Martin Kroon*



Curriculum Vitae

Martin Kroon werd geboren op 31 juli 1973 in Dedemsvaart. Na een jaar verhuisde hij naar Kampen, alwaar hij zijn jeugd doorbracht. In 1991 behaalde hij zijn diploma V.W.O. aan het Johannes Calvijn Lyceum en verhuisde vervolgens naar Groningen om er Technische Natuurkunde (ir.) te gaan studeren aan de Rijksuniversiteit Groningen. Tijdens deze studie werden twee uitstapjes gemaakt: in 1994-1995 verbleef hij een half jaar in Straatsburg, Frankrijk, onder meer om er te studeren aan de Université Louis Pasteur. In 1995 liep hij stage bij het Paul Scherrer Instituut te Zürich, Zwitserland. Hier deed hij onderzoek naar het verbeteren van de metaalcontacten op GaAs laserdiodes. Tijdens deze stage werd zijn interesse voor de halfgeleiderfysica gewekt. Teruggekomen in de Stad van d'Olle Grieze deed hij zijn afstudeeronderzoek in de vakgroep Fysica van Dunne Lagen aan weerstandseffecten van twee-dimensionale elektronengassen in InAs. Ondertussen was hij student-assistent voor het begeleiden van tweedejaars studenten bij het Natuurkundepracticum.

Na zijn afstuderen in 1996, begon hij met zijn promotie-onderzoek aan de Technische Universiteit Delft, in de vakgroep Elektronische Componenten, Technologie en Materialen en het Delfts Instituut voor Micro-Elektronica en Submicron-technologie (DIMES). Dit onderzoek betrof een haalbaarheidsstudie van de amorf silicium Transversale Junctie Zonnecel en werd gefinancierd door de Nederlandse Onderneming voor Energie en Milieu B.V. (Novem). Tijdens zijn promotie was hij ook betrokken bij de werkcolleges Halfgeleidercomponenten voor derdejaars studenten Elektrotechniek.

Vanaf juni 2001 is de auteur werkzaam bij de divisie *Solar Arrays* van Fokker Space B.V. te Leiden.



